Title
Electrochemical Conversion of Greenhouse Gases to Value-added Products

Author
Shen, Kangze

Publication Date
2023

Peer reviewed|Thesis/dissertation

University of California, Los Angeles

Electrochemical Conversion of Greenhouse Gases to Value-added Products

A dissertation submitted in partial satisfaction of the
requirements for the degree Doctor of Philosophy
in Chemical Engineering

by

Kangze Shen

2023

ABSTRACT OF THE DISSERTATION

Electrochemical Conversion of Greenhouse Gases to Value-added Products

by

Kangze Shen

Doctor of Philosophy in Chemical Engineering

University of California, Los Angeles, 2023

Professor Carlos G. Morales-Guio, Chair

Electrochemical conversion of greenhouse gases to value-added products has emerged as a promising strategy to mitigate climate change and expand the penetration of renewable energy sources into the various sectors of our economy. As the accumulation of greenhouse gases in the atmosphere continues to increase, researchers have been exploring ways to utilize electrochemistry to capture and convert these gases into useful chemicals and fuels. This approach not only reduces the accumulation of greenhouse gases in the atmosphere but also provides a sustainable solution to the production of high-value chemicals and fuels. CH_4, CO_2 and other greenhouse gases can be converted into a range of valuable products, such as methanol, ethanol, formic acid, and hydrocarbons. The use of renewable electricity sources, such as solar

and wind energy, to drive the electrochemical conversion process further enhances its sustainability. The development of efficient and selective electrochemical conversion strategies for greenhouse gas utilization holds great potential for meeting the energy demands of the future while addressing the challenges of climate change starting today.

In this doctoral dissertation work, a series of systematic studies are carried out to elucidate the mechanisms of electrochemical CH_4 partial oxidation to methanol (Chapter 2), and the reactive capture of CO_2 to CO in amine and carbonate capture solutions (Chapter 3).

Among the catalysts for partial oxidation of methane studied in Chapter 2, electrochemically deposited transition metal (oxy)hydroxides are found to be active even without the application of a bias potential. Taking CoO_x as a prototypical methane partial oxidation electrocatalyst and combining systematic experiments in a rotating cylinder electrode (RCE) cell with DFT calculations, optimal conditions of low catalyst film thickness, intermediate overpotentials, intermediate temperatures, and fast methanol transport are identified to favor methanol selectivity.

CO_2 reactive capture and conversion (RCC) is also investigated with the RCE cell in Chapter 3. In the RCE cell, the transport properties are well-defined in the gas, liquid, and solid phases, which allows the elucidation of the origin of carbon sources during the electrochemical reduction of bicarbonate and amine-based CO_2 capture solutions on a silver catalyst electrode. In this study, dissolved CO_2 is revealed to be the primary carbon species being consumed while the CO_2-absorber complex appears to serve as a secondary carbon source only at highly negative potentials. Through the development of experimental methods for the differentiation of carbon species in solution during electrochemical carbon upgrading, the work presented here allows the comparison of experimental results to density function theory (DFT) calculations and contributes to the acceleration of catalyst discovery and reactor design for RCC technologies.

This thesis work stablishes new methodological approaches to catalyst and reactor design in the Morales-Guio group, and contributes broadly to the development of electrocatalytic technologies for the capture and conversion of greenhouse gases.

The dissertation of Kangze Shen is approved.

Panagiotis Christofides

Philippe Sautet

Chong Liu

Carlos G. Morales-Guio, Committee Chair

University of California, Los Angeles

2023

Table of Contents

List of Figures

List of Tables

Symbol and Abbreviations

C_i	concentration of species i ($mol\ L^{-1}$)
ca	circa
C_{dl}	double layer capacitance
CV	cyclic voltammetry
Δ	differential (finite)
dec	decade
E	potential
et al.	*et alii*
F	Faraday constant (96485 $C\ mol^{-1}$)
η	overpotential
HER	hydrogen evolution reaction
i	current
i.e.	id est
j	current density
j_0	exchange current density
k	Boltzmann constant (1.380649 x 10¡23 J K¡1)
log	logarithm
OER	oxygen evolution reaction
R	resistance
RHE	reversible hydrogen electrode
sat.	saturated
SHE	standard hydrogen electrode
RDE	rotating disk electrode

RCE rotating cylinder electrode

CE Coulombic efficiency

PTFE Polytetrafluoroethylene

Units and Prefixes

°C	degree celsius
A	ampere
C	Coulomb
eV	electron volts
g	gram
h	hour
Hz	hertz
L	liter
m	meter
M	molar ($mol\ L^{-1}$)
min	minute
mol	mole
s	second
V	volt
W	watt
Ω	ohm
T	tera- (10^{12})
M	mega- (10^{6})
k	kilo- (10^{3})
c	centi- (10^{-2})
m	milli- (10^{-3})
μ	micro- (10^{-6})
n	nano- (10^{-9})

Acknowledgements

I would like to thank Prof. Carlos G. Morales-Guio for his training, supervision, and guidance throughout my whole Ph.D. studies and his support through the completion of this doctoral thesis. With his mentorship, I transformed from a young student with limited knowledge in chemistry and materials science to an engineer as well as a researcher understanding the important role of transport in engineering. His dedication to research and teaching, along with his pursuit of excellence has greatly influenced my character. I am also grateful to my mother, Wanying Bai, and many others who have shown unwavering love, encouragement, and support to me throughout my life and career. All the help has been indispensable in helping me achieve my goals.

In addition, I would like to thank Prof. Panagiotis D. Christofides, Prof. Philippe Sautet, and Prof. Chong Liu for their guidance as my committee members and suggestions on my thesis.

I would also like to thank all my colleagues with whom I have worked over these years including Joonbaek Jang, Yu-Chao Huang, Derek Richard, Avishek Banerjee, Martina Rüscher, Jun Ke, Eber Reyes-Lopez, Ahmed Almunaifi, and Maximilian Winzely from the Morales-Guio Group; Simran Kumari and Dongfang Cheng from the Sautet Group; and Maiko Askari from the McCrory Group at University of Michigan.

Financial support from UCLA Graduate Division Fellowship, Sloan Foundation and Scialog Program is gratefully acknowledged, as my work could not have been possible without this support.

Chapter 1 is partially based on work published in: Jang, J., Shen, K., and Morales-Guio, C. G., “Electrochemical direct partial oxidation of methane to methanol” *Joule*, **3(11)**, 2589-2593, 2019.

Chapter 2 is partially based on work published in: Shen, K., Kumari, S., Huang, Y.C., Jang, J., Sautet, P. and Morales-Guio, C.G., “Electrochemical Oxidation of Methane to Methanol on Electrodeposited Transition Metal Oxides” *J. Am. Chem. Soc.*, **145**, 12, 6927–6943, 2023.

Chapter 3 is partially based on work published in: Shen, K., Cheng, D., Reyes-Lopez, E., Jang, J., Sautet, P., and Morales-Guio, C.G., “On the Origin of Carbon Sources in the Electrochemical Upgrade of CO_2 from Carbon Capture Solutions” *Under review at Joule*, 2023.

Curriculum Vitae

Education

University of Science and Technology of China **Aug. 2014 – Jul. 2018**

B.S., Materials Chemistry **Hefei, China**

Journal Publications

1. **Shen, K.**, Cheng, D., Reyes-Lopez, E., Jang, J., Sautet, P., and Morales-Guio, C.G., "On the Origin of Carbon Sources in the Electrochemical Upgrade of CO_2 from Carbon Capture Solutions" *In review*, 2023.
2. **Shen, K.**, Kumari, S., Huang, Y.C., Jang, J., Sautet, P. and Morales-Guio, C.G., "Electrochemical Oxidation of Methane to Methanol on Electrodeposited Transition Metal Oxides" *J. Am. Chem. Soc.*, **145**, 12, 6927–6943, 2023.
3. Jang, J., **Shen, K.**, and Morales-Guio, C. G., "Electrochemical direct partial oxidation of methane to methanol" *Joule*, **3(11)**, 2589-2593, 2019.

Chapter 1: Introduction

1.1 Motivation for research in greenhouse gas conversion technologies

Emissions of greenhouse gasses (GHG) including water vapor (H_2O), carbon dioxide (CO_2), methane (CH_4), nitrous oxide (N_2O), and ozone (O_3) are regarded as the major cause of global warming. These greenhouse gases absorb and radiate heat. Unlike oxygen or nitrogen which make up most of our atmosphere, greenhouse gases absorb heat radiated from the surface of the Earth, release energy within the thermal infrared range in all directions, and part of it reflects back to the surface of the Earth. About half of that energy goes out into space, and about half of it returns to Earth as heat, contributing to the greenhouse effect. Among the greenhouse gases, the concentrations of CO_2, N_2O, CH_4 has reached annual averages of 410 parts per million (ppm), 332 parts per billion (ppb), and 1866 ppb in 2019 with a measured increase in value of 19 ppm, 63 ppb and 8 ppb compared to the concentrations in the atmosphere in 2011.[1] Under current greenhouse gas emission rates, temperatures could increase by 2 ^oC by 2050.[2] With the significant increase of CO_2 and CH_4, mitigation of climate change due to the emissions of human activities has become one of the most serious challenges over the past years. Reducing emissions of greenhouse gases at the source as well as direct carbon capture from air have been regarded as two of the most effective solutions towards bringing GHG emissions to zero and net negative values.[3] While it is hard to directly stop the production of greenhouse gases, technologies for the removal of greenhouse gases produced, emitted or already existing in the atmosphere have drawn great attention from both the academia and the society. Therefore, research in greenhouse gases capture and conversion is in urgent need.

1.1.1 Motivation for research in CH_4 conversion

Methane (CH_4), as a hydrocarbon with the highest H/C ratio, possesses a high specific heat of combustion of 890.4kJ/mol,[4] owing to which, methane can be regarded as one of the most efficient and economical fuel sources for combustion compared with coal and oil.[5] CH_4 can be

found in shale gas, marine sediments and subsurface deposits in the form of combustible ice (methane hydrates), which was estimated to have a larger reserve more than 2 times of all other resources of fossil fuels in terms of energy.[6] As the major component of natural gas, constituting a volumetric ratio of more than 70%,[7] methane is abundant as fossil fuels contributing to 30% the total energy consumed in the US market.[8]

Methane is generated from the decay of organics, the emission from natural gas deposits, the digestion of food, and human activities such as crude oil production or waste management. In Figure 1.1, the major sources of CH_4 emissions to the atmosphere are summarized and plotted.[6]

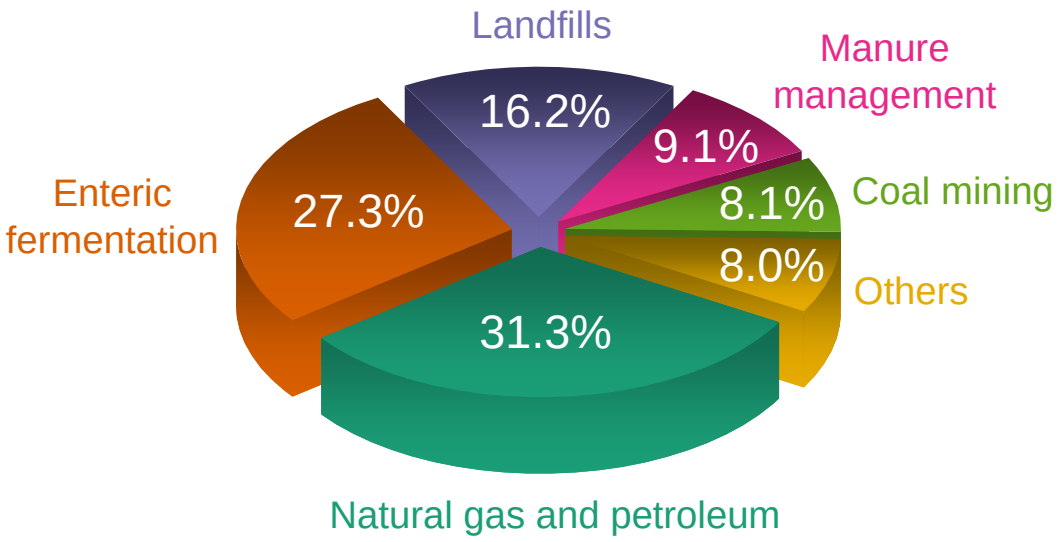

Figure 1.1: Proportion of different sources of CH_4 emissions to the atmosphere in 2017.[6]

Over a period of 100 years, methane is estimated to have around 30 times more impact on global warming than CO_2,[9] and has consequently contributed around 20% to the current rise in global temperature since pre-industrial times.[10] Methane emissions have surged drastically since the 1980s compared to any other time.[11] Hence, the control on the emissions of CH_4 is an indispensable part in addressing global climate change. Oil and gas industries have widely implemented techniques that substantially curve methane emissions including the application of vapor-recovery unit in upstream processing, the implementation of distributed sensors for leak

detection, and the preventive maintenance of the potential leaking sections in gas plants and pipelines.[12] With these operations, fugitive methane emissions can be reduced and the collected methane can potentially be further processed through different pathways, among which, the conversion of CH_4 to value-added chemicals is one of the most appealing ways.

1.1.2 Motivation for research in CO_2 conversion

Carbon dioxide (CO_2) is one of the most important and abundant greenhouse gases present in the atmosphere generated from either mild oxidation of organics like metabolisms of animals or strong combustion of fossil fuels like coal, petroleum, and natural gas. Meanwhile, CO_2 is consumed as the carbon fertilization in the photosynthesis of green plants and fixed as organics.[13]

Although CO_2 plays an important role in the carbon cycle, which is also a necessary life cycle between plants and animals, the concentration of CO_2 is rising drastically to an alarming level these years causing more serious global warming.[1]

1.2 Background on the partial oxidation of methane

Methane is the major component of associated petroleum and natural gas and is routinely flared at remote oil fields where its collection and use are deemed unprofitable. Gas flaring alone contributes 1% of the global CO_2 emissions and represents an energy loss of over 145 billion cubic meters of natural gas per year, equivalent to the total annual gas consumption of Central and South America.[14]

The current commercial way to fully utilize methane for the production of partially oxidized products requires centralized infrastructures to convert methane into synthesis gas (syngas) through steam methane reforming (SMR) as the first step, and the further catalytic conversion of syngas into products like methanol in a second step (Figure 1.2a). Direct methane conversion technologies including partial oxidation of methane (POM) and oxidative coupling of methane (OCM) have also been reported.[15] Among the oxidation products that can be produced from methane, methanol attracts much attention. In 2021, the annual demand for methanol reached

approximately 85 million metric tons and it is estimated to continue to grow at a rate of 4.3% per year to be nearly $38 billion by 2028[16]. Considering that the conversion of even less than 10% of the routinely flared methane into methanol would meet the annual methanol demand, partial oxidation of methane to methanol is becoming more attractive.

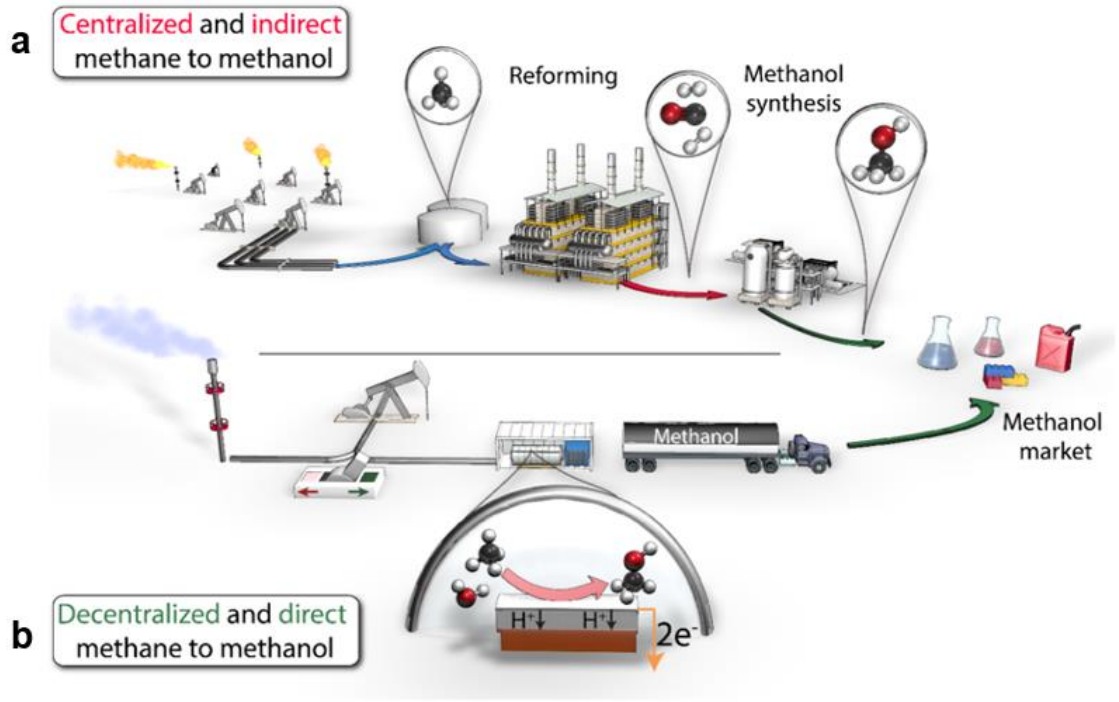

Figure 1.2: Centralized and Decentralized Methane-to-Methanol Technologies (a) Schematic of indirect methanol production involving methane reforming and methanol synthesis and purification in conventional centralized plants. (b) Direct electrochemical partial oxidation of methane to methanol in decentralized locations to reduce flaring and generate methanol for fuels and chemicals.

A commercial methane-to-methanol plant is economically viable when producing at least 2,500 metric tons per day (MTPD) of methanol. These large scales, typical of centralized petrochemical facilities, are necessary to justify investment in highly integrated and expensive heat recovery and power cogeneration networks. State-of-the-art methanol plants operating at energy and carbon efficiencies of up to 67% and 83%, respectively, require methane feeds of at least 2.1 million standard cubic meters per day (SCMD). In comparison, typical flare heads in decentralized oil and gas wells flare volumes of up to a few hundred thousands SCMD. Replacing gas flaring in remote oil fields with devices running on the well-established indirect methanol

production technologies is not possible at medium and small scales. Therefore, achieving zero routine flaring and reducing CO_2 emissions while generating revenue requires the development of novel synthetic routes for the decentralized production of methanol from methane.

Recent developments in electrocatalytic partial oxidation of methane to methanol at ambient temperatures promise to circumvent the requirement of high temperature in traditional thermal catalysis and offer a revolutionary alternative to flaring. Replacement of a 30,000 SCMD flare with a methane electrolyzer operating at carbon efficiencies of 83% would produce 36 MTPD of methanol, enough to fill a large tank truck. This production rate would generate geometric current densities of 0.5 A/cm^2 on an electrode with a surface area of around 500 m^2, which is equivalent to 10 stacks of electrolyzers each mounted with 20 cells of 2.5 m^2. Operations of this scale have been running successfully in the chlor-alkali process, which is one of the largest electrochemical industries. Although the final design of such a device can only be hypothesized at this point, reducing the footprint down to a size that can be installed on trailers or ships will allow the on-site transformation of methane as well as the storage and distribution of methanol to be accomplished upstream of the oil and gas industry.

The main challenge in developing a selective and efficient catalyst for the direct partial oxidation of methane to methanol originates from the difficulty to simultaneously control the kinetics for methane transport, activation, hydroxylation, and methanol desorption and removal. Traditional catalytic systems require high temperatures to overcome the barrier for methane C-H bond activation. Under these reaction conditions, it becomes extremely difficult to prevent over-oxidation of the produced methanol to thermodynamically more favorable products due to the lower dissociation energy of the C-H bond in methanol compared to that in the highly symmetric tetrahedral methane.[17] Inspiration on how to overcome this challenge can be taken from biological, homogeneous, and heterogeneous catalytic systems where various strategies have already been explored. Figure 1.3 presents a selection of the most distinctive mechanistic features that increase methanol selectivity in each system.

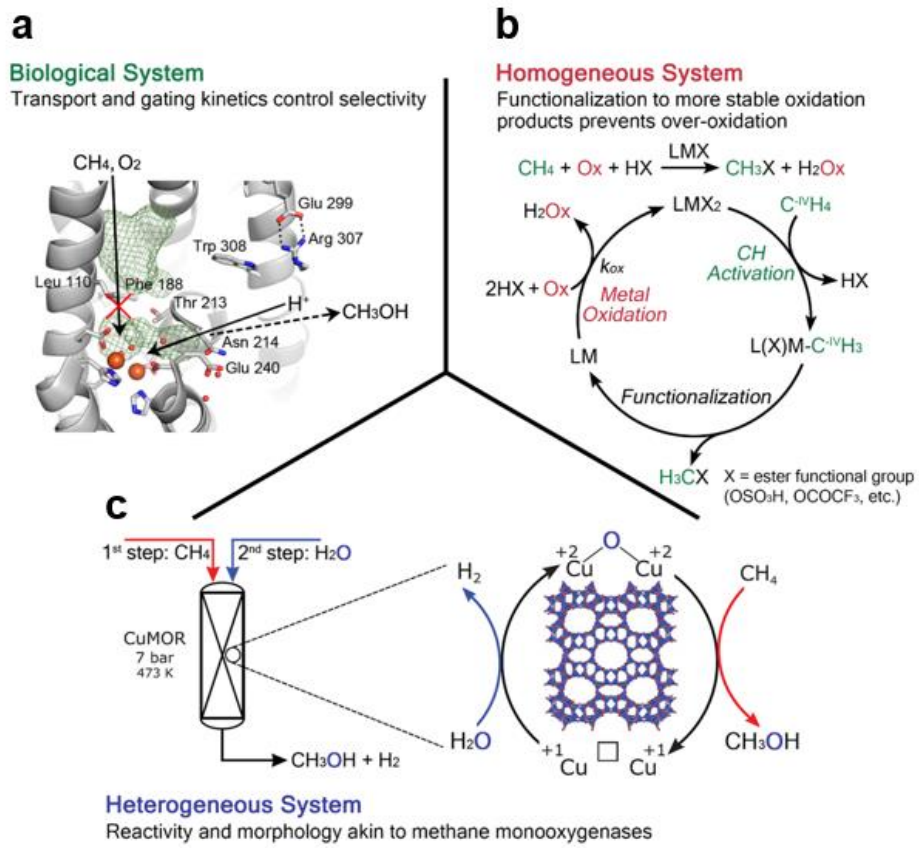

Figure 1.3: Overview of current mechanistic understanding for the direct methane partial oxidation to methanol over biological, homogeneous and heterogeneous catalysts. (a) One of the two conformations of the gating mechanism in biological systems showing disconnected hydrophobic cavities (green meshes) while the hydrophilic pore is opened for the release of the produced methanol that prevents over-oxidation and back diffusion.[18] (b) Representative CH activation scheme in homogeneous catalysis that preserve oxidation products through the functionalizing of methane to form a methyl ester (H_3CX) using strong acidic solvents (HX).[19] Methyl ester can subsequently be hydrolyzed to produce methanol (not shown). (c) Schematics of the chemical looping process and a single-atom active site stabilized inside the catalyst framework which are distinctive features of systems for the methane partial oxidation in heterogeneous catalysis.[20]

In nature, for example, methane monooxygenase proteins can transform methane directly to methanol with exceptional selectivity under ambient conditions through the exquisite control on the transport of oxygen, methane, and protons to the active center. In methane monooxygenase, hydrophobic cavities are linked together to allow the access of oxygen and methane to the active center through the connected hydrophobic passage. The delivered oxygen is then activated on the metal center of monooxygenase proteins to form an oxidative intermediate which cleaves the

strong C-H bond in methane.[18] By rearranging the enzymatic conformation, cavities detach from each other as in Figure 1.3a blocking the hydrophobic passage, while the produced methanol is released by opening up a separate hydrophilic pore. This conformational change prevents consecutive oxidation and back diffusion resulting in exceptionally high selectivity for methanol via efficient isolation of the active metal site.[18] The gating kinetics in biological systems highlight the importance of controlling mass transport to and from the catalytic site as one of the requirements for the design of synthetic systems selective for the methane-to-methanol transformation.

In supramolecular catalysts, a recent example has been the incorporation of a hydrophobic hemi-cryptophane cavity above a metal-based active center as a promising approach to increase methane-to-methanol selectivity through confinement effects.[21] However, the bio-inspired idea of physically isolating a catalytic metal center is not readily translatable to less sophisticated homogeneous catalysts.[22] A more straightforward approach widely adopted in homogeneous systems is to exploit protection schemes by functionalizing methane in the form of a methyl ester, which is much more stable in the reaction environment and can be hydrolyzed afterwards to recover methanol. Figure 1.3b shows one of the most representative mechanisms (C-H activation) among the many different reaction mechanisms available for methane functionalization using homogeneous catalyst.[19] In the cycle shown, catalysts consume stoichiometric amounts of oxidative agents to regenerate the high-valence catalytic species required to activate C-H bonds. Here, the strong acidic solvents (e.g., H_2SO_4, CF_3COOH) play the important role of both oxidizing the active center and stabilizing the product in its methyl ester form. The utilization of these solvents has led to high selectivity under less severe conditions and is a valid strategy to preserve products from over-oxidation.[17]

In the field of heterogeneous catalysis, bioinspired approaches have focused on investigating materials that possess reactivity and morphology akin to those of methane monooxygenases. Zeolite cages can stabilize single-atom active sites similar to the biological systems and have

shown high selectivity (>90%) towards methanol although the reported conversions varied depending on the conditions used and the oxidants employed.[22] The chemical cycling of Cu-promoted Fe-based zeolites between the activation of the metal center to a high-valence state using aqueous H_2O_2 and the partial oxidation of methane in the absence of the oxidant has resulted in high methanol selectivity at conversions of up to 10%.[23] However, attempts to extend the use of these materials to continuous systems using viable oxygen sources have been bounded to drastically low conversions (<0.1%) in order to maintain high methanol selectivity. More recently, the use of H_2O as a sole oxidant to produce methanol over the Cu-exchanged mordenite has been reported.[20] Despite the high selectivity observed, regeneration of active sites in this system is thermodynamically more challenging than in those using O_2 or H_2O_2 and requires higher temperatures in a pseudo-catalytic process involving inter-cycle activation stages (Figure 1.3c).

1.3 Electrochemical approaches to the partial oxidation of methane

Methane can be activated at ambient temperatures on the surface of an electrode, either directly by its reaction with a surface oxygen site (*O) or indirectly via its oxidation by free radicals generated at the electrode/electrolyte interface.[23] Formation of oxidative species is most likely an electrochemical process in both mechanisms, while methane activation is a thermochemical step. Electrocatalysis offers precise control over the rate of generation of these oxidative species by changing the applied potential and is a promising approach to control kinetics and impart product selectivity for the direct partial oxidation of methane to methanol. In electrocatalysis, the rate of product generation is primarily dictated by three factors, namely, the overpotential, the energetic barrier, and the collision frequency associated with the surface coverage and local substrate concentrations. The promise of electrocatalysts lies with the possibility to tune these three parameters independently to control transport and reaction kinetics near active sites similar or close in composition to those in biological, homogeneous, and heterogeneous systems.

1.3.1 Applied overpotential

The applied overpotential, which is an exclusive and intrinsic attribute of the electrocatalytic system, can directly change the thermodynamic landscape of a reaction plane at constant temperature, pressure, and composition. Changes in the electrochemical potential at the electrode/electrolyte interface, which can be biased by the externally applied potential, modify activation barriers for the absorption, desorption, oxidation, and reduction of species in the double-layer. The applied potential changes kinetics for the electron and charge transfer as well as the formation of oxidative species since both the water splitting to generate *O on the surface and the production of initiators for the radical activation pathway are electrochemical processes involving electron transfers. Therefore, the applied potential allows a fine-tuning of the relative kinetics of charge carriers transfer, oxidative species formation, and the accompanying reactions of oxygen evolution, methane activation, and methanol over-oxidation.

1.3.2 Energetic Barriers

Theoretical studies have suggested that it is critical to look beyond the energetics of a bare electrode surface for the thermal methane activation step. That is, the adsorption energy of *O scales with the applied potential and can potentially be a descriptor for estimating the energy required to activate the C-H bond. An electrode operating under conditions where oxygen species bind weakly to the surface provides more reactive oxygen sites and results in a lower energetic barrier.[24] The challenge in electrocatalysis is keeping high enough surface oxygen coverage while limiting the competing oxygen evolution reaction and accelerating the kinetics for methanol desorption to suppress over-oxidation. Modification of surface terminations through alloying, doping, nano structuring, or the creation of single-site catalysts are just a few of many tools to tune energetic barriers by tailoring electronic and morphological configurations. Electrolyte engineering via changes in pH and the nature of ions in the double-layer allows the guided tuning of kinetics at the electrode/electrolyte interface that could be applied to the methane electrocatalysis.

1.3.3 Frequency of Rare Events

The third factor is the number of collision events happening on the surface of a catalyst that could result in a net-forward reaction rate. Typically, effective collisions are rare events that are a function of temperature and will be proportional to the surface coverage and near-surface concentration of reactant species. Reactive *O can be readily generated electrochemically from water without the need for transport of chemical oxidants, while the local concentration of methane near the surface of an electrode can be increased by reducing the thickness of the concentration boundary layer and improving mass transport. In terms of selectivity, a short diffusion length for the transport of methanol away from the electrode surface is essential. Introducing methanol scavenging agents analogous to homogeneous systems is amenable to electrochemistry and can be implemented as part of electrolyte engineering to boost methanol yields. In this regard, the transport of methanol product away from an active site must be faster than its oxidation, and this emphasizes the importance of broadening catalyst design principles for methane partial oxidation beyond the transition state theory to include fundamentals of mass and charge transport.

1.4 Background in integrated CO_2 capture and conversion

To prevent the surge of global temperature, the conversion of the existing and produced CO_2 has attracted much attention over the last decades. So far, many possible solutions including biochemical, thermal, photochemical, and electrochemical approaches are reported to effectively convert CO_2 into value-added products.[25]

1.4.1 CO_2 capture

Compared with the current CO_2 capturing process relying on MEA-based solutions, a mixed-salt process (MSP) utilizing a liquid mixture of ammonia, potassium carbonate and water to capture CO_2 (NH_3-K_2CO_3-CO_2-H_2O) has been pioneered with high efficiency of CO_2 capture (> 90%), very high CO_2 loading (>10 wt%), a high-pressure CO_2 product (>10 bar), low NH_3 emission, and low reboiler duty (2.0 to 2.3 GJ per ton of CO_2) in a large bench-scale integrated system by

SRI as is shown in Figure 1.4.[26] Although the MSP process represents a step-change in solvent-based capture technologies, the energy used in the reboiler is still over 10 times larger than the thermodynamic minimum for CO_2 capture from a power plant exhaust (~200 MJ/ton CO_2). Additional energy inefficiencies in this process arise from large changes in temperature and pressure between the absorber unit (20 - 40°C and 1 bar) and the regenerator unit (>120 °C and 20 bar) which result in large exergy destruction across the whole process.

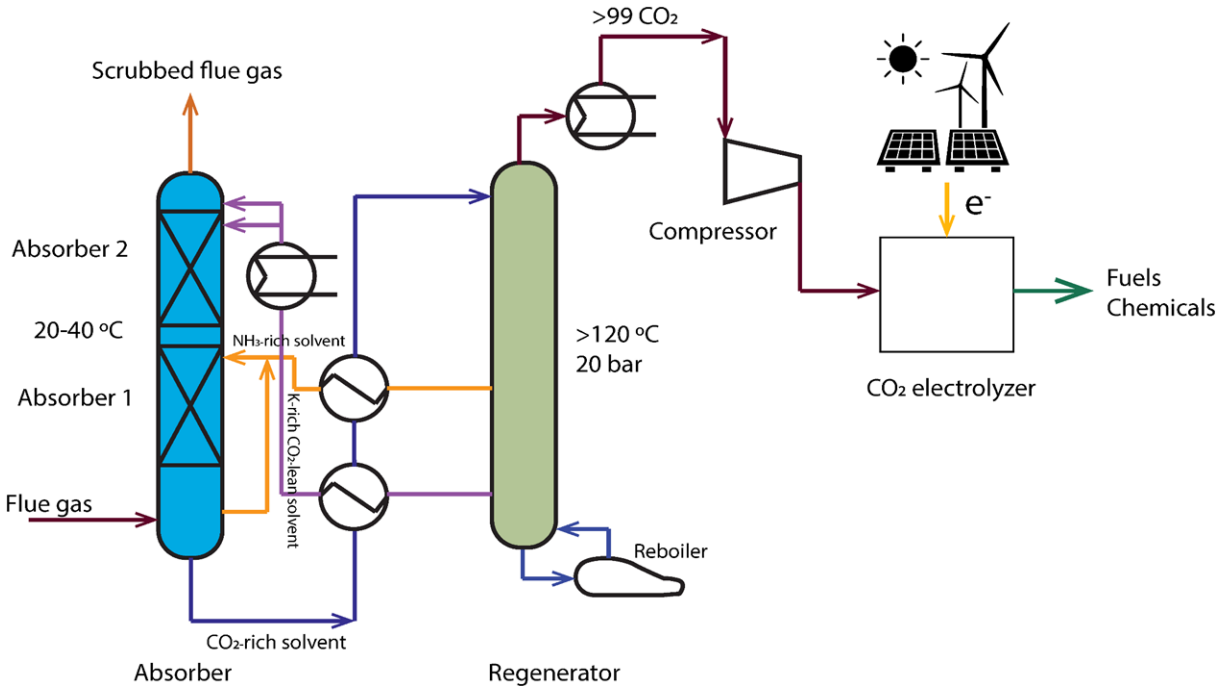

Figure 1.4: Schematics of the MSP process for CO_2 capture proposed by SRI.[26]

Hence, a change in paradigm is required to solve the problems mentioned above. Electrochemical cells operating at constant temperature and pressure are ideal systems to minimize the exergy destruction.

To make full use of the advantages of electrochemical cells, two possible ways are proposed: 1) To keep the efficient MSP absorber unit while replacing the regenerator unit with electrochemical cells to prepare pure CO_2 as the feed to the following CO_2 electrolyzer, which is an “electrochemical regeneration approach” 2) To integrate the absorber unit and the CO_2 electrolyzer, which is an “electrochemical reactive capture approach”.

1.4.2 CO_2 release

Many electrochemical approaches for the reactive capture of CO_2 are proposed as competitive alternatives to replace the existing thermal process (Figure 1.5) by utilization of i) pH change in the local environment to absorb CO_2 at high pH and release it at low pH[27 28 29 30], ii) metal cation (e.g., Cu) as an intermediate to substitute the CO_2 captured by amine absorbent and to be reduced back subsequently[31 32 33], iii) quinone and its derivatives[34 35 36 37 38 39], iv) bipyridine[40], v) disulfide[41], and vi) amine based derivatives[42 43 44] allowing the binding of CO_2 at the reduced state while releasing the captured CO_2 at the corresponding oxidized state through the control of the redox potentials. Compared with conventional heating process, the methods mentioned above minimize the exergy through the introduction of electricity, while drawbacks such as the requirement of expensive membrane and low recovery ratio of the absorbent are still preventing the application of these systems.

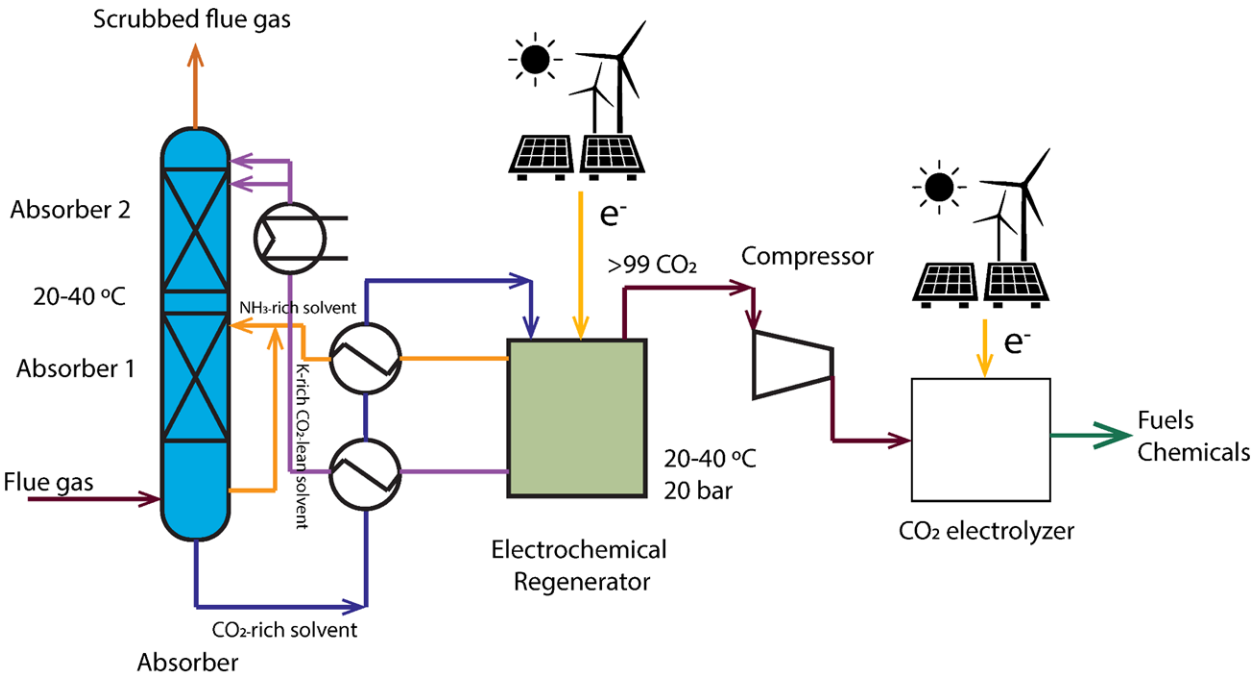

Figure 1.5: Process modification - Electrochemical regeneration approach

1.4.3 CO_2 reactive capture and conversion

The concept of "CO_2 reactive capture and conversion''(RCC) has become a hot topic where the absorption and conversion of CO_2 are realized simultaneously in an integrated system. Due to the existence of absorbent, normally amines, part of the absorbed CO_2 exists in the form of amine-CO_2 adduct while part of it remains free in the capturing agent.

Recently, some representative systems have been proposed with the concept of "CO_2 reactive capture and conversion". Besides the thermal hydrogenation of the captured CO_2[45] [46] [47], electrochemical approaches for the conversion have attracted more attention, which are shown schematically in Figure 1.6.

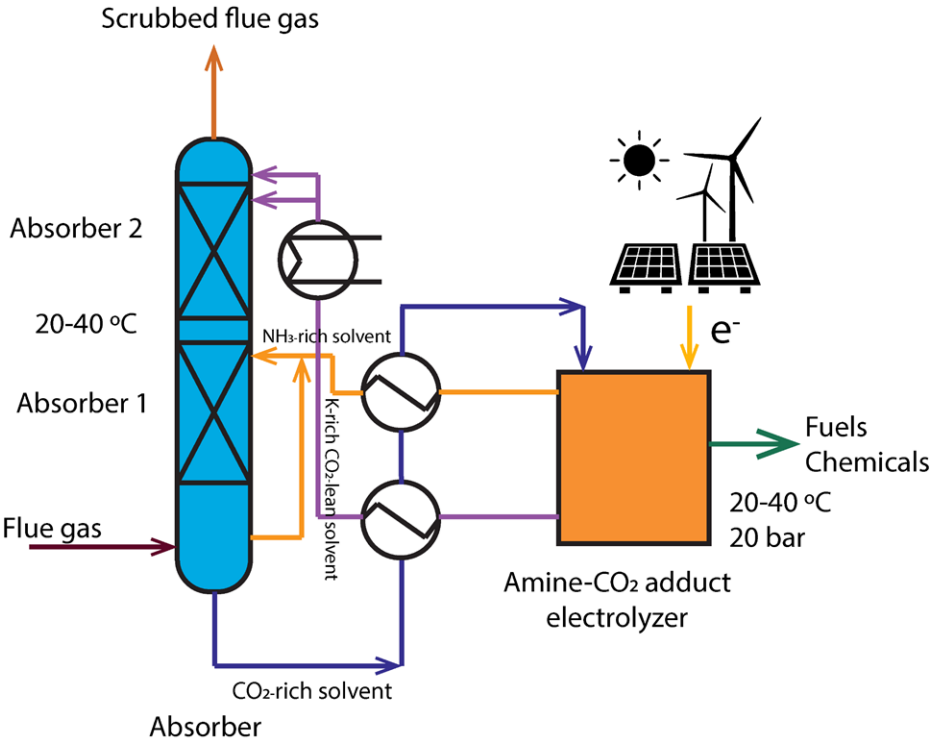

Figure 1.6: Process modification - Electrochemical conversion approach

1.5 Challenges and opportunities in the conversion technologies for greenhouse gases

A more comprehensive and in-depth understanding of the reaction mechanisms in the transformation of methane and CO_2 are urgently needed. Efforts to bridge the gap between theory and experiments must be pursued in order to one day have systems that operate at commercial

scales. However, even before these technologies can be brought to large-scale systems producing in the order of Mt/year, standards for evaluating processes should be developed, with particular attention paid to the following aspects:[5, 45, 48, 49]

a) Reactants: The amount of co-reagents for the activation should be minimized while the conversion ratio of co-reagents consumed with stoichiometric amount should be maximized.
b) Catalysts and by-products: Preferred catalysts should exhibit high activity and selectivity, while minimizing the production of unwanted by-products. Considerations for operation cost, elemental abundance, affordable prices, and recyclability are also important.
c) Solvent: Solvents creating a well-mixed homogeneous reaction environment are normally required. Thus, the accessibility of solvents and convenience for further separation should be considered and solvent-free reaction systems which may significantly reduce the overall costs will be favored.
d) Reaction temperature, pressure, time: Temperature swings should be avoided to prevent exergy loss and increase overall energy efficiency, however, the conversion ratio and the reaction rates contributing to the efficiency of production should also be balanced.
e) Separation: The unit cost, operation cost and the extent of convenience are the most important parts to be assessed in the separation process.
f) Waste production: The waste produced in each unit needs to be minimized, considering the CO_2 generated and the energy consumed.

It is noteworthy to mention that the factors listed above are not independent but coupled with each other instead. For example, the reaction temperature will play an important role in the performance of catalysts, cost of operation, and the final separation of products. Temperature swing must be avoided as the heat is not completely recovered especially at low temperature and

considerable energy loss occurs. Reaction rates, yields and selectivity that are coupled with each other will be affected simultaneously when different reaction pressure is chosen.

Balancing different factors is also challenging when deciding on the final design of reactors. High activity and selectivity are normally hard to achieve at the same time. Sometimes, catalysts with lower activity but higher selectivity may be preferred as they can reduce the cost of separation and post-processing of waste.

Above all, 3 most important parameters linked with the aforementioned aspects can be used for the assessment of the emerging conversion technologies:

a) Carbon efficiency: the fraction of carbon utilized. With higher carbon efficiency, the reactants, specifically, more CH_4 and CO_2 here can be consumed and fixed into value-added products.
b) Energy efficiency: the energy input and the energy output. The overall consumption of energy should be as low as possible.
c) Net carbon fixation/emissions: the carbon footprint through the whole process should be calculated, including the reactants consumed, cost of the preparation of catalysts, processing of the waste, and the carbon emissions of the whole process.

By performing a thorough investigation into the three parameters above, a convincing proposal can be finalized. With this set of standards evaluating all the future conversion technologies, the goal to limit the emission of greenhouse gases and to create revenue with the chemicals produced can be realized ultimately.

1.6 Dissertation objectives and structure

This dissertation discusses the conversion of greenhouse gases (methane and carbon dioxide) towards value-added products via electrochemical approaches. Specifically, the objectives of this dissertation are summarized as follows:

1. To examine the partial electrochemical oxidation of methane to methanol on transition metal oxides through combined approaches of theoretical DFT calculations and experimental tests under decoupled factors utilizing an RCE cell.
2. To explore the origin of carbon sources in the electrochemical upgrade of CO_2 from the carbon capture solutions in the process of CO_2 reactive capture and conversion.
3. To build a prototype for the electrochemical release of CO_2 via a “redox swing” of ammonia (Description not included in this thesis).

The dissertation is organized as follows:

In Chapter 2, a comprehensive and systematic study of the dependence of methane activation rates and methanol selectivity on catalyst morphology and experimental operating parameters is presented. An electrochemical method for the deposition of a family of thin-film transition metal (oxy)hydroxides as catalysts is used to prepare electrodes for the partial oxidation of methane. Among them, CoO_x, NiO_x, MnO_x and CuO_x are discovered to be active for the partial oxidation of methane to methanol. Taking CoO_x as a prototypical methane partial oxidation electrocatalyst, the dependence of activity and methanol selectivity on catalyst film thickness, overpotential, temperature and electrochemical cell hydrodynamics was systemically studied. Optimal conditions of low catalyst film thickness, intermediate overpotentials, intermediate temperatures, and fast methanol transport are identified to favor methanol selectivity. Through a combination of control experiments and DFT calculations, the oxidized form of the as-deposited (oxy)hydroxide catalyst films are shown to be active for the thermal oxidation of methane to methanol even without the application of a bias potential, demonstrating that high valence transition metal oxides are intrinsically active for the activation and oxidation of methane to methanol at ambient temperatures. Calculations uncover that electrocatalytic oxidation enables to reach an optimum potential window in which methane activation forming methanol and

methanol desorption are both thermodynamically favorable, methanol desorption being favored by competitive adsorption with hydroxide anion.

In Chapter 3, dissolved CO_2 is revealed to be the primary carbon species being consumed during the electrochemical reduction of bicarbonate and amine-based CO_2 capture solutions on silver electrodes through a combination of first-principle modeling and experimental electrochemical characterization methods. Carbon in the CO_2-absorber complex occurs to serve as a second carbon source only at highly negative potential. This work provides a deeper understanding of the reaction mechanisms and the nature of the reacting species at the electrode interface by quantifying the transport of species in solution and by determining the competitive reaction pathways for the electroreduction of captured and dissolved CO_2, which is necessary for the rational design of catalysts and scale-up of RCC technologies.

Chapter 4 summarizes the main results of the dissertation.

Chapter 2: Methane partial oxidation

2.1 Introduction

The direct partial oxidation of methane to methanol is one of the grand challenges in the area of catalysis and energy.[50] Methane is the major constituent of associated petroleum gas which is routinely flared at remote oil fields where its collection and use are unprofitable. The energy losses associated with flaring are roughly equivalent to the natural gas demand of Central and South America resulting in significant economic losses, while the associated greenhouse gas (GHG) emissions result in adverse effects on the climate and environment.[51, 52] In 2021 alone, gas flaring was responsible for the emission of 361 million metric tons (MMT) of CO_2, 39 MMT of CO_2 equivalent in non-combusted methane, and other GHGs and pollutants. There are large environmental and economic incentives to develop technologies for the decentralized transformation of methane into easy-to-transport liquid methanol as these would reduce GHG emissions,[50, 53] increase global carbon utilization, and expand the global methanol production capacity. Methanol current annual global demand is close to 100 MMT and is further projected to rise at a compound annual growth rate of over 5% to double by 2030.[54] This increase in methanol demand is primarily due to expansion of consumption by the automotive and olefin industries. Therefore, new and efficient technologies for the production of methanol from methane at medium and small scales[55] could offer a paradigm shift by connecting directly stranded carbon and energy resources to the base chemicals and energy markets.

The direct transformation of methane to methanol in remote locations requires selective catalysts capable of operating at near-ambient temperatures inside a modular device.[56-60] Although various catalytic systems have been studied for more than 100 years,[61-64] these have never reached commercialization due to low yields and poor selectivity. The main challenge in developing a selective and efficient catalyst for the direct partial oxidation of methane to methanol originates from the difficulty to simultaneously control the kinetics for i) the regeneration of the catalytic active site, ii) the transport, activation and hydroxylation of methane, and iii) the desorption and removal of the produced methanol

(Figure 2.1). Traditional catalytic systems require high temperatures or use strong oxidizing agents to regenerate the catalytic site and overcome the barrier for methane C-H bond activation. Under these reaction conditions, it is difficult to prevent overoxidation of methanol to CO and CO_2. Particularly, the oxygen atom in the produced methanol binds strongly to the metal site and requires the use of a solvent (i.e. H_2O in Figure 2.1) to desorb methanol and stabilize the reduced catalyst center.[65] Slow methanol desorption makes the product complex prone to overoxidation and introduces additional layers of complexity.[66, 67] Because of the multiple steps that need to be simultaneously controlled during the direct transformation of methane to methanol, developing selective and efficient catalysts[68] for this transformation has become one of the most remarkable challenges in synthetic catalysis.

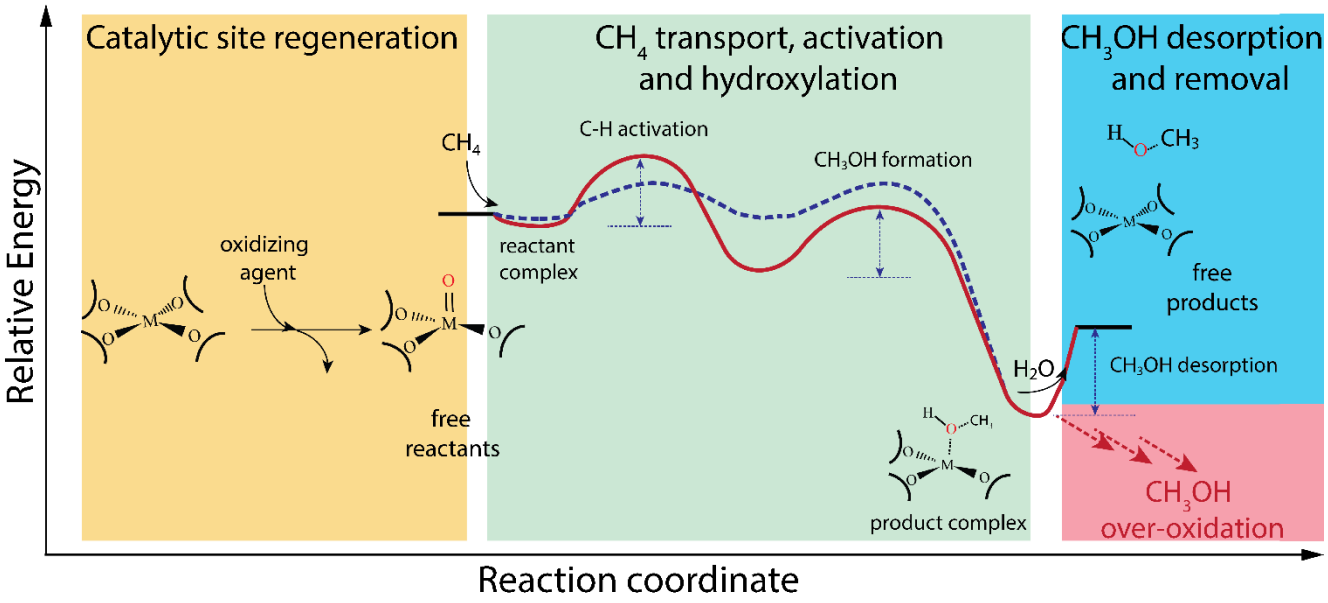

Figure 2.1: Schematic representation of the most important steps in direct methane to methanol oxidation. The simplified reaction energy diagram includes: the regeneration of the active site by an oxidizing agent or electron collector, the activation and hydroxylation of methane through two hypothetic reaction pathways (ionic in red trace and radical in blue trace), and the endothermic solvent-assisted desorption of methanol along the competing methanol over-oxidation. Parasitic decomposition of the regenerated catalytic site and non-catalytic oxidation of methanol are not shown for simplicity.

Enzymatic systems, on the other hand, offer clues on how to selectively catalyze this transformation. Methane monooxygenase, for example, catalyzes the transformation of methane directly to methanol with exceptional selectivity under ambient conditions. This is achieved through the exquisite control on the transport of oxygen, methane, protons and electrons to the transition iron(IV)-oxo complex in the active center.[66, 69] Conformational changes prevent consecutive oxidation and back diffusion and are responsible for the isolation of the active site and the exceptionally high selectivity for methanol.[70]

Electrocatalysis offers a precise control over the surface oxidative power via the applied potential and is a promising approach to control kinetics and impart product selectivity in the oxidation of methane to methanol just as in the enzymatic system.[50] Electrocatalysts can also replicate many of the mechanistic features in methane monooxygenases through the rational design and control of the electrostatic interactions between catalytic sites on the electrode surface, and the reactants and products penetrating the relatively immobile solvated ions that make up the coordination environment at the electric double layer. Advanced methane to methanol electrocatalyst should i) bring methane into the active site in the appropriate orientation to lower activation energy barriers and accelerate the rates of transformation, ii) regenerate metal-oxo species on electrode surfaces directly from water and remove electrons at slow rates relative to methanol desorption and overoxidation, and iii) have an electrode architecture with a high density of active sites connected to fast methanol transport and collection networks.

Over the last decade, the use of transition metal oxides as catalyst for the electrochemical partial oxidation of methane to methanol has drawn significant interest. Mustain and co-workers, for example, have shown that binary transition metal oxides of NiO/ZrO_2 catalyze the electrochemical oxidation of methane in carbonate electrolytes.[71-73] Park and co-workers also utilized a chemical precipitation method to prepare Co_3O_4/ZrO_2 nanocomposites and Co_3O_4 powder/ZrO_2 nanotubes that show activity for the production of higher alcohols such as 1-propanol and 2-propanol.[74, 75] In these works, the introduction of zirconia to unary transition metal oxides

has been suggested to be indispensable in order to promote methane partial oxidation in the presence of the carbonate ions. The challenge in these works utilizing particle catalysts is, however, that zirconia has multiple additional effects on transport which are poorly understood and must be deconvoluted. For example, the introduction of the catalytically inert, non-conductive zirconium oxide leads to different catalyst morphologies and spatial distributions of the active phase of the catalyst. These differences should be expected to affect selectivity as these modify the residence time of the methanol intermediate near the oxide surface and thus modify the probability for methanol overoxidation.[76] The requirement to use carbonate as mild oxidant is also not fully understood. Porous hollow fiber NiO/Ni anodes and iron-nickel hydroxide nanosheets have also been reported to produce methanol and ethanol as methane electrochemical oxidation products in aqueous hydroxide solutions where carbonate is not present in significant amounts.[77-79] CO_2 generated by the overoxidation of methane is likely to react with the highly alkaline environment to form carbonate in solution, but whether this carbonate can in turn become the major oxidant is not clear. It must also be noted that the faradaic efficiencies (FEs) in some of these systems exceed 100% (Table 2.1) implying that chemical reactions between methane and stoichiometric oxidants in the oxide catalyst or the electrolyte contribute to methane oxidation and could be responsible in part for the production of oxygenates. The production of methanol and other carbon products could also be the result of the degradation of carbon conductive materials and binders added in the preparation of the catalyst inks in some of these systems. To date, the intrinsic mechanisms for the activation of methane and the formation of methanol are largely unknown and are likely obscured by the lack of consistency across the existing literature with regards to the electrochemical setups used, the morphology of the catalysts, the composition of the electrolytes, the analytical tools used for product quantification, as well as the standards used for the reporting of activity, selectivity, and faradaic efficiency.

Table 2.1: Compilation of various electrochemical methane oxidation on different conditions and techniques

Electrocatalyst	Temp. (°C)	Pressure (bar)	Oxidant Sources	Electrolyte	Technique/Method	Products	Methane Conversion (%)	Selectivity (%)	Faradaic Efficiency (%)
Pd_2 (III,III)	80-140	6.9-35	SO_4^{2-}, SO_3	H_2SO_4	High-pressure three-electrode cell	CH_3OSO_3H, CH_3SO_3H	100	CH_3SO_3H: ~85	46
$ZrO_2/NiCo_2O_4$	RT	1	CO_3^{2-}	Na_2CO_3	Two-electrode cell	$CH_3CH_2CH_2OH$, $CH_3CH(OH)CH_3$, CH_3CH_2COOH, CH_3COCH_3, CH_3COOH	47.5	CH_3CH_2COOH: 65	100
ZrO_2/Co_3O_4	RT	1	CO_3^{2-}	Na_2CO_3	Three-electrode cell	$CH_3CH_2CH_2OH$, $(CH_3)_2CHOH$, CH_3CHO, C_2H_5OH, CH_3OH	40	>60 (total)	>100
$TiO_2/RuO_2/V_2O_5$/PTFE	RT	14	H_2O	Na_2SO_4	Gas diffusion electrode	CH_3OH, HCHO, HCOOH	100	CH_3OH: 97.7	57
(TiO_2/RuO_2)/PTFE	RT	14	H_2O	Na_2SO_4	Gas diffusion electrode	CH_3OH, HCHO, HCOOH		CH_3OH:	30
Pt	RT	46.5	$V(IV)O^{2+}$	$K_2PtIICl_4$/ $Na_2PtIVCl_6$/ H_2SO_4	High pressure, three-electrode, and two-compartment cell	CH_3OH, CH_3Cl, $CH_2(OH)_2$, HCOOH	13-19	CH_3OH: 70	>100
NiO/ZrO_2	RT	1	CO_3^{2-}	Na_2CO_3	Membrane electrode assembly	CH_3OH, HCHO, HCOOH, C_2H_5OH, CH_3COOH, C_3H_8O, C_3H_6O	-	-	-
NiO/NiHF	RT	1	OH^-	NaOH	Three-electrode cell	CH_3OH, C_2H_5OH	-	C_2H_5OH: 95	C_2H_5OH: 82-87
NiO/Ni	RT	1	OH^-	NaOH	Three-electrode cell	C_2H_5OH	32	87	81-89
Nanotube ZrO_2/Co_3O_4	RT	1	O_2	Na_2CO_3	Three-electrode cell	C_2H_5OH, $CH_3CH_2CH_2OH$, $CH_3CH(OH)CH_3$		$CH_3CH_2CH_2OH$ and $CH_3CH(OH)CH_3$: 91.98	>100
(V)-oxo dimer	RT	1~3	SO_4^{2-}	H_2SO_4	Three-electrode cell	CH_3OSO_3H	100	100	85-90
NiO/ZrO_2	RT	1	O_2	Na_2CO_3	Membrane electrode assembly	CH_3OH	-	-	5
MO_x M= Mn, Fe, Ni, Os, Pt	160	1	OH^-	$KOH+H_2O$	Membrane electrode assembly	CH_3OH		90	80
Cu_2O_3/TiO_2	RT	1	O_2	KH_2PO_4/KOH	Membrane electrode assembly	CH_3OH	-	-	6
Pt/C, Pd/C, and Ni/C	80-140	1	OH-	KOH/Nafion	Membrane electrode assembly	CH_3OH	13~20	-	
Pd/Graphite	RT	1	H_2O	$HClO_4$	Three-electrode cell	CH_3OH, C_2H_5OH	56	-	6.1
ZrO_2/CuO_x	RT	1	CO_3^{2-}	Na_2CO_3	Three-electrode cell	CH_3OH, C_2H_5OH, CH_3CHO, $CH_3CH_2CH_2OH$, $CH_3CH(OH)CH_3$	56		
V_2O_5/SnO_2	100	0.1	O_2	Mixture of 10% methane and 1% H_2O (Ar balance) and air	Fuel cell-type reactor	CH_3OH	-	88.4	61.4

Electrocatalyst	Temp. (ºC)	Pressure (bar)	Oxidant Sources	Electrolyte	Technique/Method	Products	Methane Conversion (%)	Selectivity (%)	Faradaic Efficiency (%)
PdAu/C	50-250	0.5	O_2	Cathode: 50 vol. % methane–50 vol. % oxygen mixture Anode: Hydrogen	Fuel cell-type reactor	CH_3OH	0.012-0.38	6~60	
Rh//NiO/V_2O_5	100	1	H_2O	Nafion membrane	Gas diffusion electrode	CH_3OH	-	97.9	91
Rh/ZnO Nanosheets	RT	1	OH^-	KOH	Gas diffusion electrode	CH_3OH, C_2H_5OH, CH_3COOH	-	85	22.5
$FeNi(OH)_x$	RT	1	OH^-	-	Three-electrode cell	HCOOH, C_2H_5OH, CH_3CH_3CO	-	75	87
$CoNi_2O_x$	RT	1	Cl^-	NaCl	Gas diffusion electrode	CH_3Cl	0.83~1.8	>99.75	95
CuO/CeO_2	RT	1~10	CO_3^{2-}	Na_2CO_3	Three-electrode cell	CH_3OH, C_2H_5OH, CH_3COCH_3	21	76~83	
Ti, V, Fe, Cu, Mo, Pd, Ag, W, Pt, Au	200	1	H_2O	Cathode: He Anode: Mixture of 20 vol. % methane and 6 vol. % H_2O (He balance)	Membrane electrode assembly	CH_3OH, C_2H_6	-	-	CH_3OH: 0-3%

Recently, Prajapati *et al*. demonstrated a comprehensive work that avoids the use of carbon conductive materials or binders and utilizes the surface oxides formed on metals upon electrochemical oxidation to show that four types of different transition metal oxides (TiO_2, IrO_2, PbO_2, and PtO_2) are active for the electrochemical methane oxidation reaction to CO_2 at oxidative potentials positive of 1.1 V vs SHE. A bimetallic Cu_2O_3 on TiO_2 catalyst was reported, where Cu was proposed to modify the reaction barrier for the key intermediates and facilitate the desorption of CH_3OH showing faradaic efficiencies for methanol of up to 6%.[80] Although these electrocatalysts have been shown to activate methane, none of the unary metal oxides was reported to produce methanol. Potential-dependent theoretical studies have suggested that methane oxidation on oxidized transition metal surfaces proceeds favorably at oxidative potentials where oxygen evolution also occurs.[80-82] The mechanism for the formation of methanol and the factors controlling its selectivity, however, are not well understood.

In order to gain a better understanding of the underlying mechanisms for methane partial oxidation, we have systematically approached this reaction through the breakdown of the three

competing rates in the oxidation of methane to methanol (Figure 2.1), namely, we have attempted to determine to the best of our abilities i) the rate of catalytic site regeneration and oxygen evolution; ii) the rate of methane transport, activation and hydroxylation; and iii) the rate of desorption and removal of the produced methanol. We have done this through the combination of high sensitivity product quantification tools, the use of advanced electrochemical reactors with well-characterized transport properties, and the design of experiments tailored to systematically decouple the multiple convoluted steps summarized in Figure 2.1. These experiments are combined to first-principle atomistic simulations to provide mechanistic understanding.

As a first step, we have decided to circumvent the use of catalyst inks. Here, we have used a one-step electrodeposition method for the preparation of transition metal (oxy)hydroxides as electrocatalysts. The oxidative electrodeposition method utilized here is self-limiting in growth and allows the deposition of largely amorphous, thin-film conductive metal (oxy)hydroxide films of known activity for water oxidation, well-defined charge transport mechanisms and measurable charge transport resistance.[83] Upon testing of these materials, we discover that CoO_x, NiO_x, CuO_x and MnO_x prepared via electrodeposition are active for the methane partial oxidation to methanol. In this work, we show that the detection and quantification of methanol and other oxidation products depends on the electrochemical cells used and the conditions for the collection of liquid and gas samples as reaction-transport kinetics control methanol product selectivity. Through the utilization of an advanced gas-tight cell with a rotating cylinder electrode, unique conditions of hydrodynamics for the partial oxidation of methane are realized, elucidating the importance of the control on both kinetics and mass transfer for each of the steps involved in the reaction. Calculations show an optimum potential window for selective methane oxidation into methanol.

2.2 Experimental section

2.2.1 Electrocatalyst materials and preparation.

Sodium acetate (NaOAc, anhydrous, ≥99%), Cobalt(II) chloride (CoCl2, anhydrous, >98%) and manganese(II) chloride (MnCl2, tetrahydrate, 97%) were purchased from Sigma-Aldrich. Nickel(II) acetate (NiOAc, tetrahydrate, 98%), iron(II) chloride (FeCl2, tetrahydrate, 99%), and copper(II) acetate (Cu(CH3COO)2, anhydrous, 99%) were purchased from Fisher Scientific. Millipore deionized water (18.2 MΩ cm) was used to prepare all of the electrodeposition baths. The concentrations of precursors used in electrodepositions of the different catalysts and specific pH are compiled in Table 2.2. Sodium acetate (0.1 M NaOAc) was used in all of the electrodeposition baths as supporting electrolyte. The pH of the baths was adjusted using either 0.1 M acetic acid solution or 0.1 M sodium hydroxide solution. All of the electrodeposition experiments were carried out under atmospheric conditions unless mentioned otherwise.

Table 2.2: Concentrations and pH of precursors in the electrodeposition baths

Catalyst	$CoCl_2$	NiOAc	$MnCl_2$	$FeCl_2$	$Cu(CH_3COO)_2$	pH
TiO_x (Substrate)	--	--	--	--	--	--
CoO_x	16 mM	--	--	--	--	5.5-6
NiO_x	--	16 mM	--	--	--	7.5-8
MnO_x	--	--	16 mM	--	--	5.5-6
FeO_x	--	--	--	16mM	--	7.0-7.5
CuO_x	--	--	--	--	16 mM	5.5-6

2.2.2 Catalyst electrodeposition.

An Autolab PGSTAT302N potentiostat/galvanostat was used for electrodeposition of the different transition metal oxides in a three-electrode setup with a titanium cylinder substrate (active geometric area = 3 cm^2) as the working electrode, a graphite foil as the counter electrode, and an Ag/AgCl as the reference electrode. Prior to use, the surface of the titanium cylinder electrode was polished using an alumina slurry suspension of 0.05 μm grain size on a microcloth polishing pad (Buehler), rinsed thoroughly with Millipore deionized water (18.2 MΩ cm), and sonicated in deionized water for 10-15 minutes. Prior to electrodeposition, the titanium cylinder

electrode was immersed in 2.5 M hydrochloric acid for 60 minutes to remove surface oxides. The titanium cylinders were then rinsed in deionized water and dried under Ar flow. In the electrodeposition process, all the applied potentials were measured against the Ag/AgCl reference electrode. Except for copper, electrodeposition of all the other catalysts was performed by 5 or 100 cycles of consecutive linear sweep voltammetry (LSV) within a specific potential window from 0.8 to 1.1 V vs Ag/AgCl at a scan rate of 10 mV s^{-1}. The deposition of most metal oxides was done using oxidative potentials ($M^{2+}(aq) \rightarrow MOOH(s) + e^{-} + 3H^{+}$) where the transition metal deposits on the surface of the electrode directly as an (oxy)hydroxide. As the oxidative electrodeposition proceeds, the oxygen evolution rate increases lowering the local pH and leading to the dissolution of the electrodeposited film. To suppress catalyst dissolution, the most positive potential during the LSV deposition was decreased by 50 mV after the 40^{th} and 70^{th} LSV. Copper, on the other hand was deposited under constant applied potential (−0.18 V vs Ag/AgCl) for 5 min via reductive deposition of the catalyst ($2Cu^{2+} + 2e^{-} + H_2O \rightarrow Cu_2O + 2H^{+}$). The potential vs current curves for the oxidative electrodeposition experiments and time vs current data for the copper deposition are shown in Figure 2.2.

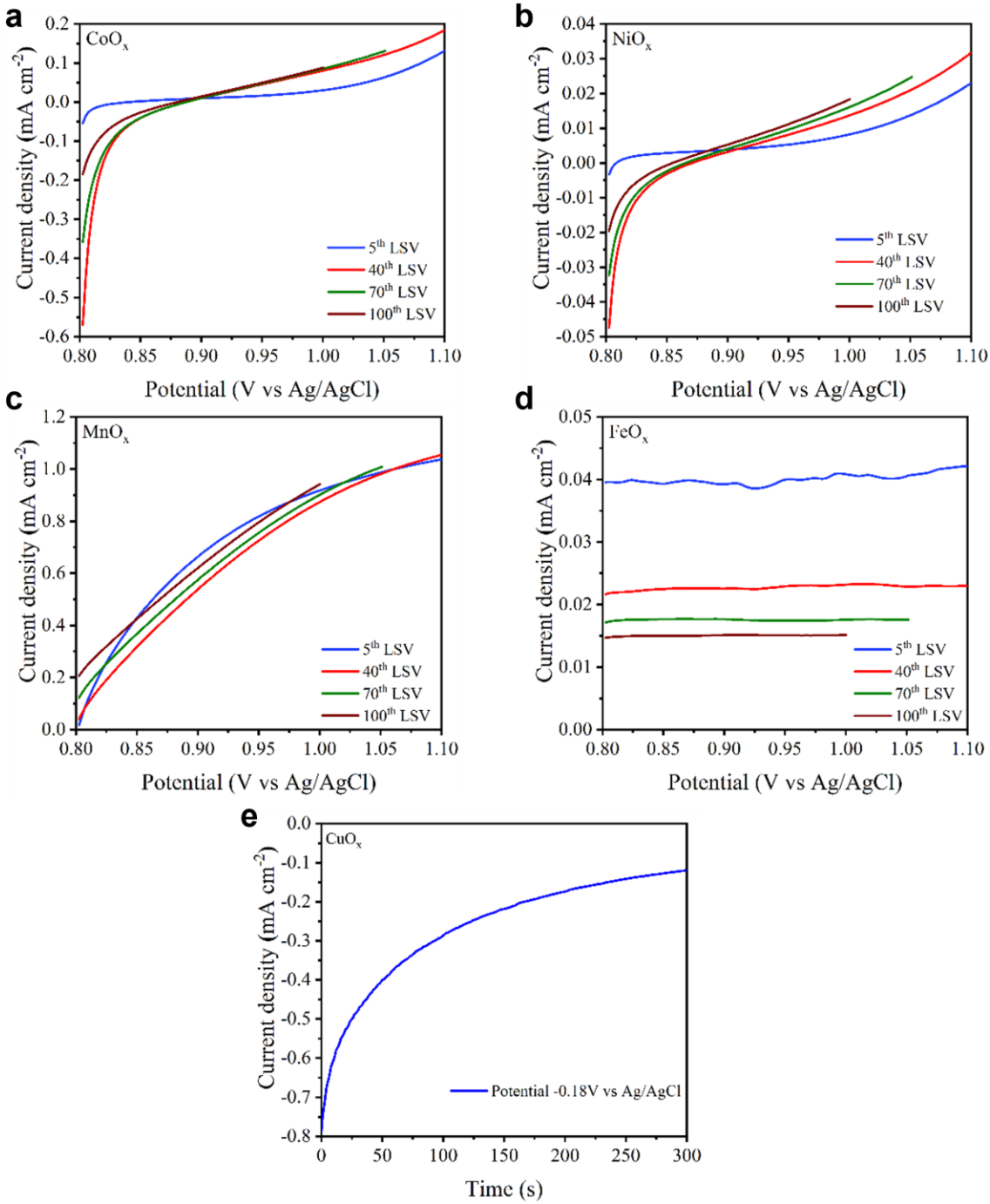

Figure 2.2: Electrodeposition profiles of different transition metal oxides. LSV oxidative electrodeposition of (a) CoO_x, (b) NiO_x, (c) MnO_x, and (d) FeO_x. Only a few selected LSV curves are shown for simplicity. (e) Constant potential deposition of CuO_x.

2.2.3 Electrochemical rotation cell setup for methane partial oxidation experiments.

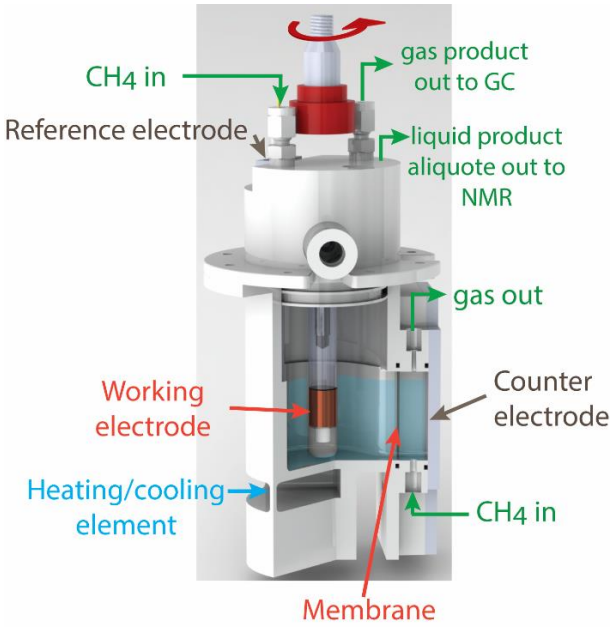

Figure 2.3: Schematic of the gas-tight electrochemical cell with a rotating cylinder electrode.

A gas-tight rotating cylinder electrode (RCE) cell recently reported by us[76, 84] was used for all the methane partial oxidation studies in this work. In the RCE cell, a follower magnet inside the cap traces a driver magnet outside the cell via magnetic coupling that allows for the rigorous control of the mass transport in the cell (Figure 2.3). The cell's cap carries the electrical connections and is designed to reduce the headspace above the electrolyte in the working electrode compartment. The cap for the working electrode compartment has three threaded ports to accommodate leak-free gas fittings (Swagelok). One of these ports is connected to a glass frit for the feeding of the CH_4 into the working electrode compartment, bringing in the gas feed and bubbling it directly into the electrolyte ensuring a high surface area for contact between the gas and the electrolyte and the consequent saturation of the liquid with dissolved methane. A second port serves as the gas outlet which transfers gaseous products out to the gas chromatogram (GC) connected to the RCE cell for the detection and quantification of gaseous products. The last threaded port is used to draw out liquid aliquots for further quantification of liquid products via nuclear magnetic resonance (NMR). This port is also used to measure the electrolyte temperature

at intervals during an experiment. In all experiments involving methane partial oxidation, methane is also bubbled in the counter electrode compartment. This is to keep similar gas environments in both cell compartments thus suppressing dissolved gas crossover. Hex screws that go through the entire lower compartments and nuts are used to compress and seal the cell. A cooling block with a heat-exchange area of 16 cm^2 is positioned below the bottom of the RCE working electrode chamber for temperature control. Liquid products accumulate in the cell over time and thus aliquots are drawn out at intervals of 20 minutes for analysis using a 500 MHz NMR.

2.2.4 Reactor kinetics

In methane partial oxidation experiments, we measure *reactor kinetics* and not *reaction kinetics*. The reactor kinetics in the RCE cell cannot be classified as either being of a batch, semi-batch or flow type. On one hand, a flow type reactor assumes low back mixing so that concentration gradients are a function of position along the flow path and it also assumes that these concentrations are not a function of time. Despite the continuous flow of gas in the RCE cell, liquid products accumulate in the electrolyte while some gas products are stripped away (i.e. O_2) and others of acidic nature such as CO_2 are absorbed in the alkaline electrolyte in the form of carbonates. A batch type reactor, on the other hand, assumes that the concentration is not a function of position but only a function of time. Our reactor system has a 3-dimmensional distribution of reactants, products and charge carriers that fluctuate as a function of time (*vide infra*). Therefore, the reaction kinetics in our reaction system are those of a *gastight rotating cylinder electrode cell* with accumulation of products and intermediates in the liquid phase of the cell. We have recently reported a detailed analysis of the hydrodynamics in these systems and how these affect reactor kinetics in Jang et al.[76] and Richard et al.[84] At the electrode/electrolyte interface, the reactor kinetics are better described by a continuously-stirred tank reactor (CSTR) approximation that captures the accumulation of products and their residence time near the surface of the electrode as well as the high local conversion of methane as external mass transport limits the supply of methane to the surface of the catalyst.

2.2.5 Electrochemical measurements

Prior to setting up of the cell, transition metal (oxy)hydroxides were freshly electrodeposited on a titanium cylinder electrode and rinsed thoroughly with deionized water. A three-electrode gas-tight rotation cell setup was used in all electrocatalytic measurements with the cylinder as the working electrode, a 5.8 cm^2 platinum foil (Pt, 0.1 mm thick, 99.99% metal basis, Alfa Aesar) as the counter electrode, a Ag/AgCl/1 M electrode (CH Instruments, Inc.) as the reference electrode, and a solution of 0.1 M potassium carbonate at a pH of 11.68-11.72 (K_2CO_3, Sigma Aldrich, 99.995% trace metals basis) as the electrolyte. After assembling the cell, the circulating bath was used to control and equilibrate the electrolyte temperature inside the working electrode compartment. Before electrochemical measurements, high purity argon gas (Ar, Airgas 99.999%) as the inert gas or methane gas (CH_4, Airgas 99.999%) as the reactant was flowed at a rate of 20 sccm for 30 Minutes in both the working and counter electrode compartments to prepare the gas saturated environments for electrochemical testing. These gas flow rates were maintained throughout the entirety of the electrochemical measurements. In control experiments used to understand the role of carbonate ions, instead of a 0.1 M potassium carbonate solution, a 0.1 M KClO4 (≥99.99% trace metal basis, Sigma-Aldrich) electrolyte adjusted to a pH of 11.8 was used.

In the electrochemical measurements, the uncompensated resistance was determined from the system response at the high frequency (f > 100 kHz) during electrochemical impedance spectroscopy (EIS) measurements. The potential drop across the resistance of the solution from the reference electrode to the cylinder electrode was accordingly corrected. The electrochemical response of the various catalysts was determined by cyclic voltammetry at the scan rate of 10 mV s^{-1}. The long-term electrochemical oxidation of methane was conducted in the RCE cell using chronoamperometry. The overall duration of chronoamperometry was 120 minutes for the electrochemical partial oxidation of methane and multiple gas and liquid samples were taken to quantify products. The specific time of sampling is discussed and shown in the following results and discussion section. Some of the most relevant electrochemical experiments and control

experiments were run by duplicate or triplicate to generate statistically significant results. Experiments that were carried out only once are shown without standard deviation bars.

2.2.6 Physical characterization

Morphology and microstructure analysis of the catalyst on the cylinder electrode was carried out using scanning electron microscopy (SEM, JEOL JSM 6700 F). X-ray photoelectron spectroscopy (XPS) measurements were obtained using a Kratos Axis Ultra DLD spectrometer with a monochromatic Al Kα X-ray source (λ = 1486.6 eV) to determine element composition of the different electrodeposited catalysts as well as their oxidation state before and after testing.

2.2.7 Product detection and quantification.

A gas chromatograph (GC) (8610C, SRI Instruments) was used for the detection and quantification of gas products. In methane partial oxidation experiments, the gas environment in the headspace of the cell was allowed to equilibrate and the first injection to the GC was made 20 minutes after the beginning of chronoamperometry measurements. The following injections were made at a 20-minute interval. Each GC run consisted of 14 minutes of running time and 6 minutes of cool-down between samples. Therefore, the gas product was sampled after 20, 40, 60, 80, 100, and 120 minutes after the beginning of the electrolysis, and each injection was used to calculate the Faradaic efficiency towards oxygen and CO and CO_2 products when generated. The detection limit for the detection of oxygen, CO and CO_2 gases is 250, 1 and 2 μA cm^{-2}, respectively.

Nuclear magnetic resonance spectroscopy (1D ^{1}H NMR 500 MHz with cryoprobe, Bruker) was used for the detection and quantification of liquid products. During the methane partial oxidation experiments, liquid aliquots were also collected at 20 minutes intervals (at 0, 20, 40, 60, 80, 100, and 120 minutes of electrolysis). Phenol (≥99.5%, Sigma-Aldrich) and dimethyl sulfoxide (DMSO, ≥99.9%, Sigma-Aldrich) were used as the internal standard for the quantification of liquid products. The internal standard was prepared by making a 52.5 mM of phenol and 2.1 mM of DMSO solution in deuterium oxide (D_2O, 99.9%, EMD Millipore). Calibration of the NMR signals

was done by calculating the ratio of the integration value of the signals for the different protons and the external standards for standard solutions containing known concentrations of each product. To quantify methanol partial oxidation products, all samples were prepared by pipetting 35 µL of the internal standard and 700 µL of the liquid aliquot into a new NMR tube. From the resulting 1D ^{1}H NMR spectra, the signal areas were normalized by that of DMSO, and the normalized signal areas were compared to the standard curve to calculate concentrations of liquid products during the partial methane oxidation reaction. The calibration curve for methanol is shown in Figure 2.4 as an example of the calibration curves obtained. Similar calibration curves were obtained for acetate and other potential products including formate, ethanol and propanol. The limit of quantification for methanol is 2.5 µM and is defined as the concentration at which the signal to noise (S/N) ratio is 10 while the limit of detection is 0.83 µM defined as the concentration at which the S/N ratio is 3.3. 128 scans were used for the acquisition of each NMR spectra.

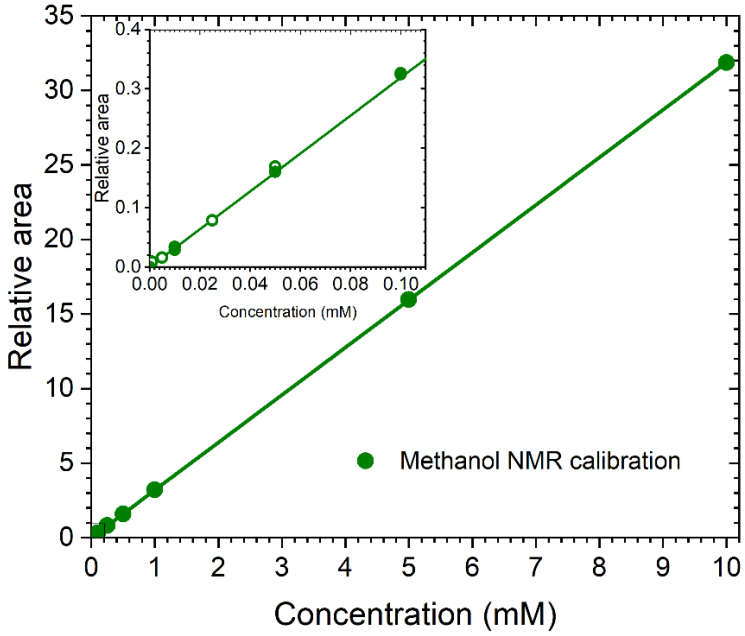

Figure 2.4: 1H NMR Calibration curve for methanol detection utilizing a 500 MHz NMR. Filled and open circles correspond to calibration solutions prepared starting from a 10 mM and 0.1 mM methanol stock solution.

2.3 Theoretical section

The Vienna ab initio simulation package (VASP), version 5.4.4,[85-88] with the PBE GGA functional, [89] was used to implement periodic density functional theory (DFT) for all calculations. The projector augmented plane-wave (PAW) method was used to describe the electron-nuclei interaction. Oxide catalyst surface were modelled with periodic slabs, with supercell vectors of size 5.75 Å and a 4x4x1 Monkhorst-Pack grid was used for the k-point sampling of the first Brillouin zone. The cut-off energy for the plane wave was set at 600 eV, and the energy convergence threshold for the self-consistent-field (SCF) cycles was set at 10^{-6} eV per cell. Dispersion interactions were included according to the dDsC correction.[90-92]

Since β-CoOOH (*R3m* space group) was found to be the cobalt oxide phase that was most active under alkaline pH and oxidative circumstances, preliminary bulk full relaxation was conducted on this compound.[91, 93, 94] According to Bajdich *et al*.,[91] the reference surface slab was taken as a 2x2 supercell of the primitive surface cell cut from bulk β -CoOOH in the most active (10-14) direction. Convergence in the adsorption energies and recovery of the bulk magnetic ordering of the center layers was obtained with a minimum thickness of four Co oxide layers and 30 Å of vacuum. To complete their octahedral coordination shell, each surface Co atom was liganded with one hydroxyl group, which would be expected in electrochemical conditions under liquid water.[91, 94-96] All model slabs show two identical surface and present an inversion symmetry to cancel any dipole moment in the perpendicular direction. Only the outer atoms were allowed to relax during the surface geometry relaxations; the inside atoms (in a 2 Å large intermediate layer) and cell parameters remained fixed at the values established for the bulk β-CoOOH. These relaxations were continued until the residual forces were less than 0.02 eV $Å^{-1}$. A Fermi smearing of 0.026 eV, or 298 K in temperature, was used to calculate the electronic occupancies. To better describe the electronic structure of this high electronic correlation material, a model Hubbard Hamiltonian (designated + U) was included in the calculations. On the basis of previous works,

the formalism proposed by Dudarev *et al*.[97] was used, along with the *U–J* value of 3.52 eV for the cobalt 3d electrons.[90-92]

Accounting for solvation effects was achieved by exploiting an implicit solvation model as implemented by Hennig and co-workers under the name VASPsol.[98-100] The influence of the electrochemical potential was included using the surface-charging method, with an implicit modelling of the electrolyte based on the linearized Poisson-Boltzmann (PB) equation.[99, 100] In contrast to the initial surface charging approach, which relies on a homogeneous background charge,[101] this electrolyte distribution balances the surface charge without the need for any correction terms. Hajar *et al*. have provided a more thorough explanation of the compared methods.[102]

Because we are dealing with a grand canonical description of the electrons from the surface charging methods, the energies reported in this work are free energies. The influence of the change in zero-point energy (ZPE) was found to be small in other works.[92, 94] Therefore, considering the number of intermediates, the influence of ZPE was not computed here.

2.4 Results

The results section of this manuscript is organized in chronological order in which we approached the research of methane oxidation catalysts. First, we determine the maximum methane oxidation rates achievable in our RCE cell based on the well-defined transport properties of our system. We also establish what are the maximum partial current densities for methanol and accordingly, the quantification limit of the analytical tools needed to measure methanol production in our cell. Second, we describe the deposition and physical characterization of the thin-film transition metal (oxy)hydroxides. Third, we describe the catalytic activity of transition metal (oxy)hydroxides for the partial electrochemical oxidation of methane and the results obtained during the systematic interrogation of these materials to separate the transport, electrochemical and thermochemical contributions to the experimental performance. Finally, we present our DFT

study of the reaction mechanism and potential dependence, and show that there is an optimal window of potential for selective methanol oxidation.

2.4.1 Determination of maximum methanol production rates.

In our RCE cell, the film transfer coefficient for any molecule or ion can be calculated from the Sherwood number Sh_{RCE} which is given by the relation in Equation 2.1[76, 84] where Re and Sc are the Reynolds and Schmidt numbers, respectively. The average deviation from the experimentally measured Sh number with the general correlation in Equation 2.1 is ±7.7% for Re>500. At lower Re numbers for the RCE system, the background convection by the bubbling of the gas dominates mass transport to the surface of the electrode.[84]

$$Sh_{RCE} = \frac{k_m}{D/d_{cyl}} = 0.204 {Re_{RCE}}^{0.59} Sc^{0.33} \quad (1)$$

At a temperature of 17 °C utilized in most of the experiments in this work, the concentration of methane in solution at an overhead pressure of 1 atm of CH_4 is 1.6 mM. When the cylinder electrode is rotated between 100 and 800 rpm (corresponding to Sh_{RCE} numbers for methane of 87 and 295), the mass transport limited flowrates of methane to the surface of the electrode $J_{CH4,\,\mathrm{max}}$ are between 1.9 and 6.3 x 10^{-9} mol cm^{-2} s^{-1} (Figure 2.5, top panel). At these methane transport rates, the maximum partial current densities for the partial oxidation of methane to methanol $j_{CH3OH,\,\mathrm{max}}$, assuming a two-electron oxidation process, ranges between 0.36 and 1.22 mA cm^{-2} (Figure 2.5, middle panel). The low partial current densities are to be expected as mass transport to the electrode is limited by external mass transport of methane from the bulk of the electrolyte, and because methane is one of the less soluble gases in water.

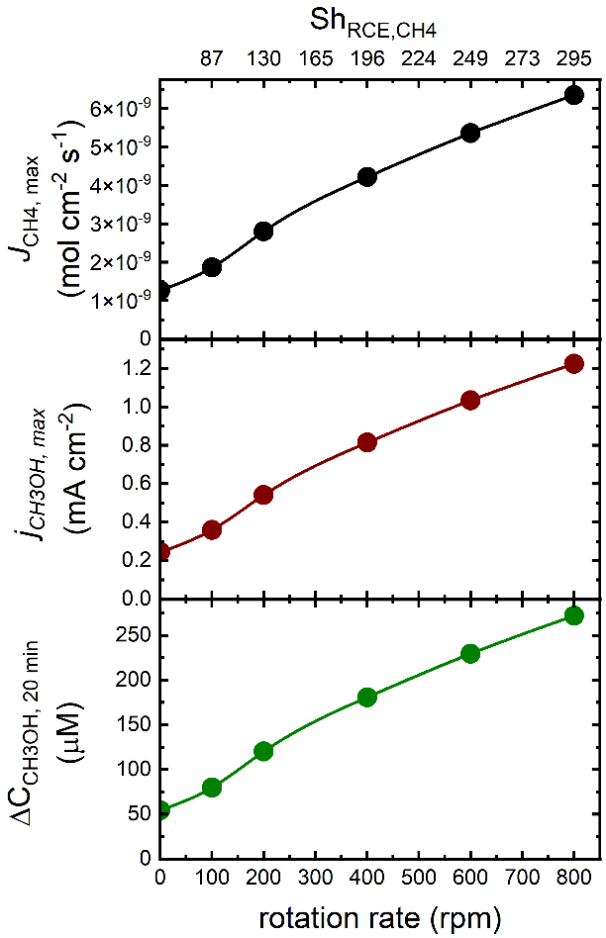

Figure 2.5: Mass transport limited methane partial oxidation $j_{CH4,\,\mathrm{max}}$ with the corresponding maximum partial current densities for methanol $j_{CH3OH,\,\mathrm{max}}$ and the maximum methanol concentration change in the electrolyte between liquid samples collected every 20 minutes $\Delta C_{CH3OH,\,20\,\mathrm{min}}$.

In the RCE cell, a compromise is made between obtaining high partial current densities for methane to methanol oxidation and decoupling transport effects from intrinsic kinetics. Because the cylinder electrode active area is 3 cm^2 and the volume of electrolyte in the cathode compartment is 84 mL, the maximum change in concentration of methanol that can be measured over a liquid sampling interval of 20 minutes $\Delta C_{CH3OH,\,20\,\mathrm{min}}$ is between 54 and 270 μM (Figure 2.5, bottom panel) for electrodes rotated at speeds between 0 and 800 rpm, respectively. This would imply that all methane reaching the electrode is transformed selectively to methanol, which is not typically observed. The 500 MHz NMR utilized for methanol quantification has a limit of detection of 0.8 μM and thus is sensitive enough to quantify methanol products in our experimental setup.

Other techniques such as HPLC, have quantification limits in the order of 1 mM[80] and cannot be used to detect methanol in our system. The use of HPLC for methanol quantification in our system would require an order of magnitude larger electrode area to electrolyte volume ratio.

2.4.2 Electrodeposited transition metal (oxy)hydroxides

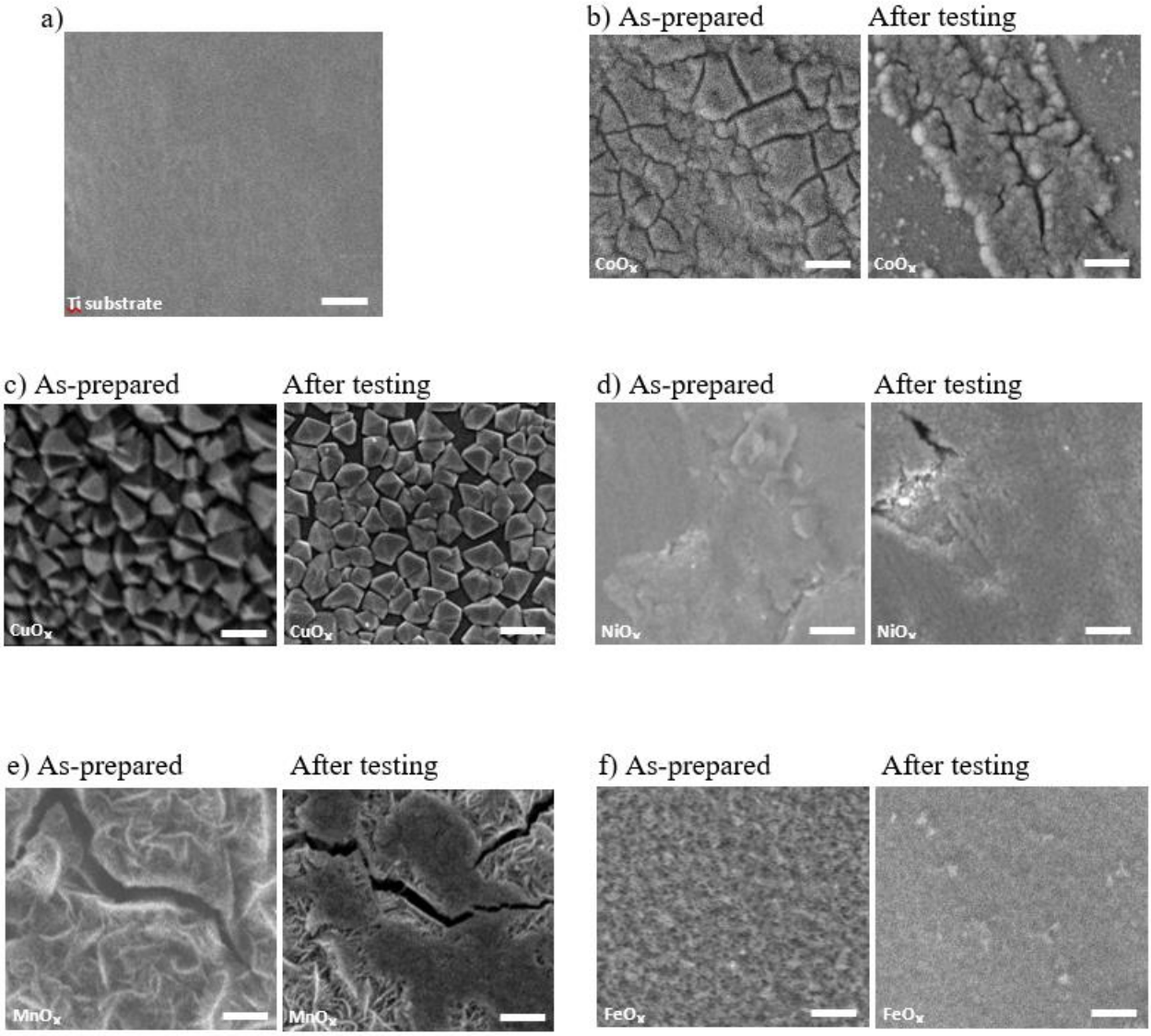

Figure 2.6: SEM images of (a) blank titanium, (b) CoO_x, (c) CuO_x, (d) NiO_x, (e) MnO_x, and (f) FeO_x electrodeposited on a titanium cylinder electrode. SEM images are shown for the as-prepared samples and after electrochemical oxidation of methane for 2 hours. The scale bars in all the samples correspond to 1 µm.

Unary transition metal (oxy)hydroxides of CoO_x, CuO_x, NiO_x, FeO_x, and MnO_x were prepared by electrodeposition as described in the experimental section.[83] Scanning electron microscopy

(SEM) was used to characterize the morphology and microstructure of different transition metal (oxy)hydroxides on the surface of the titanium substrate (Figure 2.6) before and after electrochemical oxidation of methane for 2 hours. The titanium substrate showed a relatively flat surface after mechanical polishing and immersion in the HCl solution to remove the surface oxide. Electrodeposited cobalt (oxy)hydroxide shows the typical dense film morphology observed for electrodeposited cobalt oxides.[103] Cracking of the films is observed upon drying and the pulling of vacuum for electron microscopy. After electrochemical testing over 2 hours, some of the cobalt oxide film was lost (Figure 2.6b). The electrodeposited copper oxide (Figure 2.6c) showed angular particles before oxidation with edges and corners closely packed on the surface of the titanium substrate. The copper oxide film after 2 hours of testing appeared less densely packed while the particle edges were still well defined. Nickel (oxy)hydroxide (Figure 2.6d) exhibited a porous film morphology formed by small nanoplates. This nanoplate morphology was maintained after methane partial oxidation and is similar to those obtained during electrodeposition of other nickel (oxy)hydroxides.[83] Manganese (oxy)hydroxide (Figure 2.6e) showed larger nanoplates compared to the nickel oxide catalyst. The MnO_x film also showed cracks upon drying but maintains the nanoplate morphology. Iron (oxy)hydroxide Figure 2.6f) showed a porous structure in a dense film similar to NiO_x before oxidation, while its porous microstructure could not be entirely resolved after oxidation. In general, the oxidatively electrodeposited transition metal (oxy)hydroxide films can be characterized as porous thin films while CuO_x is dense and nonporous. The slight changes in morphology between before and after testing are in line with changes observed for thin film transition metal oxides used for electrochemical water oxidation, where some of the catalyst film is lost via dissolution under the local acidic environments.[83, 103] The thickness of the catalyst films varies between a few nanometers for the films deposited with only 5 LSVs to a few hundred nanometers for the films deposited with 100 LSVs. The maximum catalyst loading achieved by oxidative electrodeposition is of less than 100 µg per cm^2 as determined by electrochemical quartz crystal microbalance measurements.[83]

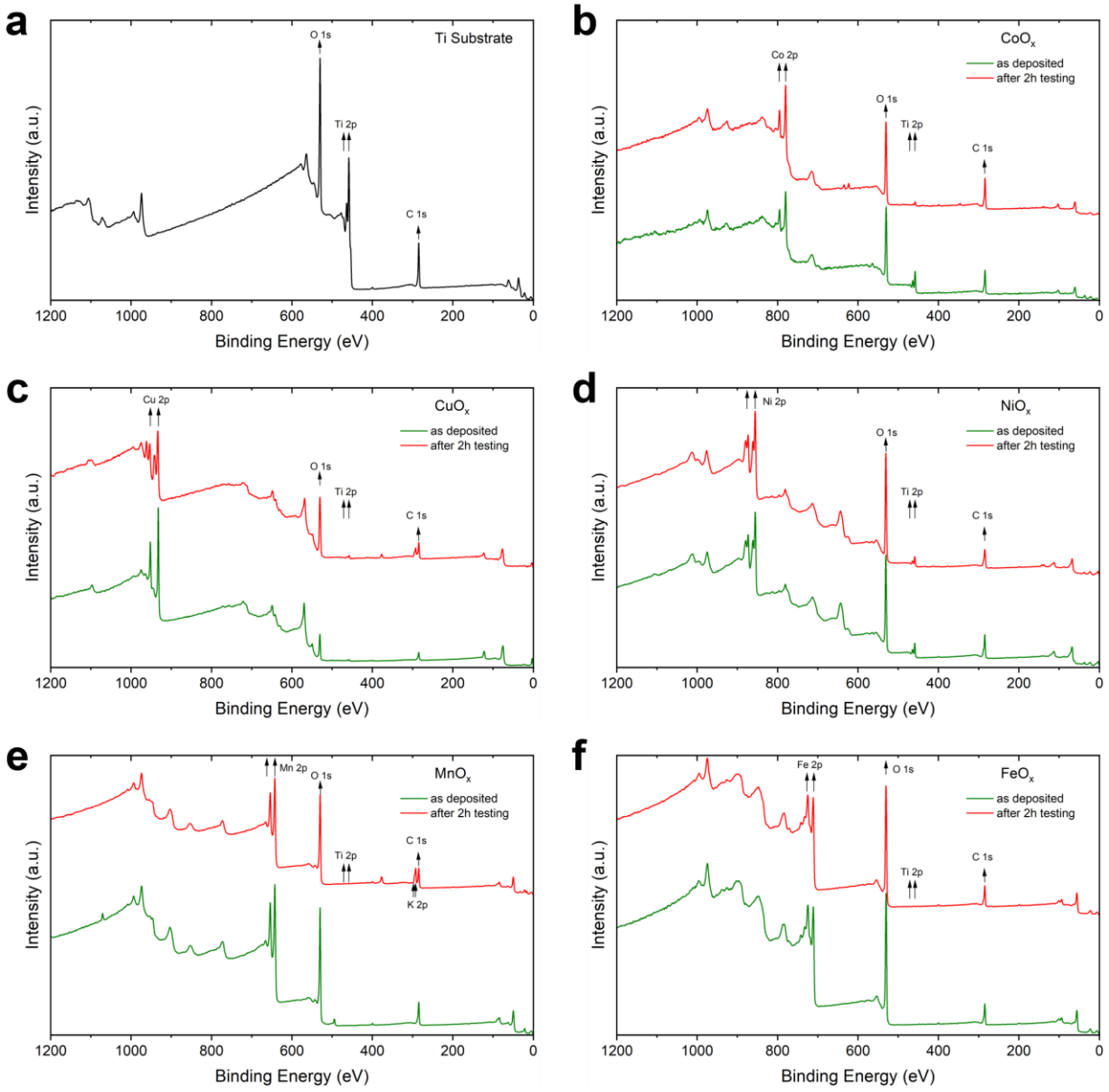

Figure 2.7: Wide-range XPS spectra of the surfaces of (a) titanium cylinder substrate and the different unary transition metal (oxy)hydroxides (b) CoO_x, (c) CuO_x, (d) NiO_x, (e) MnO_x, and (f) FeO_x prepared through 100 LSVs. XPS spectra before and after testing of the electrocatalyst for the electrochemical oxidation of methane are shown.

The chemical compositions of the titanium substrate and the different transition metal oxides (CoO_x, CuO_x, NiO_x, MnO_x, and FeO_x) were determined using *ex situ* XPS (Figure 2.7). The titanium substrate signal is non-existent or very small compared to the XPS signal from the various metal (oxy)hydroxides indicating the conformal deposition of the catalysts over the cylinder geometry in the form of unary metal (oxy)hydroxides. The XPS signal from all the catalyst

deposited via oxidative electrodeposition remain unchanged after testing indicating that the electrodeposited form of the (oxy)hydroxides is identical to that active for water and methane oxidation (Figure 2.8). Only CuO_x changes before and after testing as this catalyst is deposited via reductive electrodeposition. The titanium substrate showed signals of both metallic titanium and TiO_2. The Co 2p signal from the as-deposited and after testing CoO_x catalyst corresponds to that of cobalt in CoOOH. The acetate to cobalt ratio before and after testing does not change significantly and is in a ratio of 1 to 0.6-0.7 (Figure 2.8). The Ni $2p_{3/2}$ signal from the as-deposited and after testing NiO_x electrocatalyst has a Binding energy of 856 eV corresponding to high oxidations states of +3. The presence of oxide and hydroxide signals in the O 1s region indicate that the NiO_x is better described as a NiOOH. The layered nickel (oxy)hydroxide accumulates acetate in the interlayer spacing and the Ni to acetate ratio is of 1 to 0.6 in the as-prepared material and decreases to 1 to 0.3 after prolonged testing for methane partial oxidation. The high binding energy of the Mn 2p signal (642.5 eV) in the MnO_x catalyst indicates the high valence oxidation state of the Mn atom and remains similar before and after testing. The acetate content in the MnO_x catalyst is lower than in the other electrodeposited oxides and has a ratio of Mn to acetate of 1 to 0.3 before testing and decreases to 1 to 0.15 after prolonged methane electrochemical oxidation. After testing, K 2p signals are evident for the MnO_x and CuO_x samples despite washing of the electrode with abundant deionized water. The FeO_x catalyst is deposited in the form of FeOOH with an Fe to acetate ratio of 1 to 0.2. This ratio remains constant even after testing for methane oxidation. The Cu 2p signal of the as-deposited CuO_x catalyst corresponds to that of Cu_2O while that after testing corresponds to CuO. The resting oxidation states of the metal (oxy)hydroxides after testing are thus +2 for CuO_x, +2/+3 for NiO_x, +2/+3 for the CoO_x, +3 for the FeO_x, and +3 for the MnO_x. The open circuit potential for the catalyst films after methane oxidation is between 0.6 and 0.7 V vs SHE.

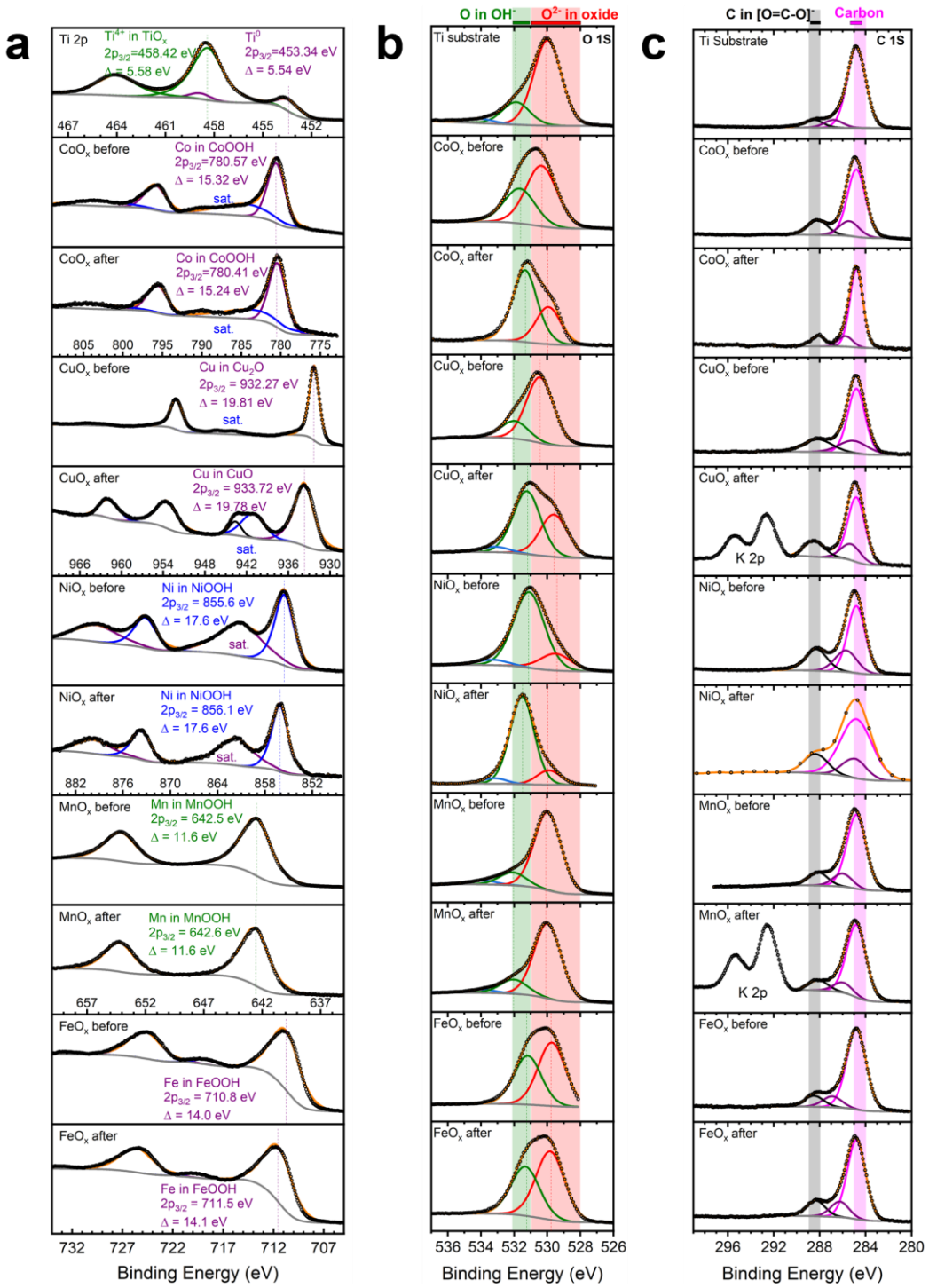

Figure 2.8: (a) 2p region of the various transition metal oxides, (b) O 1s region, and (c) C 1s region of the XPS spectra of the Ti substrate, CoO_x, CuO_x, NiO_x, MnO_x, and FeO_x electrocatalysts prepared through 100 LSVs before and after testing for methane electrochemical oxidation.

2.4.3 Electrocatalytic performances for partial methane oxidation.

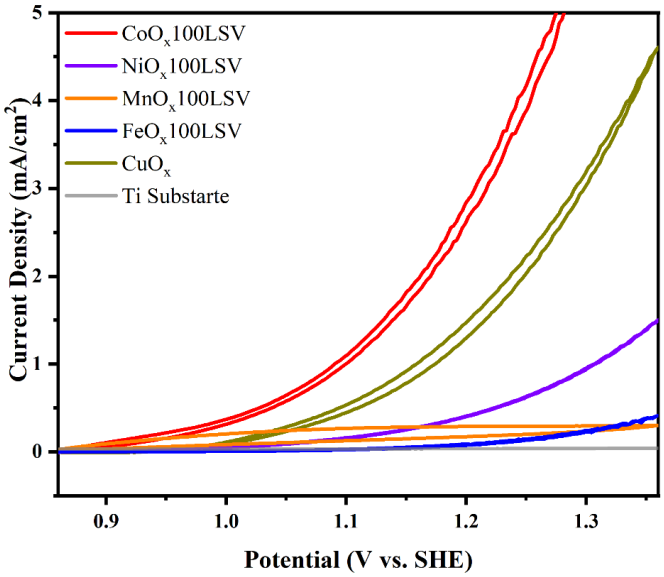

Figure 2.9: CV profiles of electrodeposited CoO_x, NiO_x, MnO_x, and FeO_x of 100 LSV along with CuOx and titanium substrate under rotational speed: 800 rpm, and temperature: 17oC.

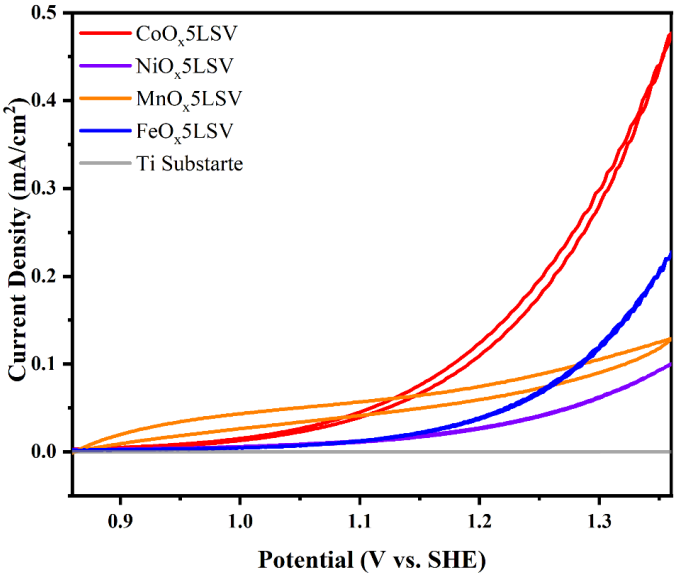

Figure 2.10: CV profiles of electrodeposited CoO_x NiO_x, MnO_x, and FeO_x of 5 LSV along with titanium substrate under rotational speed: 800 rpm, and temperature: 17oC.

The electrocatalytic activities of different transition metal oxides for the electrochemical partial oxidation of methane were studied in 0.1 M K_2CO_3. Figure 2.9 and Figure 2.10 show the potential vs current response of the (oxy)hydroxides electrodeposited by 100 and 5 LSV cycles, respectively. Under high catalyst loading (100 LSV cycles), CoO_x was found to be the most active

among these electrocatalysts. CuO_x was the second most active electrocatalyst. Although NiO_x, MnO_x, and FeO_x are less active, their electrocatalytic performances are still higher than the titanium cylinder electrode substrate. The low activity of the MnO_x and FeO_x catalysts might be due to the high catalyst loadings and high film thickness which results in a non-conductive film.[83, 104] When lower catalyst loadings (5 LSV cycles) were used, CoO_x was still the most active catalyst (Figure 2.10) although the current densities are more than an order of magnitude lower compared to the film deposited using 100 LSV cycles. At lower loading FeO_x becomes the second most active electrocatalyst at high overpotentials with an activity similar to that of the NiO_x catalyst. MnO_x, on the other hand, shows a highly resistive behavior while drawing oxidative currents already at less positive potentials compared to the other transition metal (oxy)hydroxides. All the electrocatalysts show higher current densities than the titanium substrate. No efforts have been made here in normalizing activity to the electrochemical surface area (ECSA), as the ECSA cannot be determined in a reliable manner on the titanium cylinder substrate. The current-potential response of the various transition metal (oxy)hydroxide films does not change significantly under an Ar or CH_4 atmosphere although the open circuit potentials are become a few millivolts less positive when the gas atmosphere is changed from Ar to CH_4. Figure 2.11 shows a representative current-potential response for a CoO_x film under a CH_4 and Ar atmosphere.

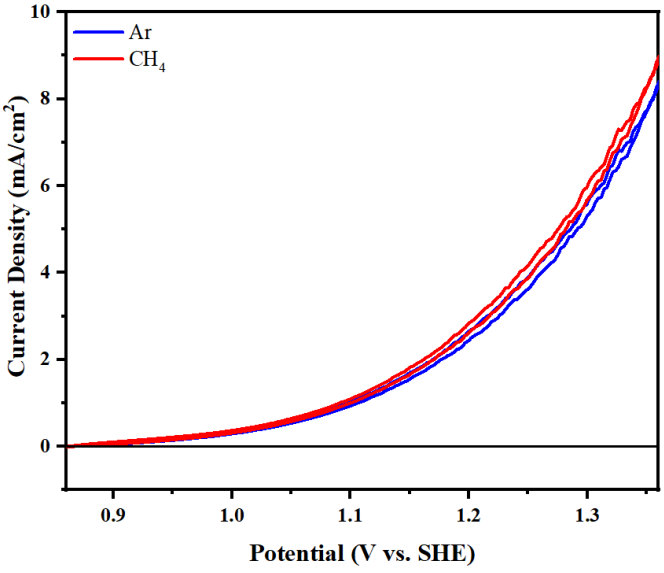

Figure 2.11: CV profiles of electrodeposited CoOx under rotational speed: 800 rpm, catalyst loading: 100 cycles of LSV, and temperature: 17°C.

2.4.4 Product analysis of electrochemical methane oxidation reaction.

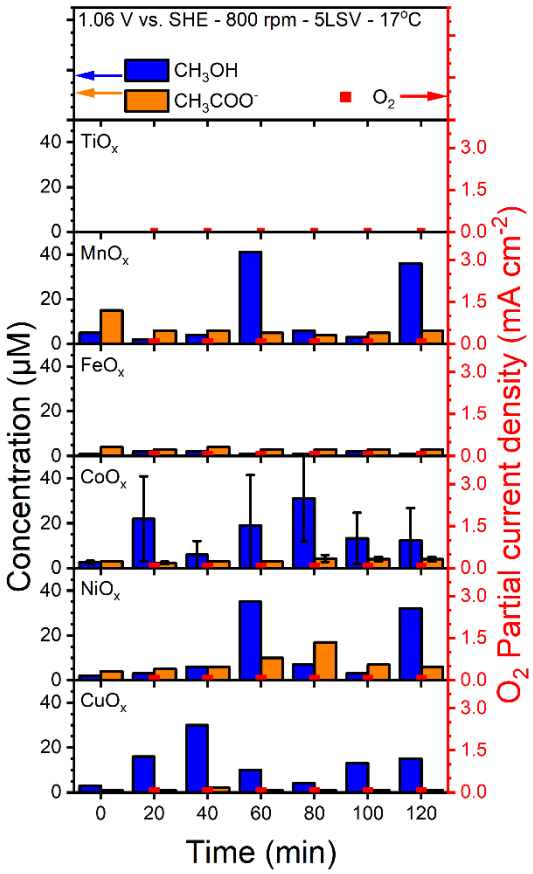

Figure 2.12: Production distributions of methanol and acetate on different transition metal oxides, TiO_x, MnO_x, FeO_x, CoO_x, NiO_x, and CuO_x, for electrochemical methane oxidation reaction at multiple reaction times (20 minutes intervals) within two-hours experiments using chronoamperometry performed at 1.06 V vs SHE under rotational speed: 800 rpm, catalyst loading: 5 cycles of linear sweep voltammetry, and temperature: 17°C.

Product analysis using NMR shows methanol and acetate are the major products during the electrochemical partial oxidation of methane on the various transition metal (oxy)hydroxides at a potential of 1.06 V vs SHE (Figure 2.12). By collecting and analyzing samples at 20-min intervals, we have observed fluctuations in the concentration of the liquid products over time. These fluctuations reveal the dynamic nature of partial oxidation studies in the RCE cell as the produced methanol accumulates in the bulk of the electrolyte and can be further oxidized over time.

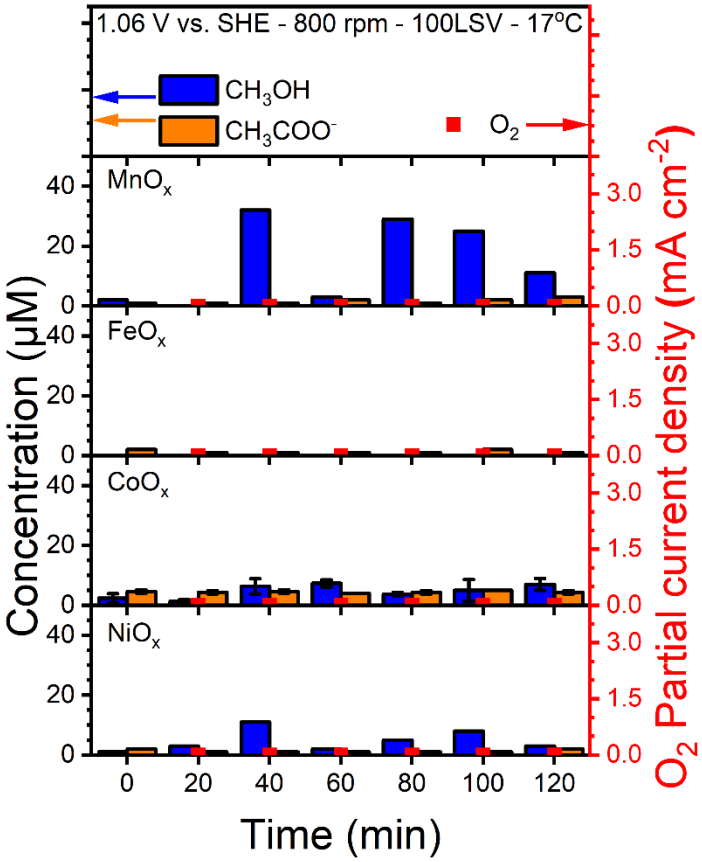

Figure 2.13: Production distributions of methanol and acetate on different transition metal oxides, MnO_x, FeO_x, CoO_x, and NiO_x, for electrochemical methane oxidation reaction at multiple reaction times (20 minutes intervals) within two-hours experiments using chronoamperometry performed at 1.06 V vs SHE under rotational speed: 800rpm, catalyst loading: 100 cycles of linear sweep voltammetry, and temperature: 17°C. The data for CuO_x and TiO_x are not shown as these films are not deposited by oxidative linear sweep voltammetry and their catalytic activity are already shown in Figure 2.12.

Two different thickness of the various transition metals were tested. Catalysts deposited using more linear sweep cycles result in lower methanol and acetate concentrations at the same applied potential. Methanol production for films prepared by 100 LSV cycles of the different oxides are shown in Figure 2.11. Among all the electrocatalysts tested, CoO_x, NiO_x, MnO_x, and CuO_x are found to be active to produce methanol and acetate while FeO_x produces O_2 and the titanium substrate (TiO_x) is largely inactive. Although the FeO_x catalyst can generate reactive oxygen species and evolve oxygen, the catalyst either does not activate methane or oxidizes it completely to CO_2 which cannot be measured accurately in our system due to the dissolution of CO_2 in the alkaline carbonate electrolyte and the ubiquitous CO_2 background signal from the CO_2 and

carbonate buffer equilibrium observed in the GC. Measurement of the electrolyte pH before and after testing shows a decrease in pH of between 0.08 and 0.1 pH units when methane is the reactive gas for all the transition metals including FeO_x. This pH drop is not observed when Ar is flowed through the cell in control electrolysis experiments even when the current densities are similar. The decrease in pH in the Argon control electrolysis experiments is below 0.01 pH units and within the pH meter experimental error. This suggests that methane is indeed oxidized on all the transition metal oxides under the applied potential of 1.06 V vs SHE although no significant amounts of methanol are observed for the FeO_x film. We have not made any attempts to quantify CO_2 from the decrease in pH in the electrolyte.

Interestingly, at the beginning of the methane partial oxidation experiments (t=0 min), methanol and acetate are already detected although at low concentrations indicating that the production of methanol and acetate is thermodynamically favorable even before the application of oxidative potentials due to the likely participation of thermal reactions between the methane and the electrodeposited metal (oxy)hydroxide. Figure 2.14 shows the ^1H NMR spectra as a function of time for two experiments carried out at two different potentials for a CoO_x catalyst. Before the start of the chronoamperometry experiments, a similar amount of acetate and methanol can be observed in both experiments. These products come from the chemical reaction of methane with the electrodeposited film. At a less negative applied potential of 0.8 V vs SHE (Figure 2.14a), the methanol concentration remains low and fluctuates over time although the changes in concentration are not significant while the acetate concentration increases over the first 60 minutes of the experiment and then decreases to reach again a second maximum at the end of the experiment.

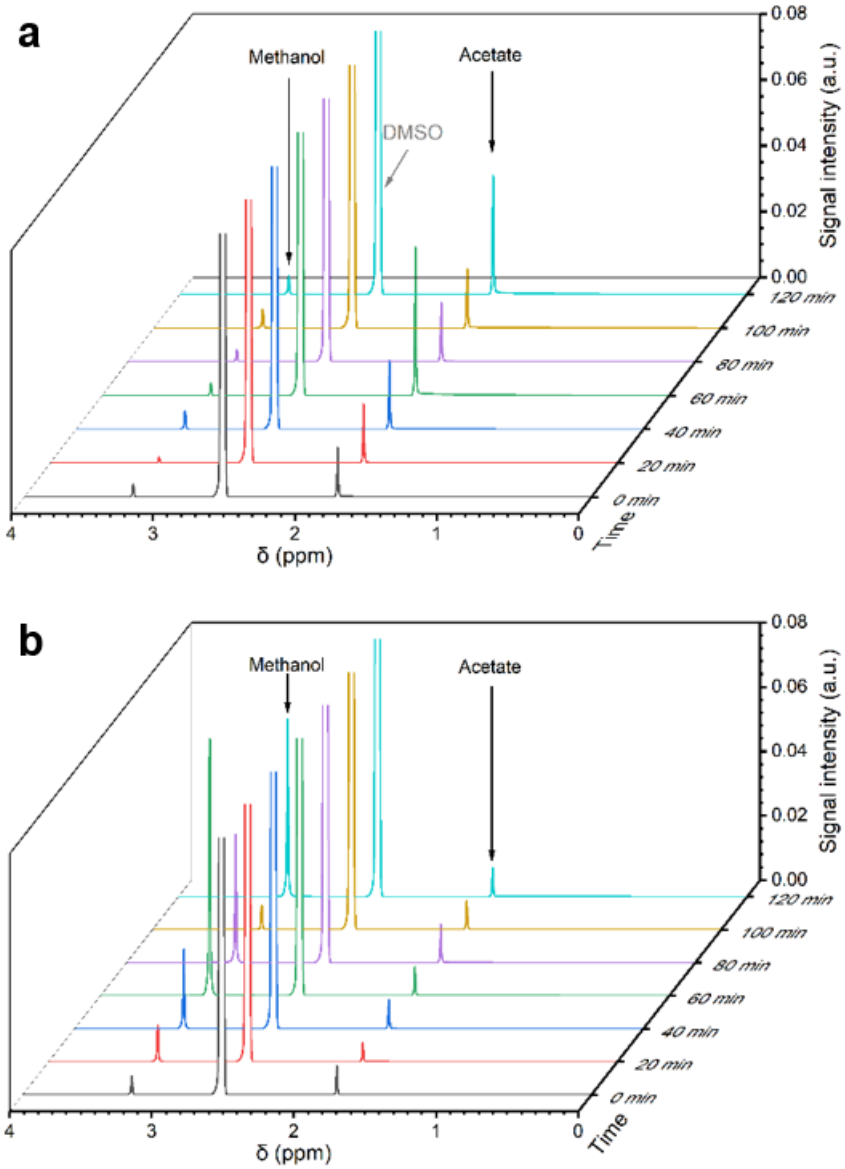

Figure 2.14: NMR spectra for liquid products of electrochemical partial oxidation of methane on electrodeposited CoO_x taken at 20-minute interval (a) under an applied potential: 0.8 V vs. SHE, rotational speed: 800 rpm, catalyst loading: 100 LSV, and temperature: 17°C and (b) under an applied potential: 1.06 V vs. SHE, rotational speed: 800rpm, catalyst loading: 5 LSV, and temperature: 17°C.

At higher applied potentials of 1.06V vs SHE (Figure 2.14b), the acetate concentration remained low over the duration of the experiment while the methanol concentration increased and also reached a maximum at 60 min. The methanol concentration then decreased almost to the initial values and then increased again for the last sample at 120 min. The generation of methanol

and further oxidation makes the determination of faradaic efficiencies difficult as the net rates of methanol formation cannot be measured.

2.4.5 Control experiments to separate thermal from electrochemical contributions and potential contamination.

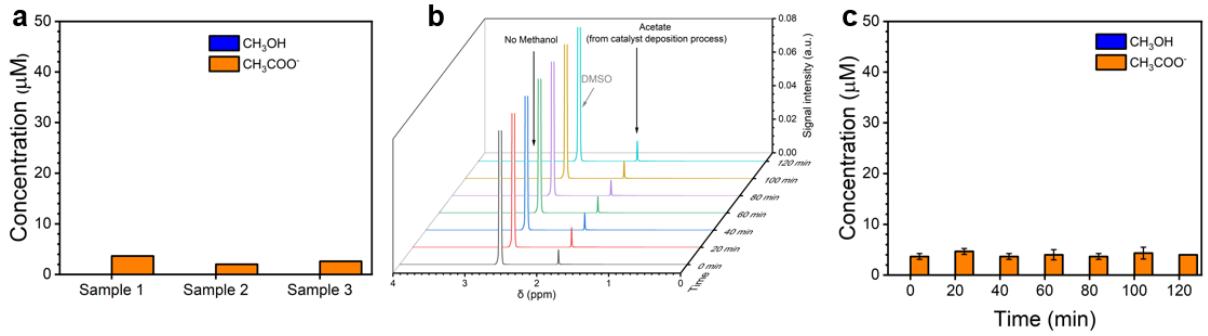

Figure 2.15: Control experiments. Concentration of acetate and methanol for control experiments where (a) three different CoOx films (100 LSV) were dissolved in 2M HCl, and (b) Production distributions of methanol and acetate on CoOx under Argon atmosphere at multiple reaction times (20 minutes intervals) within two-hours experiments using chronoamperometry performed at 0.86 V vs SHE under rotational speed: 800rpm, catalyst loading: 100 cycles of linear sweep voltammetry, and temperature: 17°C.

Our first reaction after observing methanol and acetate before the application of any electrochemical bias was to check for potential sample contaminations. Seeing also methanol and acetate across most of the oxides tested prompted us to run additional control experiments. The electrodeposition bath for the oxides contained acetate so we set out to determine whether the acetate observed could come from the deposition bath and if that was the case, what concentrations could be expected. To quantify acetate carried over from the electrodeposition bath to the catalytic experiments, we dissolved three different freshly prepared cobalt oxide films (deposited using 100 LSVs) each in 2 mL of a 2 M HCl and diluted the resulting solution with electrolyte until reaching the same volume as that used in the working electrode compartment of the RCE cell. We then proceeded to carry out NMR the same as any of the other samples. Figure 2.15a shows the result of the NMR quantification for the three dissolved CoO_x films. Indeed, concentration as high as 4 M of acetate can be assigned to acetate trapped in the CoO_x catalyst film during electrodeposition. Importantly, no methanol was observed in the dissolved films

indicating that the methanol observed before the start of the experiments comes from the reaction of methane with the catalyst film and is not due to any potential contamination arising from the liquid product quantification process. For comparison, depending on the applied potential, acetate concentrations as high as 17 μM were observed in the methane partial oxidation experiments for the CoO_x electrocatalysts deposited by 100 LSV (Figure 2.17a). These are concentrations almost 4 times higher than those that could be assigned to the acetate from the electrodeposition bath. NMR samples were also collected for constant potential experiments under Ar flow (Figure 2.15b and Figure 2.15c) as a function of time. Traces of acetate were observed for the Ar control experiments in agreement with the acetate concentrations expected to come from the catalyst electrodeposition bath while methanol was not observed. Figure 2.15b shows a representative NMR spectrum for control experiments run under an Argon atmosphere at an applied potential of 0.86 V vs SHE. The absence of the methanol signal in the NMR spectra confirms that methanol is only produced when methane is present in the system. Control experiments under Ar were run in triplicate and the average concentration of acetate as a function of time was averaged and plotted in Figure 2.15c. Concentrations of acetate below 5 μM at the beginning of the experiment and over the two hours of experiment under Ar flow can thus be assigned to acetate from the electrodeposition bath.

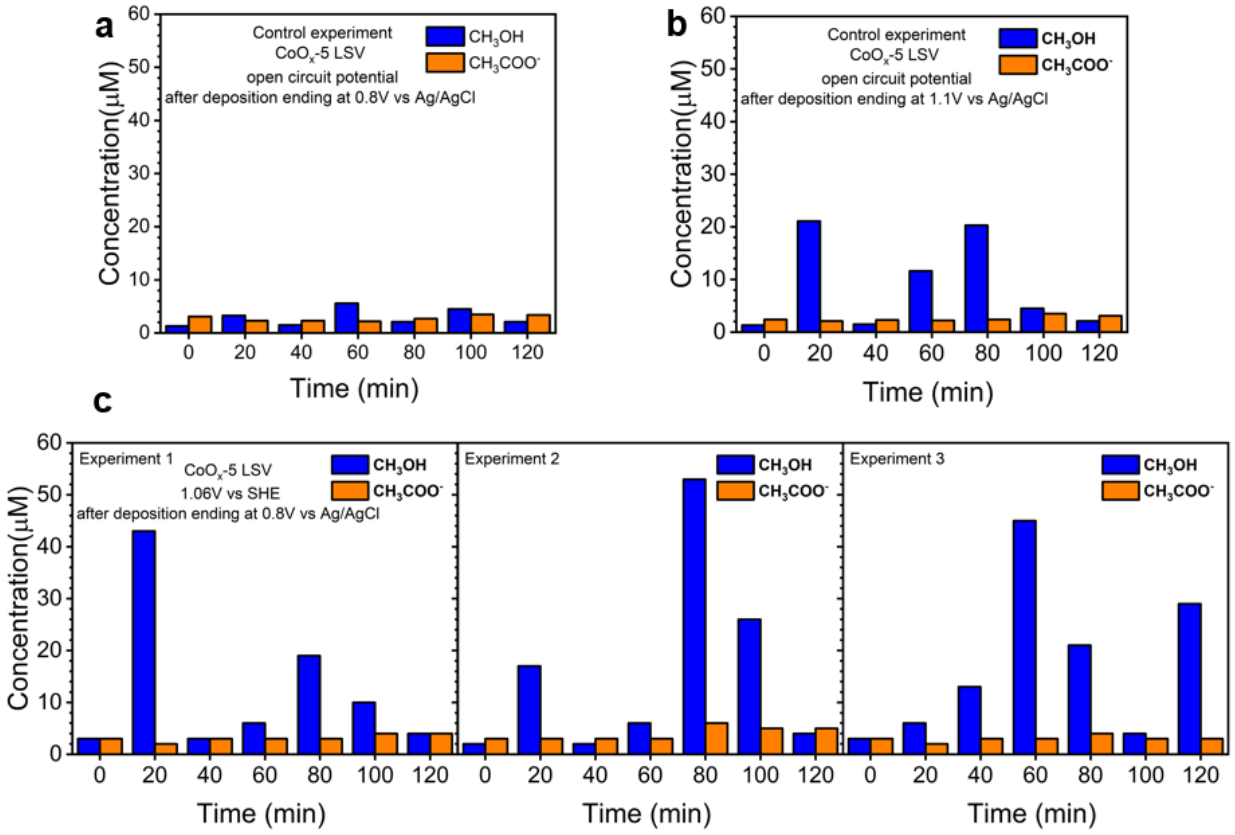

Figure 2.16: Production distribution of methanol and acetate on electrodeposited cobalt oxides CoO_x as a function of time during the partial oxidation of methane at open circuit and under applied potential. Conditions: 800rpm, catalyst loading: 5 LSVs, temperature: 17°C. (a) Open circuit potential for CoO_x catalyst electrodeposited by ending the deposition cycle at a potential of 0.8V vs Ag/AgCl, (b) Open circuit potential for CoO_x catalyst electrodeposited by finishing the deposition potential at 1.1 V vs Ag/AgCl, and (c) three catalyst prepared similarly to the catalyst in (b) but tested at a constant potential of 1.06 V vs SHE.

Since methanol is not generated in experiments carried out without the use of methane, we proceeded to understand the origin of the methanol observed at the start of each experiment before the application of potential. Indeed, thermal reaction of methane with surface oxides has been suggested as the rate limiting step in methane activation even for electrochemical based reactions with minimal applied potential dependence.[82] The large number of reports that imply faradaic efficiencies for methane partial oxidation above 100% also lead us to think that methane can be chemically reacting with activated oxide sites in the catalyst film. To determine whether this is unique to our oxidative electrodeposited catalysts, we ended the linear sweeps used during

electrodeposition not at the most positive potential of 1.1 V vs Ag/AgCl but at the less anodic potential of 0.8 V vs Ag/AgCl where the electrodeposited films are at a less oxidized state. It is well known that the transition metal oxides of cobalt, copper, iron, manganese, nickel and titanium are electrochromic and that these electrochemically oxidized materials can store high oxidation states over long periods of time. In effect, when the electrodeposition of the film was ended at the less oxidative potential of 0.8 V vs Ag/AgCl, these films did not show significant methane oxidation products in control experiments with no applied potential (Figure 2.16a). Concentrations of methanol of just up to 5.6 μM were observed. In comparison, when the electrodeposition of the film was ended at 1.1 V vs Ag/AgCl, methanol concentration of up to 22 μM where observed for experiments with no applied potential (Figure 2.16b). Importantly, the fluctuations in concentrations over time were also observed with methanol disappearing after 80 minutes of experiment without any applied potential. This indicates that the electrodeposited films store high oxidation states and that these states are trapped for periods of times long enough for the film to be washed with deionized water and dried after electrodeposition and left on the bench of the lab under an air environment until the start of the methane oxidation experiments in the RCE cell. Indeed, these oxidation states are long lived and active enough to drive thermochemical methane oxidation upon being put in contact with the dissolved methane. It is also likely that the only mechanism for the reduction of the high valence oxidation states in the electrodeposited films is by reacting with methane. For comparison, Figure 2.16c shows three similar CoO_x catalysts tested at an applied potential of 1.06V vs SHE. Under these conditions, concentrations of up to 53 μM are observed in one of the experiments while in the other two experiments the maximum methanol concentrations were 43 and 45 μM. Therefore, up to half of the methanol produced can be assigned to the thermal oxidation of methane by high oxidation states in the as-prepared CoO_x catalyst. We hypothesize that this is not unique to our catalysts and could explain the Faradaic efficiencies of over 100% for methane electrochemical oxidation observed in other systems. Non-electrochemical transformation of methane to methanol under open circuit conditions at

temperatures of 300 ^{o}C or higher have been previously reported to proceed via redox cycles on transition metal oxides where methane is oxidized by active oxygen species formed on the catalyst surface.[105] The contribution of non-electrochemical methane oxidation processes, however, is rarely considered as a possibility in ambient temperature electrochemical cells.

In order to gain a better fundamental insight of the electrochemical and thermal steps involved in the partial oxidation of methane, the effects of various factors including applied potential, operating temperature, catalyst loading, electrolyte compositions, and rotational speed on methanol selectivity were systematically studied. Since cobalt oxide (CoO_x) is a well-known catalyst with methane partial oxidation activity, well-characterized redox properties, and active oxygen species,[83, 104] we have selected it as a prototypical electrocatalyst to understand mass, charge and heat transport phenomena involved in methane partial oxidation.

2.4.6 Catalyst loading (porosity).

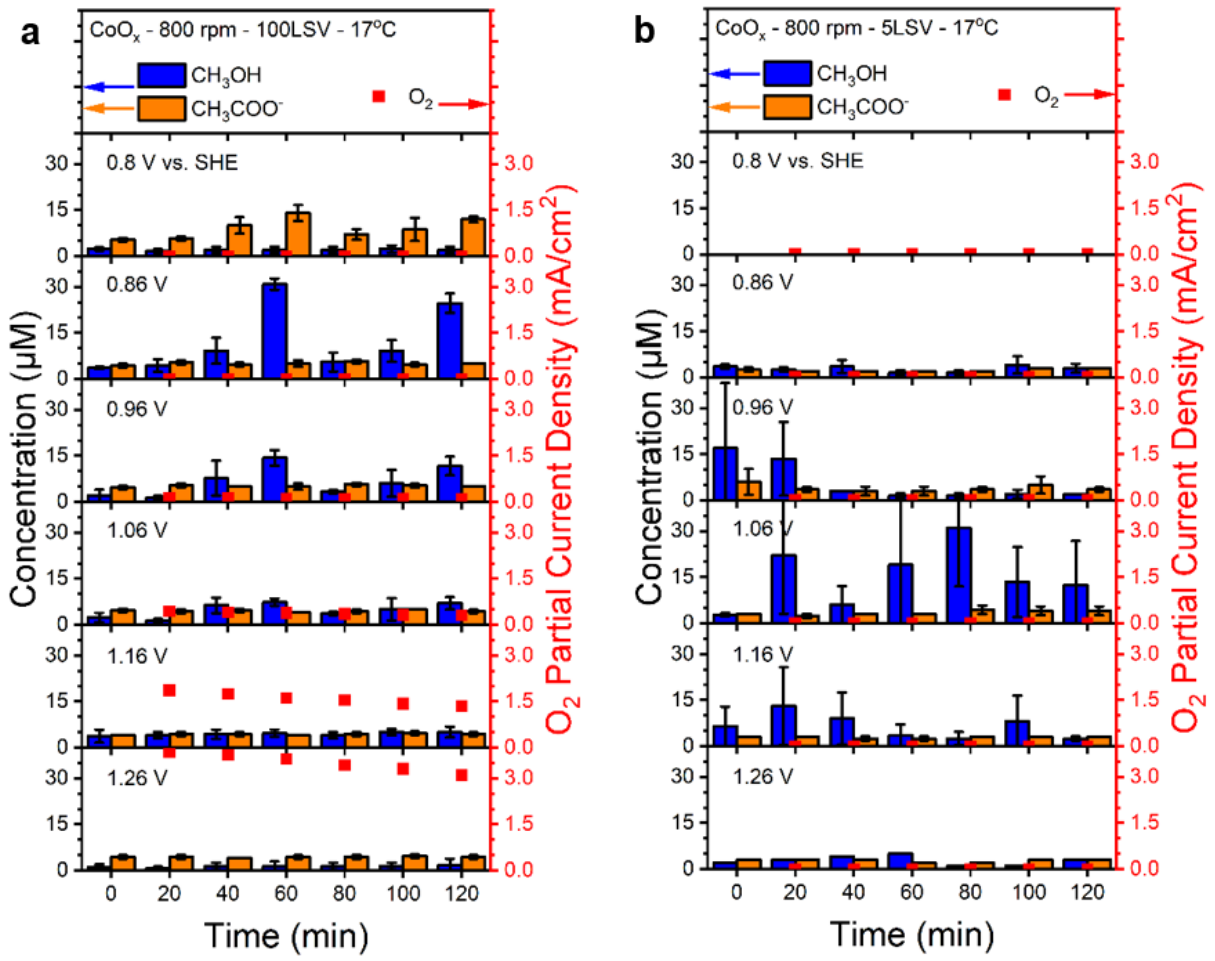

Figure 2.17: Production distributions of methanol and acetate on cobalt oxides, CoOx, for the electrochemical partial oxidation of methane at multiple reaction times (20 minutes intervals) within two-hours experiments using chronoamperometry performed at different applied potentials: 0.8, 0.86, 0.96, 1.06, 1.16, and 1.26 V vs SHE under rotational speed: 800rpms, temperature: 17°C with (a) catalyst loading: 5 cycles of linear sweep voltammetry and (b) catalyst loading: 100 cycles of linear sweep voltammetry.

In our setup, the amount of electrodeposited transition metal (oxy)hydroxides can be controlled by changing the number of electrodeposition cycles.[83] The loadings of the catalytic film as well as its morphology and conductivity is expected to affect the degree of electrochemical oxidation of methane and its overoxidation. Higher porosity is expected to increase the tortuosity for the transport of methanol out of the catalyst film. Two different catalyst loadings (deposited by 5 and 100 LSVs) were used to explore the relationship between methanol selectivity and mass and charge transport phenomena within the catalyst film. Low catalyst loadings corresponding to

thinner catalyst films require applied potentials of at least 0.96 V vs SHE to activate methane and accumulate methanol in the RCE cell at concentrations of at least 10 μM (Figure 2.17b). At less oxidative potentials (0.8~0.86 V), only trace amounts of methanol and acetate are detected. The detection of appreciable amounts of methanol only occurs at potentials of 0.96 to 1.16 V vs SHE, and more positive potentials lead to the overoxidation of methanol. In comparison, the thicker catalyst film obtained through the deposition of the CoO_x film with 100 LSV required more modest potentials (0.8~0.86 V vs SHE) to activate and oxidize methane (Figure 2.17a). As the potential was biased to more oxidative windows, the concentration of methanol and acetate substantially decreased until methanol is only present at trace amounts. The onset for the oxygen evolution reaction also requires lower overpotentials for the thicker films in agreement with the OER literature where cobalt has been shown to be active across the bulk phase of the catalyst film.[106, 107] Therefore, thicker catalyst films or more catalyst loadings lead to both faster methane activation at low overpotentials as well as higher methanol overoxidation at high overpotentials. Higher overoxidation of methanol at potentials of 1.06 V vs SHE for the thicker film compared to the thinner film is due to the highly porous structures and thus the longer paths for methanol to exit the thicker catalyst layer. The trapping of bubbles on the catalyst films was not observed at the potentials tested. In any future application, an optimal point between applied potential and catalyst thickness must be determined for porous transition metal (oxy)hydroxides if these are to be used as catalyst for the methane to methanol transformation.

2.4.7 Applied potential.

The driving force for the partial oxidation of methane and the overoxidation of methanol changes as the applied potential is increased. At low applied potentials of around 0.8 V vs SHE, acetate is preferentially accumulated in the electrochemical cell for the thicker CoO_x films (Figure 2.17a). This indicates that although the activation of methane occurs readily, the activated methane intermediate likely reacts with the carbonate or the CO_2 generated from the complete oxidation of methane to produce acetate. At potentials higher than 0.86 V vs SHE, the selectivity

changes to methanol reaching a maximum accumulation of methanol at intermediate overpotentials. Higher overpotentials lead to the complete oxidation of methanol as corroborated by the decrease in the pH at the end of the experiments while the pH does not change in experiments under Ar flow. Higher applied potentials indeed modify the density of high valence oxidation states available for catalysis which are also needed to conduct charges in the porous transition metal (oxy)hydroxide films. Therefore, electrochemical partial oxidation of methane to methanol should be more favorable at relatively intermediate overpotentials where enough of the higher oxidation states of the catalysts are present on the surface of the catalyst but before the oxygen evolution reaction becomes dominant at high overpotentials.

2.4.8 Electrolyte composition.

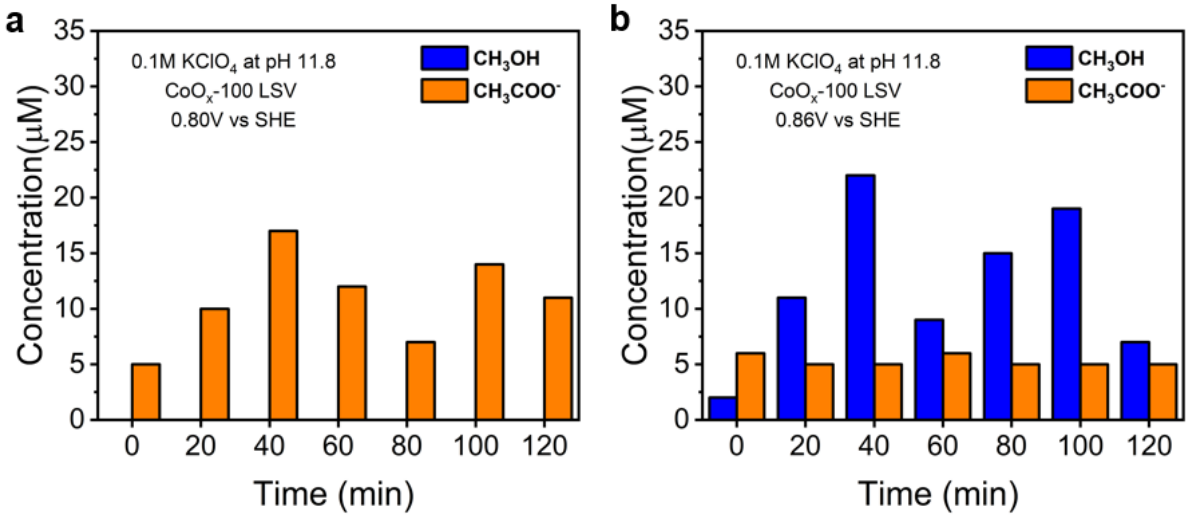

Figure 2.18. Production distribution of methanol and acetate on electrodeposited cobalt oxides CoOx as a function of time during the partial oxidation of methane in a 0.1M $KClO_4$ electrolyte at pH 11.8 for applied potentials of (a) 0.8 V and (b) 0.86 V vs SHE. Conditions: 800rpm, catalyst loading: 100 LSVs, temperature: 17°C.

An emerging question is whether carbonate ions fulfill the role of mild oxidants and oxygen atom donors during the oxidation of methane. To determine if carbonate ions are indeed needed for the oxidation of methane to acetate and methanol, control experiments were carried out in a potassium perchlorate electrolyte with pH adjusted to that of the carbonate electrolytes (pH=11.8). Figure 2.18 shows the product distributions at two potentials for a 100 LSV CoO_x film. The

production of acetate and methanol is similar as those in experiments with the carbonate electrolyte. Therefore, is safe to conclude that carbonate ions are not the predominant oxygen donor sources during methane electrochemical partial oxidation in transition metal (oxy)hydroxides and are not involved in the reaction mechanism.

2.4.9 Rotation speed.

The RCE cell allows the study of electrocatalytic reactions under well characterized mass transport. The effect of the rotation of the electrode in the methane partial oxidation rates has also been considered here. By tuning the rotation of the electrode, mass transport can be systematically changed to modify the thickness of the boundary layer for the transfer of reactants and intermediates in and out of the electrocatalytic surface.

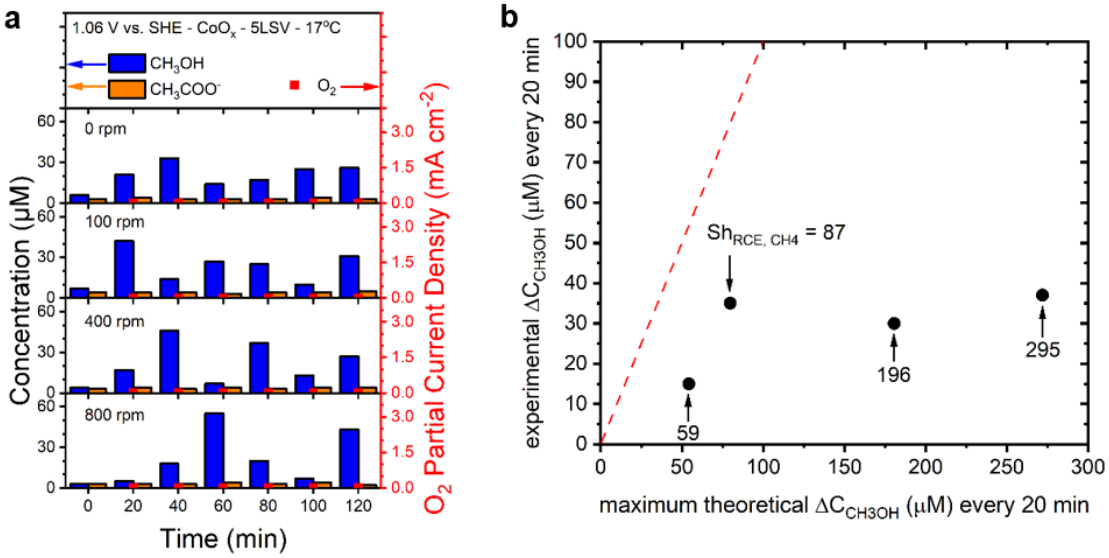

Figure 2.19: (a) Production distributions on cobalt oxides, CoOx, for electrochemical partial oxidation of methane at multiple reaction times (20 minutes intervals) within two-hours experiments using chronoamperometry performed at 1.06 V vs SHE under different rotational speed: 0, 100, 400, and 800rpms, catalyst loading: 5 LSV, and temperature: 17°C. Current vs potential curves are shown in Figure 2.20. (b) Experimental versus maximum theoretical methanol accumulation rates in the RCE cell.

As shown in Figure 2.19a, the highest concentrations of methanol during the two-hours experiments at rotation speeds of 0, 100, 400, and 800 rpms are 33, 42, 46, and 55 μM, respectively. Lower rotation speeds or static electrodes are limited by mass transport of methane to the electrode surface which leads to the accumulation of lower concentrations of methanol in

the cell. However, the concentration of the methanol accumulated in the cell remains rather constant and does not fluctuate as much as for higher rotation speeds. The electrolyte volume in the working electrode compartment is 84 mL while the electrode area is just 3 cm^2. Under low rotation speeds, the methanol accumulated is not forced to pass by the electrode surface preventing its further oxidation. On the other hand, while higher rotation speed contributes to higher methanol concentrations by ameliorating the mass transport of methane to the electrode, it also contributes to the faster further oxidation of methanol resulting in large fluctuations in the methanol concentrations observed as a function of time. The rather constant concentration of methanol observed at low rotations speeds is what would be expected in a system with two consecutive reactions where the methanol is the reaction intermediate. At some time, the rate of methanol production should match that of methanol overoxidation and reach a steady-state concentration. This makes the cyclic nature of the concentration of methanol at higher rotations speeds difficult to rationalize. An important metric can still be obtained by measuring the maximum change in methanol concentration in the 20 minutes sampling interval as the maximum mass transport limited rate of methanol production in the RCE cell under the different rotations is well characterized as shown in Figure 2.5. At rotations speeds of 100 rpm, equivalent to a $Sh_{RCE,CH4}$ value of 87, changes in concentration of as much as 28 M of methanol are observed in the 20-minutes interval between samples which approaches half of the maximum methanol production rate possible, indicating that close to 50% of the methane reaching the surface of the electrode is transformed effectively to methanol (Figure 2.19b).

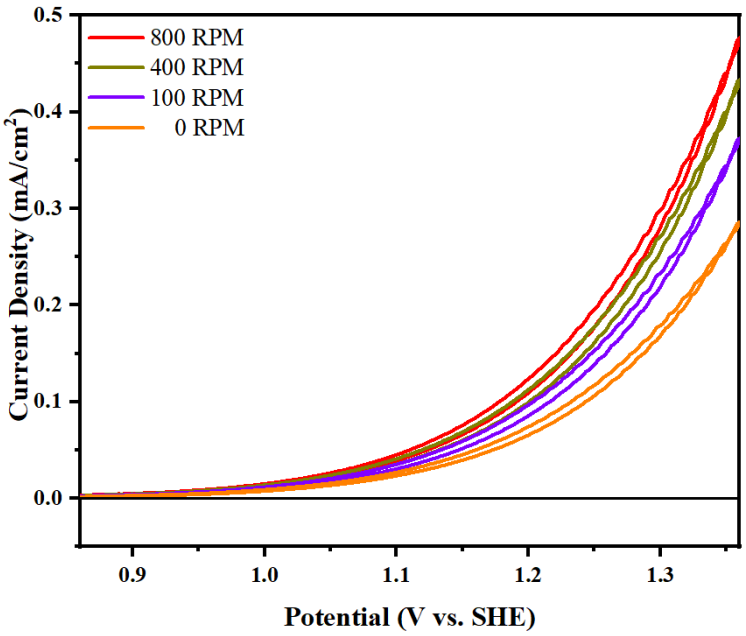

Figure 2.20: CV profiles of CoOx under rotational speed: 0 rpm, 100 rpm, 400 rpm and 800 rpm, catalyst loading: 5 cycles of LSV, and temperature: 17°C.

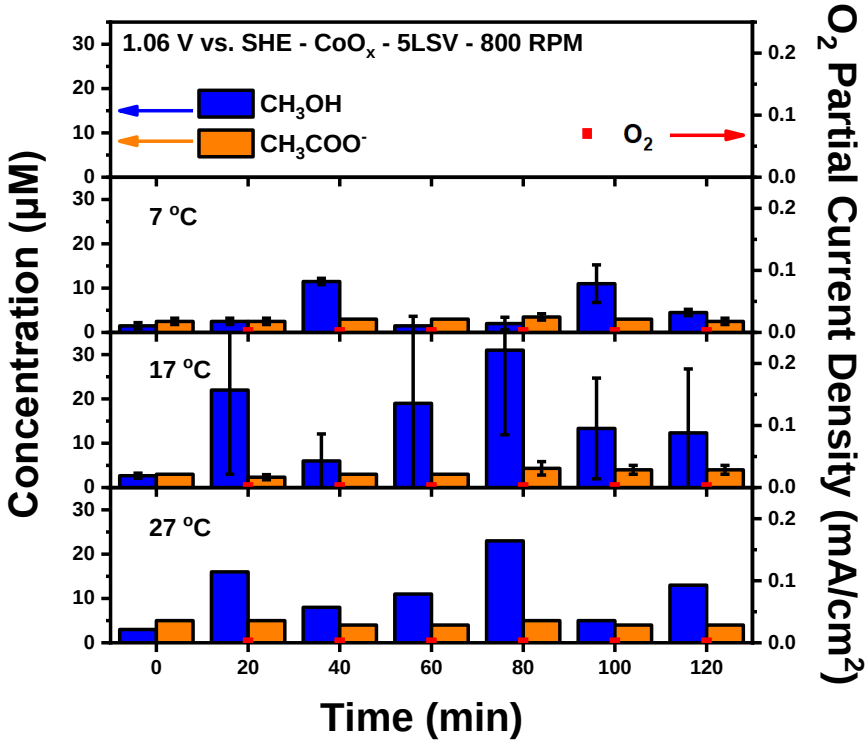

Figure 2.21: Temperature dependence of the production distributions of methanol and acetate on cobalt oxides, CoO_x, for electrochemical partial oxidation of methane. Samples are collected at 20 minutes intervals within a two-hours experiment. Chronoamperometry is performed at 1.06 V vs SHE under rotational speed of 800rpms, catalyst loading: 5 cycles of linear sweep voltammetry, and different temperature: 7, 17, and 27°C. Current vs potential responses at various temperatures are shown in Figure 2.23.

At this stage, the reason for the fluctuation of the methanol and acetate concentrations as a function of time is not clear. Methanol is never observed in the cathode compartment, so we disregard the possibility for time dependent transport or crossover of methane-derived species back and forth between the anode and the cathode compartments (Figure 2.22). Only trace amounts of acetate below the limit of quantification are observed in the anode compartment as these charged species can be transported through the anion conductive membrane. Acetate, however, is the minority charge carrier in the alkaline electrolyte. Computer fluid dynamics of the electrolyte in the RCE cell indicate the formation of different convection zones in the cell.[108] As expected, the energy introduced through the rotation of the electrode is mostly dissipated within the hydrodynamic boundary layer of a few hundred micrometers around the rotating cylinder electrode. Over time, this energy is transferred to the bulk of the electrolyte increasing the convection in the cell. Convective patterns are disrupted by the bubbling of methane inside the electrolyte and by the interactions between the electrolyte and the walls of the cell. The dissipation of mechanical energy in the cell can indeed be reflected in the periodicity of the changes in the concentration of products but at this time these relations are purely speculative. Further multi-scale modeling of the reactor is expected to shine light into the relation between electrode rotation and product accumulation. We highlight that understanding of mass transport is of the outmost importance for the study of methane to methanol systems. The study of the direct oxidation of methane to methanol has been comprehensively investigated over the past decade; however, little research has taken mass transfer effect into account.

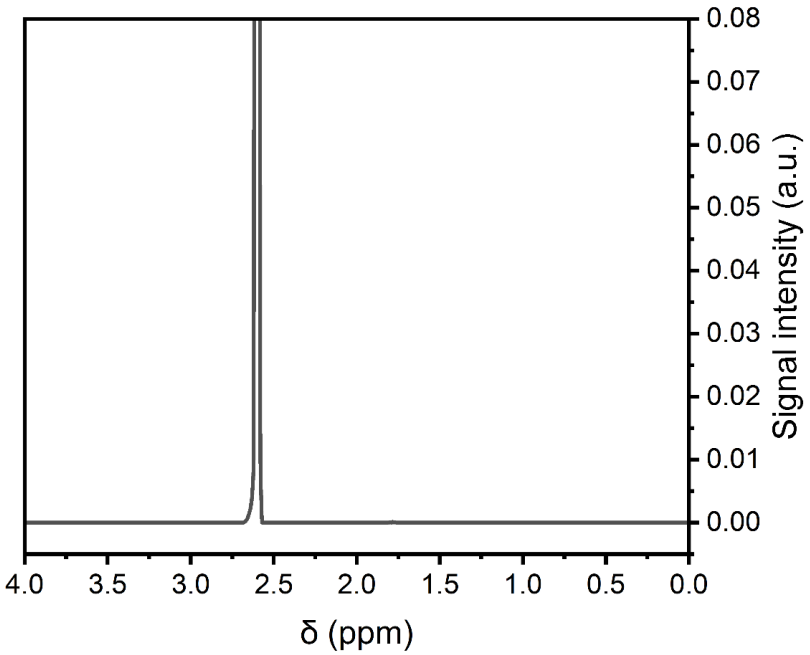

Figure 2.22: Representative NMR spectra for liquid samples taken from the cathode compartment of the cell during electrochemical methane oxidation experiments. No methanol is ever observed on the cathode compartment and only trace amounts of acetate below the limit of quantification are sometimes observed.

2.4.10 Operating temperature.

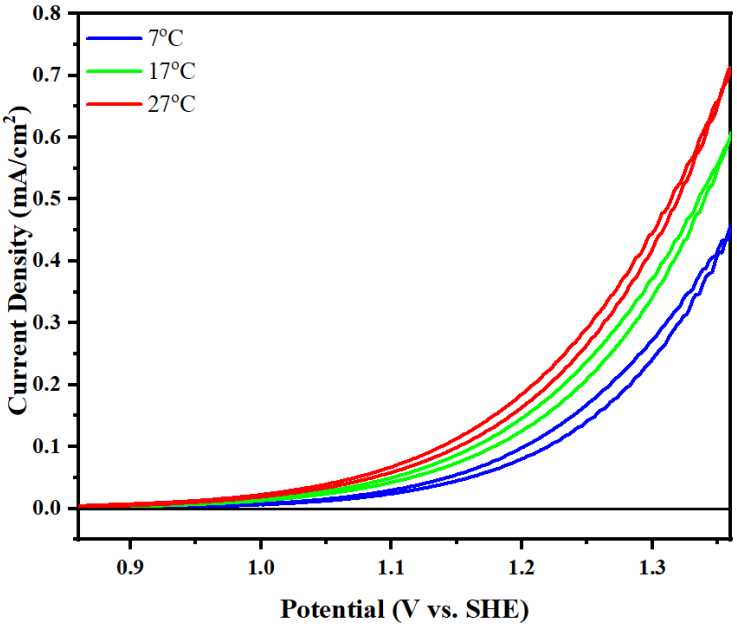

Figure 2.23: CV profiles of electrodeposited CoOx under rotational speed: 800 rpm, catalyst loading: 5 cycles of LSV, and temperature: 7°C, 17°C and 27°C.

The rate-limiting step in methane electrochemical oxidation can be the regeneration of the catalytic site, the transport of methane to the catalyst surface, the thermal activation of the C-H bond and its hydroxylation, or the desorption and removal of the methanol (Figure 2.1). Any of these processes is expected to be a function of temperature as higher temperatures can increase charge hoping in conductive oxides, the diffusion coefficient of methane in liquids, as well as increase the rates of methane activation and the endothermic desorption of methanol. Higher temperatures can also increase the rate of methanol overoxidation and thus temperature can be expected to have a complex effect on methane electrocatalysis. Figure 2.21 shows the dependence of the product distribution during the methane partial oxidation as a function of temperature. Three different temperatures were studied ranging from 7 to 27^{o}C to understand the role of thermal processes in the activation of methane and the overoxidation of methanol. Linear sweep voltammetry of the CoO_x catalyst at the different temperatures are shown in Figure 2.23. Higher temperatures correlate with higher current densities. At a lower operating temperature (7°C), the accumulation of methanol in the cell is lower potentially due to slower kinetics for methane oxidation as mass transport of methane to the surface at 800 rpm is not limiting. At lower temperatures, less thermal energy is available to overcome the activation barrier for C-H activation. At higher temperatures, the solubility of methane in the electrolyte decreases and could result in mass transport limitations although the diffusion coefficient for methane increases and the kinetics for both methane activation and methanol overoxidation could also increase. At temperatures of 17 and 27°C we indeed observed higher accumulation of the methanol and acetate products with higher concentrations reached at the intermediate temperature of 17°C. Moderate temperatures could be optimal for the transformation of methane to methanol to facilitate methane activation while limiting methanol overoxidation. The issue of the decrease in solubility of methane at higher temperatures can be circumvented either through the use of gas diffusion electrodes[109] or the application of higher partial pressure of methane.

2.4.11 Reaction mechanism via DFT calculation.

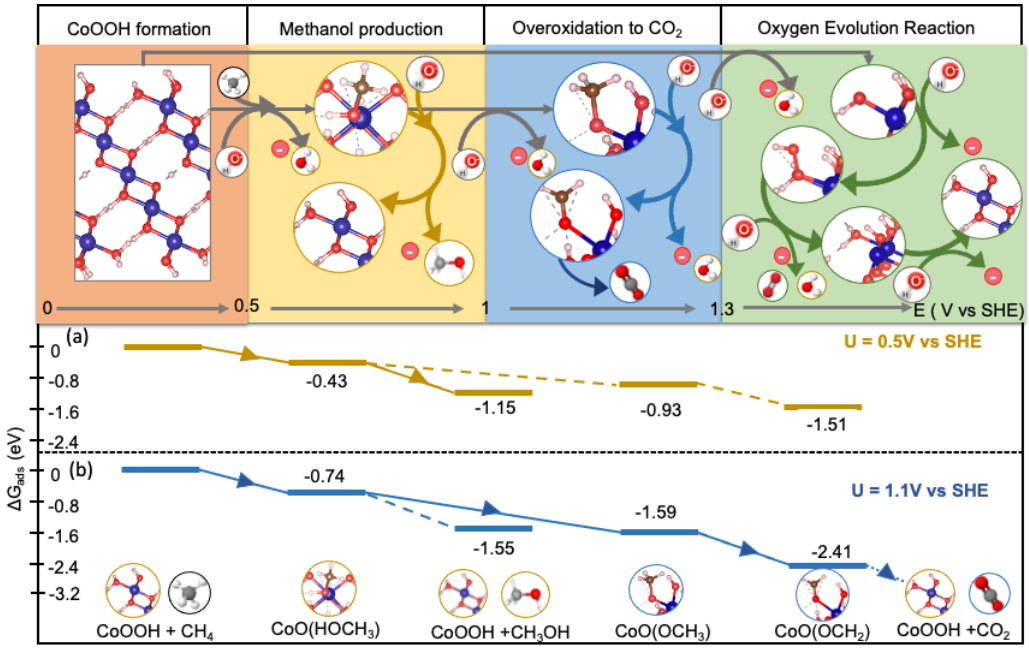

Figure 2.24: Reaction mechanism and reaction energy diagram at (a) U = 0.5 V vs SHE (b) U = 1.1 V vs SHE. The top panel shows the most favorable reactions at certain electrochemical potential windows. In the red box the CoOOH formation takes place starting from 0.5 V vs SHE.[91] The yellow box shows methanol production in the potential range of 0.5 – 1 V vs SHE after which the most favorable reaction would be the overoxidation of methane to CO_2 competing with the oxygen evolution reaction starting from U = 1.3 V vs SHE. The reaction diagrams are evaluated at pH = 12.

To understand the mechanism during the electrocatalytic methane oxidation process, DFT simulations were performed. The reaction mechanism and thermodynamic analysis are shown in Figure 2.24. The focus is on the main reaction pathway for methane to methanol and CO_2, while the side reaction dealing with acetate formation was not explored as it is the major product only in a very narrow potential window for the thicker CoO_x film. Understanding the Cobalt oxide stability in reaction conditions is the first step in this process. CoOOH is the most stable phase for Cobalt oxide that is observed in the potential range of U = 0.5 to 1.5 V versus SHE at highly alkaline pH.[90, 91] Therefore, we consider that the catalyst is CoOOH as soon as the potential reaches 0.5 V vs SHE. Experimentally, the formation of CoOOH was achieved by activating the surface by performing CV measurement and reaching potentials more positive than 0.5V vs SHE. The open circuit potential for CoO_x films after deposition and electrochemical activation were

indeed between 0.55 and 0.75 V vs SHE depending on the final potential applied during the activation cycle. The open circuit potentials also change upon the switch of the atmosphere from argon to methane. The activated surface then can perform partial oxidation of methane via the electrochemical reaction between methane and high oxidation states of the catalyst, even without an applied potential. Understanding the thermodynamic branching between various reaction mechanisms when the electrochemical potential is modified then becomes the primary objective of this section of the work. As CoOOH is only stable in the potential range of 0.5 – 1.5 V vs SHE at alkaline pH we have studied the various reactions in the same potential range. From our calculations, three main reaction mechanism are at play, the predominant one depending on the potential, as shown in Figure 2.24:

(a) Selective methane oxidation to methanol.

$$^{*}OH + CH_4 + OH^- \rightarrow CH_3OH + H_2O + e^- \quad (2.2)$$

$$^{*}CH_3OH + OH^- \rightarrow CH_3OH + {}^{*}OH + e^- \quad (2.3)$$

$$^{*}CH_3OH + OH^- \rightarrow {}^{*}OCH_3 + H_2O + e^- \quad (2.4)$$

In the initial potential window of 0.5 – 1 V vs SHE, where methanol formation is favored, the first reaction step is to activate the C—H bond of methane, and this happens electrochemically on the hydroxyl group of the CoOOH surface (Equation 2.2). Figure 2.24 (yellow zone) shows the reaction diagram of methane oxidation to methanol. At 0.5 V vs SHE (Figure 2.24a), we observe the electrochemical methane activation to be thermodynamically favorable (-0.43 eV). This step (Equation 2.2) combines electrochemical activation of the C-H bond of methane with OH^- and concerted rebinding of the CH_3 fragment with a surface adsorbed OH (*OH). The formed adsorbed *CH_3OH on the surface has two options (1) the CH_3OH group on the surface can desorb and the hydroxyl group on the surface can be replenished electrochemically by hydroxyl ion to give back the initial catalyst (CoOOH), represented in Equation 2.3, the *CH_3OH can further oxidize to *OCH_3 (Equation 2.4). We have studied both possibilities and observe that the selectivity between

the two reaction is potential dependent. At lower overpotential (< 1V vs SHE), electrochemical desorption of methanol is thermodynamically favorable (Figure 2.24a). As we move toward more positive potential (> 1V vs SHE), the methanol oxidation to $*OCH_3$ becomes more favorable. This can be seen on Figure 2.24b, where the potential (1.1 V) is just above 1V, and the $*OCH_3$ species (ΔG_{ads}= -1.59 eV) is becoming more stable than desorbed methanol and hydroxylated CoOOH surface site (-1.55 eV). Increase in potential causes the H on the methanol attached to the surface to become more acidic, which then reacts with a OH^- in the solution to produce $*OCH_3$ and water, which actively encourages the oxidation of $*CH_3OH$. At 1 V vs. SHE, the thermodynamic favorability of the two reactions switches. Thus, thermodynamics informs us that CoOOH behaves as an excellent catalyst for the selective oxidation of methane into methanol at an intermediate window of potential (0.5 – 1 V versus SHE), which is in good agreement with our experimental observations.

(b) Methane overoxidation to CO_2.

$$^*OCH_3 + OH^- \rightarrow {}^*OCH_2 + H_2O + e^- \quad (2.5)$$

$$^*OCH_2 \rightarrow \cdots \rightarrow CO_2\ evolution$$

As already mentioned above, if we go towards a sufficiently large overpotential, the surface methanol is overoxidized to $*OCH_3$ (above 1 V vs SHE, Figure 9 blue zone), $*OCH_3$ then oxidizes to $*OCH_2$, a step again thermodynamically favorable (Equation 2.5). These are the first steps toward the overoxidation of methane to CO_2 which is captured as carbonate in the alkaline electrolyte. The other favorable oxidation steps after $*OCH_2$ were not explicitly calculated here.

(c) Oxygen evolution reaction

$$^*OH + OH^- \rightarrow {}^*O + H_2O + e^- \quad (2.6)$$

$$^*O + OH^- \rightarrow {}^*OOH + e^- \quad (2.7)$$

$$^*OOH + OH^- \rightarrow {}^* + O_2 + H_2O + e^- \quad (2.8)$$

$$OH^- + {}^* \rightarrow {}^*OH + e^- \quad (2.9)$$

Finally, at sufficiently large overpotentials, we will observe the oxygen revolution reaction which would be directly competing with methane overoxidation to CO_2. The reaction mechanism for OER in alkaline conditions is given in the Equations 2.6 – 2.9. OER reaction on CoOOH has been extensively studied in the literature.[90-92] We find that the OER occurs at a potential on 1.28 V vs SHE in pH = 12 with the rate determining step (RDS) as the desorption of O_2 (Equation 2.8). This matches very well with what has already been reported by Curutchet *et al*.[94]

The competition between the OER process and the methane oxidation reaction for the active site is an essential element to consider in the reaction condition. Methane activation can interfere with OER intermediates at two different reaction stages. First, as seen above, surface *OH can be used to form $*OHCH_3$ (Equation 2.2), preventing their conversion into *O (Equation 2.6). Second, *O intermediates might interact with methane and OH^- to form $*OCH_3$ (Equation 2.10), preventing the formation of *OOH (through Equation 2.7).

$$^*O + CH_4 + OH^- \rightarrow {}^*OCH_3 + H_2O + e^- \quad (2.10)$$

Both reactions occur at high overpotentials and are thermodynamically favorable. For example, Equation 2.2 will have a ΔG of -0.8 eV at a potential of 1.3 V vs SHE, but Equation 2.6 will have a ΔG of -0.15 eV. Similarly, equation 10 will have a ΔG of -1.4eV at the same potential but Equation 2.7 will only have a ΔG of -0.1 eV. In any scenario, the two competing reactions mentioned above will have a significant impact on OER but have no impact on the formation of methanol at moderate overpotentials.

2.5 Discussion

From a thermodynamic perspective, the electrochemical partial oxidation of methane to methanol in alkaline electrolytes (Equation 2.11) requires a relatively low oxidative potential of only 0.18 V vs SHE at pH 14 compared to the oxygen evolution reaction (OER, Equation 2.12) which requires an additional 0.22V. Despite methane partial oxidation to methanol being thermodynamically accessible in an electrochemical cell, this reaction is kinetically difficult and

requires an adequate catalyst to reduce activation energy and a large overpotential to drive measurable partial current densities. Driving large enough currents often requires biasing the electrode to oxidative potentials at which oxygen evolution also takes place despite this reaction also being kinetically slow.

$$CH_4 + 2OH^- \rightleftharpoons CH_3OH + H_2O + 2e^- \; E^0 = 0.18V \quad (2.11)$$

$$2OH^- \rightleftharpoons 0.5O_2 + H_2O + 2e^- \qquad E^0 = 0.40V \quad (2.12)$$

At very high oxidative potentials, the oxygen evolution reaction outcompetes the methane oxidation reaction and oxygen or CO_2 are predominantly formed.[80] An often ignored fact is that high overpotentials are also needed to transport charges on porous oxide electrodes as these materials are electrically insulating and become conductive only when the population of high oxidation states in the catalyst film is high.[83, 110] This means that we cannot expect to see methane activation until transition metal (oxy)hydroxides become oxidized and conductive.

The first point is to form on the catalyst surface the right oxidation number at the considered transition metal for electronic conductivity and methane oxidation. Figure 2.25 shows the ranges of applied potentials vs SHE at which electrodeposited transition metal (oxy)hydroxides[83, 111] become conductive by changing the valence state from +2 to +3 for the Co, Ni, Fe, and Mn (oxy)hydroxides in 1 M KOH. At potentials positive of the water oxidation potential (0.4 V vs SHE in pH 14), many of these metal (oxy)hydroxides enter higher oxidation states and become active for both the methane partial oxidation reaction and the oxygen evolution reaction requiring somewhere between 250 and 500 mV overpotential to sustain meaningful oxidative currents.[83]

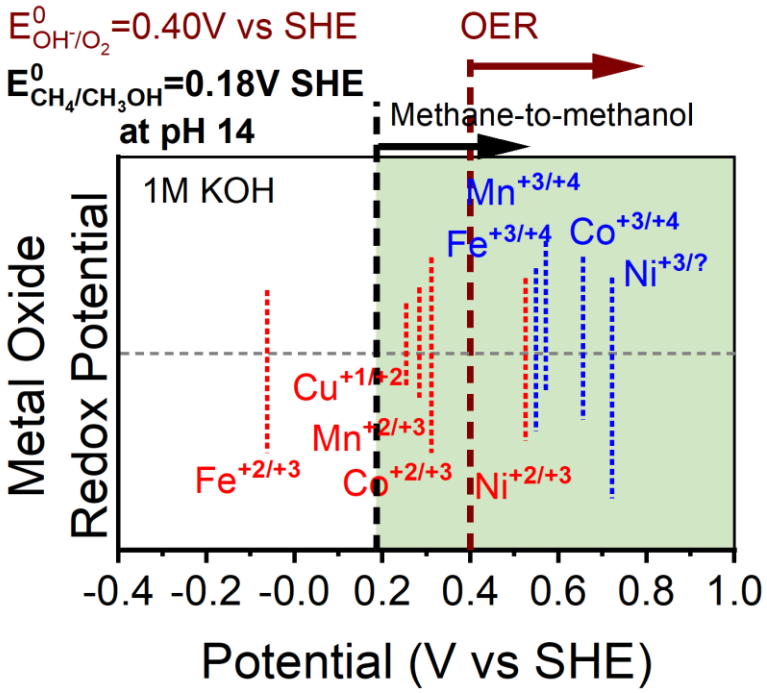

Figure 2.25: Redox potentials experimentally measured for oxidatively electrodeposited transition metal (oxy)hydroxide in 1 M KOH.

From a purely experimental perspective, the potential window between 0.5 and 1.0 V vs SHE is thus optimal to enable any of the transition metal (oxy)hydroxides to be conductive while accessing a large population of metal-oxo sites on the surface of the catalysts to activate and oxidize methane. It must be noted, however, that the redox potentials in Figure 2.25 and the rates of water oxidation are a function of pH and will change in a different manner for each metal (oxy)hydroxide relative to the 0 V vs SHE.[112] That is, the onset of conductivity and the population of high oxidation states on the surface of the catalyst during operation is a complex function of the potential and the local pH. Based on previous theoretical works for the activation of methane,[113, 114] and on the DFT results on CoOOH presented here, we hypothesize that indeed various transition metal oxides are active for the transformation of methane to methanol at ambient and moderate temperatures provided four conditions are met: 1) enough methane is supplied to the catalyst surface, 2) the transition metal oxide is conductive without the need of large overpotentials where OER could become dominant, 3) the potential is low enough so that methanol can be preferentially desorbed versus the formation of methoxy and further oxidation,

and 4) the catalyst architecture and the transport properties of the cell allow methanol to be transported away from the electrode before it can be further oxidized. Indeed, our DFT calculations on CoOOH show for a potential below ~1 V, desorption of methanol coupled with adsorption of OH^- on the Co site is thermodynamically favored versus further oxidation to methoxy, so that electrocatalytic oxidation with the control of the potential could open a possibility of selective formation of methanol. Moving to gas phase humidified membrane electrode assemblies could be a viable approach to electrochemical methane-to-methanol transformation systems provided the four conditions above of high methane transport, high metal oxide catalyst conductivity, fast methanol desorption relative to overoxidation, and fast methanol product collection are met.[115-117]

We have shown here that partial oxidation of methane proceeds via the chemical reaction between methane and high oxidation states of the catalyst, even without an applied potential beyond the one needed to maintain the oxidation state of the site. Faradaic efficiency may then no longer be a good descriptor for selectivity in the partial oxidation of methane to methanol. We consider the following steps for the partial oxidation of methane on metal-oxo sites. At intermediate overpotentials (0.5 - 1 V vs SHE), the methane is activated electrochemically by dissociation of a C-H bond via reaction with a hydroxyl anion and concerted rebinding with a hydroxyl located on the surface of the electrode to form adsorbed methanol (Equation 2.2). Methanol can desorb from the site, and this reaction is made exothermic by a concerted electrochemical adsorption of OH^-. At larger overpotentials (1 - 1.3 V), the hydroxyl group attached to the methanol on the surface becomes acidic leading to the formation of methoxy which subsequently over-oxidizes to CO_2 which is captured as carbonate in the alkaline electrolyte. At even higher overpotentials (>1.3 V), the oxygen evolution process becomes a competitive reaction as well.

According to thermodynamics of the reactions, methane overoxidation to CO_2 by methoxy formation would be preferable over OER. A significantly greater methane concentration might

result in a drop in OER and an increase in over-oxidation since both processes utilize the same active site. However, at moderate methane concentration not all active sites would be occupied/deactivated by methoxy, hence we would observe significant OER on the CoOOH surface at large overpotentials.

2.6 Conclusions

In summary, we have demonstrated the use of electrochemical methods for the deposition of a family of thin-film transition metal (oxy)hydroxides, which is a simple, clean, and efficient strategy for the fabrication of electrodes for the partial oxidation of methane to methanol in a carbonate electrolyte. CoO_x, NiO_x, MnO_x and CuO_x are active for the partial oxidation of methane to methanol while FeO_x oxidized methane entirely to CO_2 in the potentials tested. Taking CoO_x as a prototypical methane partial oxidation electrocatalyst, the dependence of activity and methanol selectivity on catalyst loading (porosity), applied potential, temperature, and cell hydrodynamics were systematically investigated. Higher catalyst loading with thicker films lead to more significant over-oxidation of methanol due to the highly porous structures and thus the longer paths for methanol to exit the catalyst layer. Acetate is a side-product at low overpotentials (0.8V vs SHE) while methanol is the favored product at medium overpotentials (0.86~1.06V vs SHE). This very interesting potential regime where selective oxidation of methane to methanol is seen is confirmed and explained by our DFT simulations. We find an optimum potential window in which methane activation forming methanol and methanol desorption are both thermodynamically favorable on fully hydroxylated CoOOH. Methanol desorption from the site is favored due to the stabilizing concerted electrochemical adsorption of a OH^- from the solution. The selectivity is hence explained by competitive adsorption with hydroxide anion, which expels the methanol from the site, and by the transport of methanol away from the electrode. High overpotentials (above 1.16 V vs SHE) result in the over-oxidation of the produced methanol to CO2, since electrooxidation of methanol to methoxy becomes more favorable than its desorption,

and the production of oxygen through OER. Similar mechanisms for the production of methanol could be at play on other unary transition metal (oxy)hydroxides and need to be systematically studied through a combination of experiments under well-defined transport conditions and DFT simulations.

The temperature also plays an essential role in both methane activation and over-oxidation of the produced methanol. High temperatures result in lower selectivity for methanol likely to the increase in the rates of thermal steps for both methane activation and methanol overoxidation, as well as the increase in the OER activity and the decrease in solubility of methane in the electrolyte. Higher rotation speeds of the cylinder electrode increase turbulence in the cell and decrease the cycling time of the accumulation and overoxidation of methanol in the electrochemical cell. More importantly, catalyst loading (porosity) and electrolyte convection are both correlated with the effect of mass transfer, implying the importance of understanding mass transport of the relevant species in partial oxidation studies of methane.

Through the use of the gas-tight rotating cylinder electrode cell, unique conditions of hydrodynamics for the partial oxidation of methane show the importance of the control on both kinetics and mass transfer of each step during the reaction. Consequently, this work demonstrates electrodeposition as a viable strategy for catalyst fabrication and may pave the way for efficient strategies of catalyst preparation for further studies of the electrochemical partial oxidation of methane under ambient conditions as well as well-defined conditions of mass, heat, and charge transport.

The transition metal (oxy)hydroxide catalysts reported here should enable the decentralized production of methane to methanol utilizing electrochemical units engineered for optimal methane delivery to the electrode surface as well as rapid methanol product removal and collection. Modular electrochemical devices with advanced electrode architectures for methane and methanol transport can one day enable the efficient and decentralized partial oxidation of

methane to methanol at ambient temperatures. In this work we have provided a first understanding of how to tackle the design of these devices.

Chapter 3: CO_2 capture and conversion

3.1 Introduction

Carbon capture and utilization (CCU) is a crucial technology for mitigating the effects of climate change, as carbon dioxide (CO_2) is the main greenhouse species emitted across all sectors of our economy. Point sources of CO_2 such as power plants and industrial chemical manufacturing plants emit CO_2 at concentrations of up to 15 vol% CO_2 and are being targeted as the first locations for CCU implementation. CO_2 removal at industrial scales relies on the use of aqueous solutions of amines that capture CO_2 exothermically in an absorber unit. Thermal energy is then used to heat and release CO_2 from the loaded amine solution generating a pure CO_2 gas stream for further conversion, and a lean amine solution for further CO_2 uptake. The direct transformation of CO_2 in its captured form while bonded to the absorbing media or molecule, known as reactive carbon capture (RCC), promises to enable the high rate transformation of captured CO_2 while circumventing its release.[118-121] In the last few years, a great deal of attention has been given to the development of RCC systems that use renewable electrons to drive the thermodynamically uphill process of directly upgrading the captured CO_2 on the surface of a catalyst electrode. Electrocatalysts can potentially transform the captured CO_2 under similar conditions of low temperature and high pressure as those used in the absorber unit, thus promising the reduction in capital and operating costs for CCU.[118, 122] Aqueous carbon capture solutions, however, present a large degree of speciation where the captured carbon exists in different molecular configurations with intrinsically different energy states and consequently different kinetic barriers to access these carbon atoms for reaction.

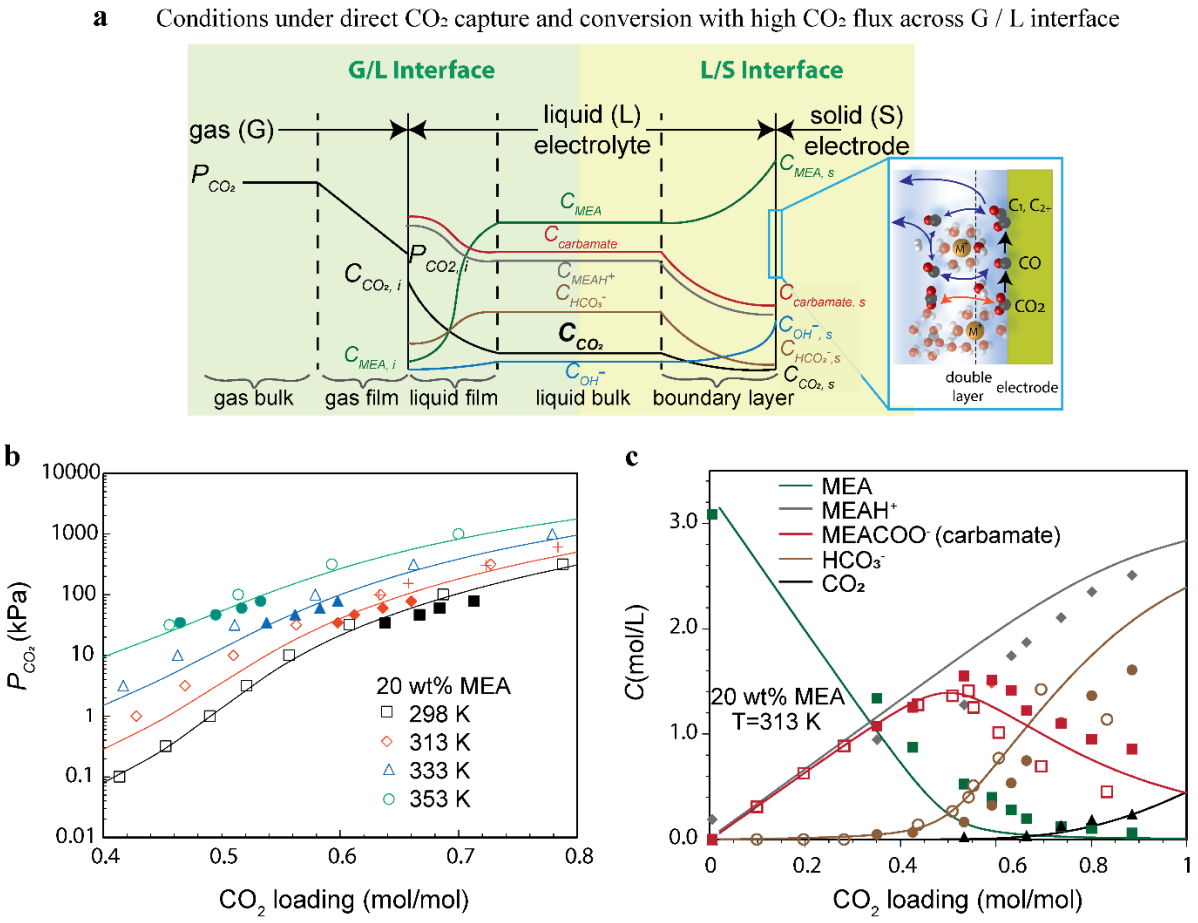

Figure 3.1: (a) Schematic of G/L and L/S interfaces relevant to CO_2 capture and conversion showing the spatial speciation of CO_2-MEA solutions. (b) Comparison of experimental data[123-125] (symbols) for CO_2 partial pressure of MEA-H_2O-CO_2 system and modified Kent-Eisenberg VLE model prediction (lines) for a 20 wt% MEA aqueous solutions. This plot is used in this work to estimate the loading of CO_2 in MEA solutions by measuring the partial pressure of CO_2 in equilibrium with the solution. (c) Equilibrium speciation in MEA aqueous solution[125, 126] as a function of CO_2 loading.

In order to illustrate the complexity of RCC systems, Figure 3.1a shows the speciation of CO_2 in a monoethanolamine (MEA) aqueous solution as a function of position starting from the gas/liquid (G/L) interface and ending at the liquid/solid (L/S) interface where carbon species are transformed into a fuel or chemical on a heterogeneous catalyst electrode. The concentration of species varies significantly in space and time across the RCC system. CO_2 in MEA aqueous solution exists in the form of carbamate ($RNHCOO^-$), bicarbonate (HCO_3^-) and unbound dissolved CO_2.[123-128] Here R represents the $-CH_2CH_2OH, -H, or -CH_3$ functional groups in the broadly

used monoethanolamine, amine and methylamine absorbers. Under equilibrium, the loading of CO_2 in solution (mol of CO_2/mol of amine) is proportional to the partial pressure of CO_2 in the gas phase (P_{CO_2}) and increases or decreases when the amine solution is respectively cooled or heated as shown in Figure 3.1b. The simple process of moving the loaded amine solution across an RCC plant from the absorber unit to the reaction/regeneration unit using pumps or through expanding valves will result in heating and depressurization and thus large CO_2 loading changes. Higher CO_2 loadings in amine solutions during absorption are achieved by direct reaction of CO_2 with hydroxyl anions in highly alkaline solutions to make bicarbonate and carbonate. Bicarbonate is a more thermodynamically stable form of the captured CO_2 molecule compared to the MEA carbamate and becomes the dominating form of absorbed carbon at high CO_2 loadings (Figure 3.1c), contributing to the increased loading of carbon in capture solutions. Lower pH values and higher temperatures accelerate the desorption and release of CO_2[129-131] and need to be taken also into account in RCC research. The major scientific challenge in electrocatalytic RCC is the rigorous distinction of the reacting species at the electrode interface between dissolved CO_2, bicarbonate, or the absorber-CO_2 adduct (e.g. carbamate in amine-based absorbers). A detailed understanding of the nature of the reacting molecule is necessary for the rational co-design of catalysts and absorbers and the accelerated scale-up of RCC technologies.

The direct electrolysis of the MEA-CO_2 adduct in a 30 wt% MEA / 2 M KCl solution on a silver electrode has been recently reported to be a promising method for the reactive capture of CO_2. This approach demonstrated operating current densities greater than 50 mA cm^{-2} and Faradaic efficiencies for CO of up to 72% at 60 ^{o}C.[132] The enhancement in Faradaic efficiency for the CO_2 reduction product compared to the same system at lower temperatures and in the absence of the KCl salt was attributed to the tailoring of the electrochemical double layer through the use of alkali cations. Control experiments suggested that dissolved CO_2 was removed from the system by purging N_2 before the start of the experiment, however, more systematic studies measuring the amount of dissolved CO_2 in the system under operation are necessary as the broad CO_2 capture

literature[124-126, 133, 134] indicates that the concentration of dissolved CO_2 should be very high in any MEA capture solution loaded with CO_2 and heated up to 60 ^oC (Figure 3.1b). In this work, we combine first principle modeling and experimental electrochemical characterization to take a fundamental approach in the analysis of various CO_2 capture solutions reported in the literature for the electrochemical reduction of CO_2 to carbon monoxide on an electrodeposited silver catalyst.

When the transport properties are well-defined everywhere in the gas, liquid, and solid phases of an electrochemical cell, it will be evidently shown that the reduction of CO_2 absorbing solutions on a silver electrode is primarily driven by the transformation of unbound dissolved CO_2. Utilizing a gastight rotating cylinder electrode (RCE) cell with well-defined transport properties at the gas/liquid and liquid/solid interfaces, we have carried out the electrochemical reduction of ammonium carbamate (AC), potassium bicarbonate and a CO_2-loaded MEA solutions and observed that dissolved CO_2 is always present in the liquid as revealed by the partial pressure of CO_2 in the headspace of the cell at the same time as the CO product. Importantly, in all experiments, the maximum concentration of CO reached in the headspace of the cell is proportional to the partial pressure of CO_2. By changing the rotation speed of the electrode in the RCE cell, the mass film transfer coefficient for the transport of species to and from the electrode is systematically changed, and we show that the maximum partial current density of CO is limited by the transport of CO_2 dissolved in the bulk of the solution to the surface of the electrode. Our combined theory-experiment approach demonstrates that reduction of dissolved CO_2 is favored over carbamate reduction, until highly negative potentials where the direct reduction of amine carbon capture solutions becomes feasible, while bicarbonate cannot be directly reduced on the surface of the silver electrode even at high overpotentials.

3.2 Methods

3.2.1 First principle calculations

DFT calculations were performed with the Vienna ab initio simulation package using the general gradient approximation (GGA) Perdew−Burke−Ernzerhof (PBE) functional,[87] with the van der Waals interaction between atoms corrected using D3.[135] The projector-augmented wave method was employed to describe the core electrons, while the valence electrons were expanded in a plane-wave basis set with a cut-off energy of 400 eV.[86] A (3×3)-4 layers surface supercell was considered for Ag (111), and the Brillouin zone was sampled using a Gamma-centered (4×4×1) k-point mesh (for benchmark, see Figure 3.2).

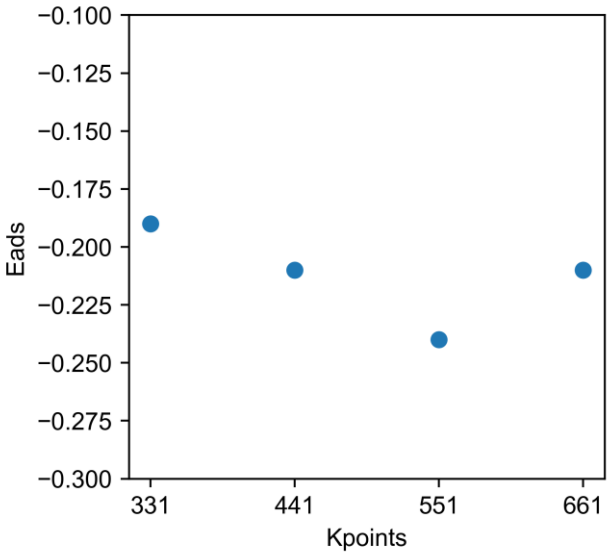

Figure 3.2: Convergence of adsorption energy of carbamate-K with respect to k-point mesh at -1.5 V vs SHE. Considering both accuracy and computational cost, (441) k-point mesh was chosen in this work.

Since the capture agent used in this work is the simple NH_3 molecule, the sizes of adsorbates are relatively small along the reaction path, and the distance between periodic NH_2COOH, the largest adsorbate along the reaction path, is 8.7 Å, which is not expected to result in significant interactions. Increasing the unit cell size, such as (4x4), will exponentially increase the difficulty in sampling configurations of adsorbates with cations. We performed a test to compare the

adsorption of NH_2COOH using (3x3) and (4x4) unit cells and found that the difference in adsorption energy is only 0.04 eV. Thus, in this work, we consider (3x3) unit cells. When using larger molecules as capture agents, it is important to consider the possible interactions between adsorbates and select the appropriate unit size. The bottom two layers were fixed while the upper two layers with adsorbates were allowed to relax during the optimization. The convergence criteria for electronic and force minimization were set to 10^{-6} eV and 0.02 eV/Å respectively. An explicit K^+ was included along with the optimization to include the cation effect. We tested the reliability of the approach that explicitly considers the cation while employing implicit solvent model to describe the solvation of the cation near the surface in our previous work.[136] The zero point energy and entropy corrections were determined from frequency calculations performed for all the structures using the harmonic oscillator approximation.

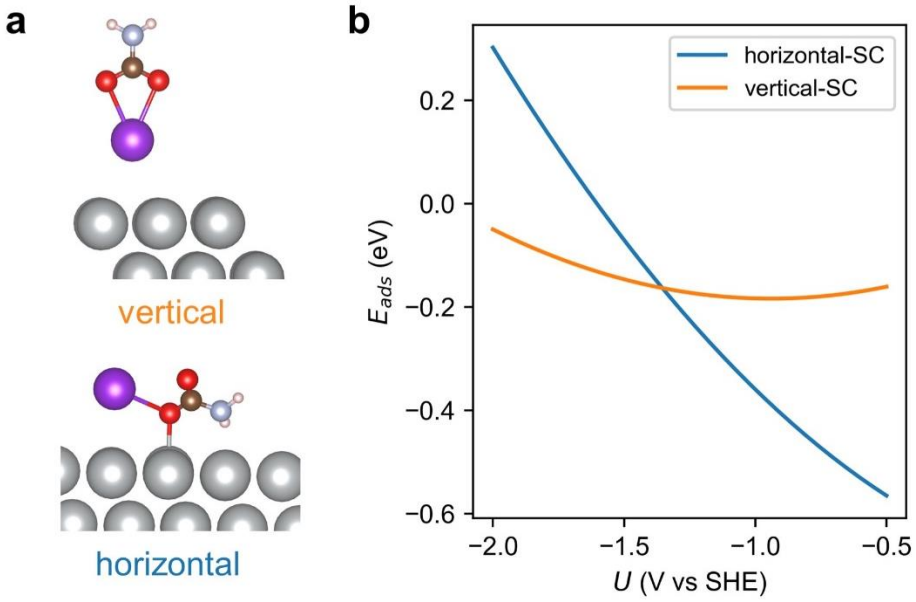

Figure 3.3: (a) Two configurations of carbamate in the region of double layer at -1.3 V vs SHE. (b) Adsorption energy of carbamate as the function of electrode potential.

In our study, we sampled and evaluated different configurations of adsorbates on the electrode surface and reported the most stable ones in the paper. For carbamate, we found two potential-dependent configurations, which are shown in Figure 3.3. We considered the liquid-

vapor equilibrium for CO_2 and NH_3 in our calculations to determine the chemical potentials of these species. The experimentally measured partial pressure for CO_2 is 0.3-0.4 kPa and based on the equilibrium for a mixed salt solution,[137] the pressure for NH_3 is estimated as 0.1-1.0 kPa. The choice of pressure in these intervals only has a minor impact (~0.1 V) in the crossing point in potential between the two competing potential-determining steps in Figure 3.21, namely CO_2 adsorption and *NH_2COOH to *COOH. For calculations shown in Figures 3.15 and 3.21, we used 0.4 kPa for CO_2 and 1.0 kPa for NH_3, and cases for a lower pressure are shown in Figure 3.13 and Figure 3.14.

The chemical potential of H, $\mu(\mathrm{H})$, was calculated by

$$\mu(\mathrm{H}) = \frac{1}{2}E(H_2) - ln(10)k_BT \cdot pH - eU_{SHE} + (ZPE^{gas} + C_p^{gas} - TS^{gas}) - (ZPE^{ads} + C_p^{ads} - TS^{ads})$$

where the potential is expressed in SHE scale.

Potential-dependent energetics were obtained using GCDFT calculations,[99] which explicitly included the charge polarization resulting from the applied potential, combined with an implicit model of the water solvent and the electrolyte. The potential-dependent grand canonical free energy can be expressed by a surface charging model:

$$\Omega(U) = \Omega(U) - q(U) \cdot FU = \Omega(U_0) - \frac{1}{2}C(U - U_0)^2$$

where $\Omega(U)$ is the electronic energy of the surface at the *U* potential, $q(U)$ is the charge difference against the neutral condition, F is the Faradaic constant. *C* stands for the effective capacitance and U_0 represents the potential of zero charge (pzc). For more details of GCDFT, see our previous work.[138-141]

The linearized Poisson Boltzmann implicit solvation model implemented in VASPsol[99] is used to represent the polarizable electrolyte region. The dielectric constant 73.4, and the Debye screening length 2.09 Å, were used (corresponds to 2 M aqueous solutions of MEA with 2 M KCl from work by Sargent et al[132]). The surface slab is symmetrized along the z axis to avoid overall

dipole and asymmetric potential in the implicit solvation region. Here the implicit solvent thickness is set to 60 Å for the symmetrized slab. All intermediate species were computed using the VASPsol, which takes into account solvent effects for each intermediate.

3.2.2 Catalyst preparation

Ag cylinder electrodes were prepared via a modified electrodeposition method.[142] In brief, deionized water (18.2 MΩ cm) was used to prepare the electrodeposition bath with 0.1 M silver nitrate ($AgNO_3$, puriss. p.a., >99.8%, Sigma Aldrich), 0.15 M nitric acid (HNO_3, TraceMetal Grade, Fisher Chemical) and 0.01 M citric acid (anhydrous, ACS, 99.5+%, Alfa Aesar). The electrodeposition procedure was carried out under atmospheric conditions inside a fume hood. An Autolab PGSTAT302N potentiostat/galvanostat was used for the electrodeposition of Ag in a two-electrode setup with a titanium cylinder substrate (active geometric area = 3 cm^2) as the working electrode, and a Pt electrode (Pine Research) as the counter electrode. Before the electrodeposition, the surface of the titanium cylinder substrate was polished using sandpaper (P600, 3M), rinsed thoroughly, sonicated in deionized water for 10 minutes and finally dried under Ar flow. The electrodeposition of Ag was carried at a fixed current of -30 mA which was applied for 12 seconds and then the current was reduced to -6 mA and kept constant for 10 minutes to deposit a compact and nanoporous Ag film onto the titanium cylinder substrate.

3.2.3 Electrochemical cell configuration

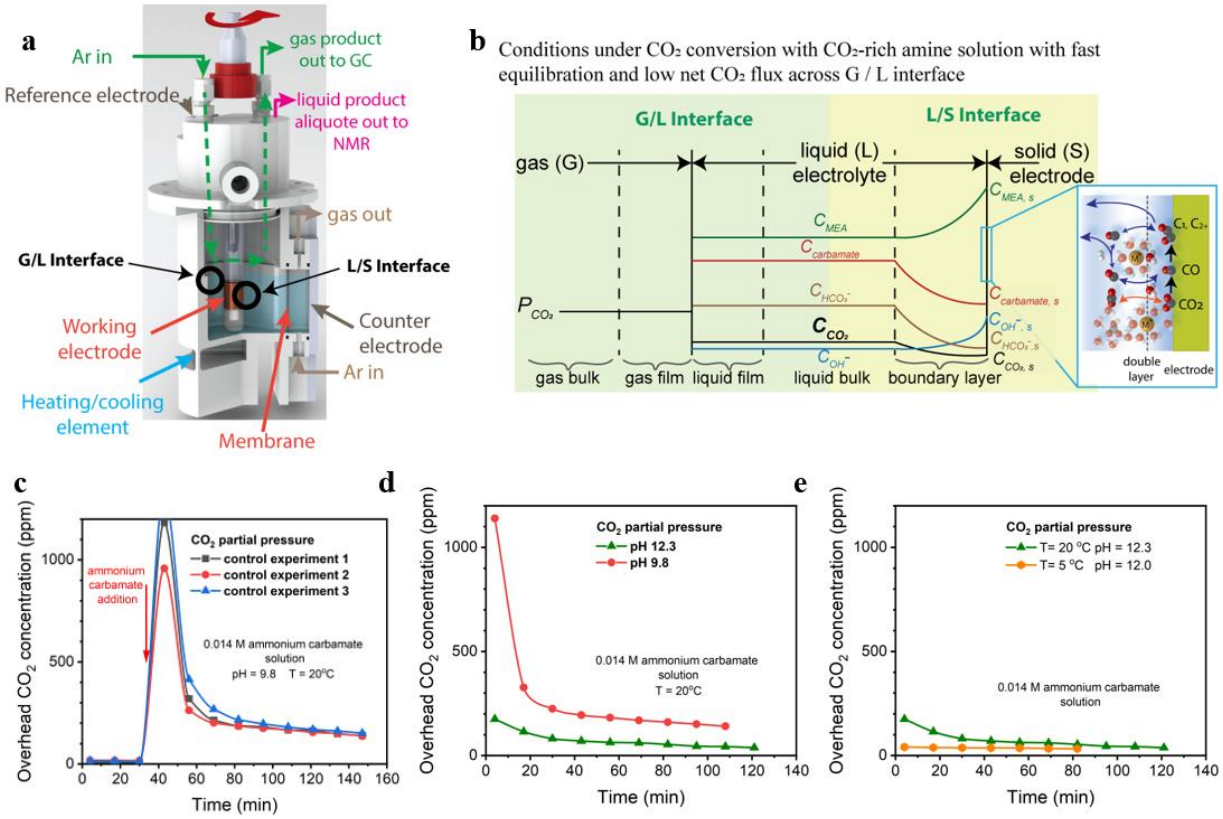

Figure 3.4: (a) Gastight rotating cylinder electrode. (b) Schematic of G/L and L/S interfaces relevant to CO_2 electrochemical reduction in CO_2-rich amine solutions. (c) Concentration of CO_2 under transient conditions upon the addition of ammonium carbamate to a 0.099 M $KClO_4$ and 0.001 M KOH solution. (d) Concentration of CO_2 under transient conditions for a 0.014M ammonium carbamate solution as a function of pH. (e) Concentration of CO_2 under transient conditions for a 0.014M ammonium carbamate solution as a function of temperature.

A gas-tight rotating cylinder electrode (RCE) cell reported by us[76] was used for all the amine-captured CO_2 reduction experiments in this work. In the RCE cell, a follower magnet inside the cap traces a driver magnet outside the cell connected to the shaft of the MSR Rotator (Pine Research) via magnetic coupling realizing rigorous control of the mass transport in the cell (Figure 3.4a). The cap for the working electrode compartment is in charge of the electrical connection while having a relatively small headspace (~50mL). There are three threaded ports on the cap to accommodate plastic leak-free gas pipes and fittings (Swagelok). One of the three ports is used to bubble Ar gas directly into the electrolyte. A second port serves as the gas outlet transferring

gaseous products to an on-line gas chromatogram (GC, 8610C, SRI Instruments) for the detection and quantification of gaseous products during the experiment. The remaining port is used to inject reactants or to draw out liquid samples for further quantification of liquid products through Nuclear Magnetic Resonance (NMR) while keeping the whole system gas-tight. In all experiments, Ar is also bubbled in the counter electrode compartment. Hex screws and nuts are used to compress and seal the electrochemical cell. Temperature control is realized via a cooling block with a heat-exchange area of 16 cm^2 positioned at the bottom of the RCE working electrode compartment. The electrolyte is collected after each experiment for analysis.

3.2.4 Electrochemical characterization

Table 3.1: Compositions of the catholyte in the working chamber of the RCE cell

Experiment label	$KClO_4$	KOH	AC	MEA	HCO_3^-
0.2M AC	0.099M	0.001M	0.2M		
0.7M AC	0.099M	0.001M	0.7M		
0.2M MEA	0.099M	0.001M		0.2M	
0.7M MEA	0.099M	0.001M		0.7M	
0.2M HCO_3^-					0.2M
0.7M HCO_3^-					0.7M

Table 3.2: Compositions of the anolyte in the counter chamber of the RCE cell

Experiment label	$KClO_4$	KOH	AC	MEA	HCO_3^-
0.2M AC	0.099M	0.001M			
0.7M AC	0.099M	0.001M			
0.2M MEA	0.099M	0.001M			
0.7M MEA	0.099M	0.001M			
0.2M HCO_3^-					0.2M
0.7M HCO_3^-					0.7M

Prior to setting up the cell, the Ag electrodeposited titanium cylinder electrode is prepared and rinsed thoroughly with deionized water. A three-electrode gas-tight rotation cell setup was

used with the cylinder as the working electrode, a platinum foil (Pt, 0.1 mm thick, 99.99% metal basis, Alfa Aesar) as the counter electrode, the Ag/AgCl/1 M KCl as the reference electrode (CH Instruments, Inc.). The different compositions and concentrations of catholyte and anolyte tested in this work are compiled in Table 3.1 and Table 3.2. The CO_2-saturated MEA solutions were prepared by bubbling CO_2 in a separate glass cell (Pine Research) containing around 100 mL of the amine solution. The solution was continuously stirred at 300 rpm and gas was delivered through a mounted frit (Pine Research). CO_2 was purged into the amine solution for 3 hours to ensure the saturation of the solution with CO_2. All solutions were purged with Ar for 6 hours to remove as much of the dissolved CO_2 as possible before these solutions were transferred into the electrochemical cell for RCC tests. After loading the solution with CO_2 for 3 hours and flowing Ar for 6 hours to remove some of the dissolved CO_2, the partial pressure of CO_2 in equilibrium with the CO_2-loaded MEA is between 0.1 and 0.5 kPa. These equilibrium pressures correspond to a CO_2 loading of around 0.5 mol/mol of amine.[125, 126] At these loading, the predominant carbon species are carbamate while bicarbonate is low.[134] 82 mL and 6 mL of the as prepared catholyte and anolyte solutions were added into the working and the counter compartments, respectively. After the assembly of the cell, the circulating bath was connected with the cooling block to control and equilibrate the operating temperature inside the working electrode compartment. Before electrochemical measurements, high purity argon (Ar, Airgas 99.999%) as the inert gas was flowed at a rate of 20 sccm for at least 60 minutes in both the working and counter electrode compartments to make sure that the compositions of gases in the headspace of the working electrode compartment are stable before any further electrochemical tests. All the gas flow rates were maintained throughout the electrochemical measurements.

In the electrochemical measurements, electrochemical impedance spectroscopy (EIS) was collected under each current density lasting 5 seconds before the chronopotentiometry and the uncompensated resistance was determined from the real part of the resistance measured at high frequency (f > 100 kHz). The potential drop including the resistance of the solution from the

reference electrode to the cylinder electrode was accordingly corrected in further results and discussion. The electrochemical amine-captured CO_2 reduction was conducted in the RCE cell using chronopotentiometry. The overall duration of chronopotentiometry was 360 minutes. Detailed description of the potentials and currents used for the generation of the data in Figure 3.16 and Figure 3.24 are given in Experimental procedures.

3.2.5 Physical characterization

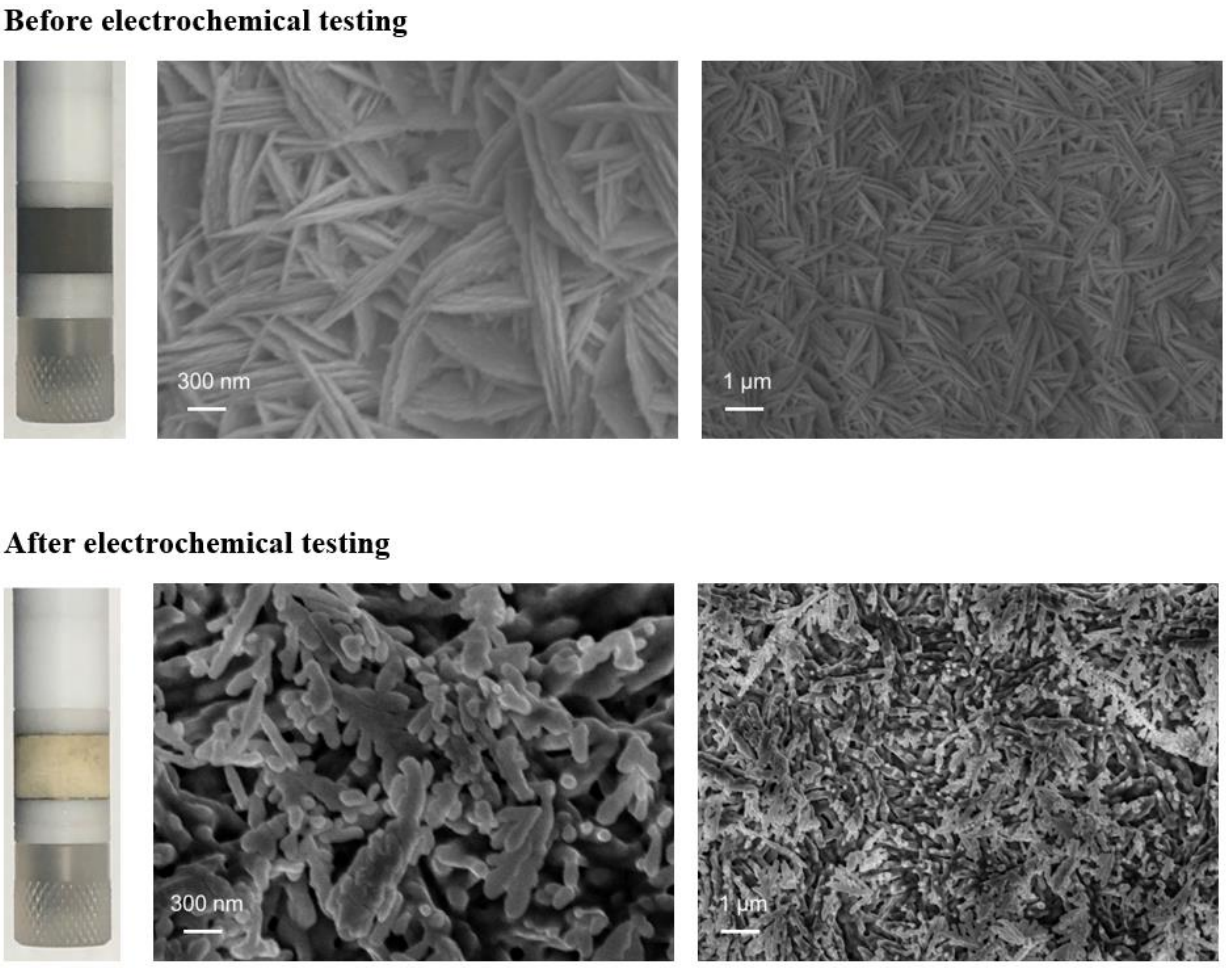

Figure 3.5: Physical characterization by optical and scanning electron microscopy of the electrodeposited Ag catalyst films before and after testing. The change in morphology occurs within the first 10 minutes of testing and thus the morphology in the images at the bottom is the one representative of the active catalyst.

Scanning electron microscopy (ZEISS Supra 40VP SEM) was used to get the morphology and microstructures of the as prepared electrocatalysts. The morphology of the catalyst changes within a few minutes of testing and acquires softer dendrite edges as shown in Figure 3.5.

3.2.6 Product detection and quantification

A gas chromatograph (GC) (8610C, SRI Instruments) was used for the detection and quantification of gas products. In a typical experiment, injections were made at a 20-minute interval. Each CG run consisted of 14 minutes of elution time and 6 minutes of cool-down. The TCD and FID signals were integrated and compared against a calibration curve to calculate the Faradaic Efficiency (FE) for products including H_2 and CO. The detection limits for the CO and H_2 gases are in the order of 1 ppm and 100 ppm, which are equivalent to 0.001 mA/cm^2 and 0.1 mA/cm^2 respectively in terms of current density under our testing conditions.

Nuclear magnetic resonance spectroscopy (1D ^{1}H NMR 500 MHz with cryoprobe, Bruker) was used for the detection and quantification of liquid products. The internal standard was prepared with 52.5 mM of phenol (≥99.5%, Sigma-Aldrich) and 2.1 mM of dimethyl sulfoxide (DMSO, ≥99.9%, Sigma-Aldrich) in deuterium oxide (D_2O, 99.9%, EMD Millipore). Details on the construction of calibration curves and procedure for product quantification are given in our previous report.[76]

3.2.7 Gas/Liquid interface characterization

CO_2 absorption is a reversible process characterized by an equilibrium constant. The equilibrium between hydroxyl ions and dissolved CO_2 is given by Equation 3.1 for alkaline solutions. The absorption of CO_2 in alkaline amine solutions leads to the additional formation of the corresponding carbamate and ammonium ions (Equation 3.2 and Equation 3.3). The experimental challenge in RCC systems is measuring the concentration of dissolved $CO_2(aq)$ in equilibrium with the partial pressure of CO_2(g) in the electrochemical cell, which in this work is measured using a gas chromatogram directly connected to the headspace of the cell.

$$CO_2(aq) + OH^- \rightleftharpoons HCO_3^- \quad (3.1)$$

$$CO_2(aq) + 2RNH_2 \rightleftharpoons RNHCOO^- + RNH_3^+ \quad (3.2)$$

$$RNH_2 + H^+ \rightleftharpoons RNH_3^+ \quad (3.3)$$

When a fast equilibrium is reached at the gas/liquid interface (Equation 3.4), the partial pressure of CO_2 can be used to estimate the concentration of CO_2 dissolved in the solution using Henry's Law where $P_{CO_2}^{gas} = H_{CO_2} C_{CO_2}^{liq}$ and $H_{CO_2} = 29.41\ bar\ M^{-1}$ at 298.15 K.

$$CO_2(g) \rightleftharpoons CO_2(aq) \quad (3.4)$$

Experimentally, one of our first focus points in this work was to determine whether the partial pressure of CO_2 in our cell was indeed in equilibrium with CO_2 dissolved in the solution. In our RCE cell (Figure 3.4a), Argon gas was purged at a rate of 20 sccm in various CO_2-amine electrolytes and the outlet of the cell was fed to an on-line gas chromatogram to measure the CO_2 concentration in the overhead space of the cell as a function of time. From the CO_2 concentration in the headspace and the knowledge that the pressure is 1 bar in the overhead, the partial pressures of CO_2 were calculated. This partial pressure of CO_2 should be proportional to the concentration of dissolved CO_2 in solution if the gas/liquid interface in the cell has reached equilibrium in the timescales for sampling of the gas headspace (Figure 3.4b). Figure 3.4c shows the concentration of CO_2 in the gas phase in the cell as a function of time before and after the addition of ammonium carbamate to a 0.099 M $KClO_4$ and 0.001 M KOH electrolyte solution at an initial pH of 11.1 where enough ammonium carbamate is added so that the concentration of ammonium carbamate upon addition is 0.014 M. Before the addition of the ammonium carbamate, it is evident that there is no CO_2 but upon the addition of the ammonium carbamate at the 30-minute mark, the concentration of CO_2 rapidly increases and the pH drops to around 9.8. As time proceeds, the flux of CO_2 out of the liquid decreases and the concentration of CO_2 decreases slowly approaching a concentration of 200 ppm after 80 minutes of the addition of the ammonium carbamate. This concentration value in the headspace is lower if the initial pH of the electrolyte is higher and the pH of the solution after the addition of the ammonium carbamate is higher as

shown in Figure 3.4d where the pH of the solution is 12.3 and the concentration of CO_2 in the headspace after 80 minutes of the carbamate addition is 50 ppm. On the other hand, lower pH values result in higher CO_2 concentrations in the overhead. Temperature effects are shown in Figure 3.4e. At lower temperatures, the concentration of CO_2 in the headspace is lower. These results are in agreement with the expectation that higher proton concentrations (lower pH) and higher temperatures should accelerate the release of CO_2 from amine solutions.

3.2.8 Liquid/Solid interface characterization

Here we used dimensional analysis to investigate the mass transport properties in the liquid/solid interface of the RCE cell by determining the Sherwood number under different hydrodynamics. According to the Buckingham Pi theorem, the Sherwood number describing the ratio of the convective mass transfer to the rate of diffusive mass transport depends on two independent dimensionless numbers: the Reynolds number Re and the Schmidt number Sc in the form of Equation 3.5

$$Sh = KRe^{a}Sc^{b} \tag{3.5}$$

in which, the Schmidt number is defined to be the ratio between the kinematic viscosity ν of a fluid and the diffusion coefficient D of the specific species in Equation 3.6

$$Sc = \frac{\nu}{D} = \frac{\mu}{\rho D} \tag{3.6}$$

and the Reynolds number is defined in Equation 3.7.

$$Re_{\mathrm{RCE}} = U_{\mathrm{cyl}} d_{\mathrm{cyl}} \frac{\rho}{\mu} \tag{3.7}$$

Here, ρ is the solution density, μ is the dynamic viscosity, d_{cyl} is the outer diameter of the cylinder, and U_{cyl} is the peripheral velocity of the rotating cylinder.

U_{cyl} can also be expressed according to the rotating cylinder electrode we used as a function of the angular rotation rate ω in rad/s, or the frequency f in revolutions per minute (rpm) as in Equation 3.8.

$$U_{\mathrm{cyl}} = \omega \frac{d_{\mathrm{cyl}}}{2} = \frac{\pi d_{\mathrm{cyl}} f}{60} \tag{3.8}$$

In our previous work, we have characterized the mass transfer properties of the cell through electrochemical reduction of ferricyanide, protons, and nitrite under different concentrations of reactants, rotational speeds, and different temperatures. After extracting the limiting current densities j_{lim} at mass transport-limited potential regime, the mass transfer coefficient k_m can be calculated by

$$j_{\mathrm{lim}} = zFC_{i,b}k_m \tag{3.9}$$

and further converted into the corresponding Sherwood number. The prefactor and the exponential coefficient are determined by linear regression on the plot of log $Sh/Sc^{0.33}$ vs. log Re (Figure 3.6a). Finally, the expression of Sherwood number as a function of the Schmidt number and Reynolds number for our RCE cell can be written as:

$$Sh_{\mathrm{RCE}} = \frac{k_m}{D/d_{\mathrm{cyl}}} = 0.204{Re_{\mathrm{RCE}}}^{0.59}Sc^{0.33} \tag{3.10}$$

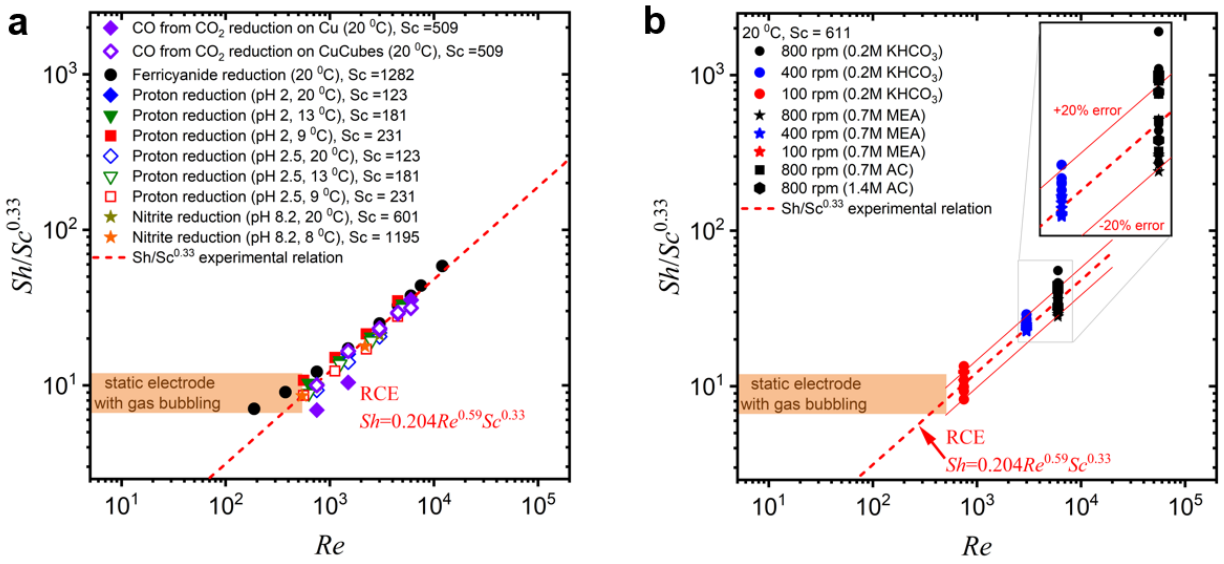

Figure 3.6: Sherwood number correlation to Reynolds and Schmidt numbers. (a) Empirical determination of the correlation via dimensional analysis of various reactions under different conditions reported in the previous reports.[76, 84] Including, experimental values calculated from the production of CO from CO_2R for flat and porous copper electrodes. (b) Sherwood and Reynolds correlation for data in Figure 3.16 for 0.2 M $KHCO_3$ and 0.7 M MEA at 20°C under different rotation speeds on a silver electrode.

The developed relationship (see Jang et al.[76] for the complete development of the relationship) universally holds true regardless of the experimental conditions including the effects of reactants, their concentration, electrode rotation, and temperature. Therefore, the equation can be used as a reference for the convective transport-limited rates of reactions that cannot be readily obtained from experiments due to the complexity of systems including multiple electrocatalytic and buffering reactions. For example, j_{lim} of CO_2 in this work cannot be measured explicitly with the dominating hydrogen evolution and is complicated to estimate with equilibrium reactions between CO_2 and absorber adducts. However, the maximum flux of CO_2 that can be supplied to the surface of the electrode can be determined from Equation 3.10 with the assumption that the local concentration of CO_2 at the electrode is zero. This calculated maximum flux of CO_2 or its corresponding maximum partial current density to CO is sufficient to explain the relationship between the observed partial pressure of CO_2 and CO partial current density to a large extent considering the low concentration of dissolved CO_2 in this system. This is shown in Figure 3.6b where the data in Figure 3.16 is replotted in dimensionless terms.

Partial current densities for CO of up to 25 mA cm^{-2} can be achieved at a rotation of 800 rpm for a catalyst selective for the reduction of CO_2 to CO under 1 bar of CO_2. At 100 rpm, this maximum partial current density is 7.4 mA cm^{-2}. Here we ignore the fact that dissolved CO_2 can react directly with hydroxyls (Equation 3.1) generated at the cathode electrode during electrochemical reduction reactions in aqueous electrolytes. These chemical reactions would result in lower maximum current densities than those in the absence of reaction. However, inside the boundary layer, as dissolved CO_2 is depleted, it is also likely that bicarbonate and carbamate will decompose (reverse direction in Equations 3.1 to 3.3) to generate additional CO_2 compensating for the CO_2 consumed at the surface of the electrode. Local heating generated by ohmic resistance and the heating of the vicinity of the electrode resulting from the overpotential needed to drive the reaction can be used to further promote CO_2 desorption from the amine

absorber near the cathode electrode.[122] Still, the maximum flux of dissolved CO_2 from the bulk of the electrolyte under steady state conditions will not be larger than that given by Equation 3.11.

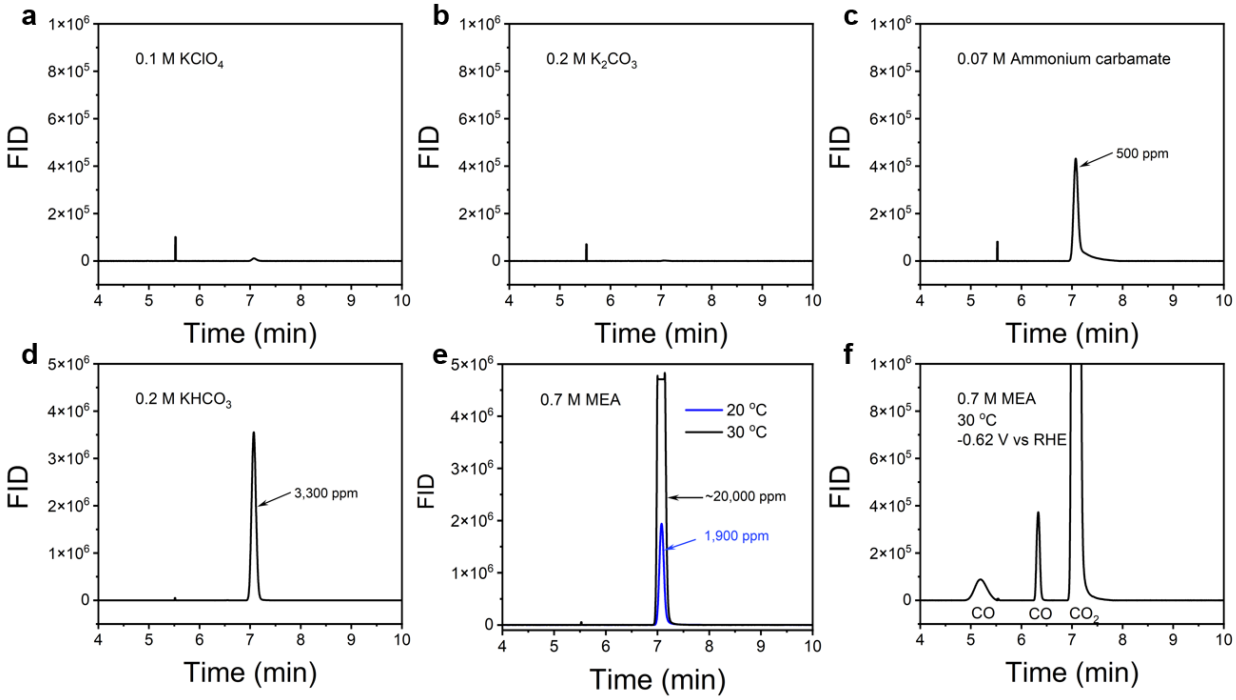

Figure 3.7: CO_2 signal in on-line gas chromatogram for different electrolytes. (a) 0.1 M $KClO_4$, (b) 0.2 M K_2CO_3, (c) 0.07 M Ammonium carbamate, (d) 0.2 M $KHCO_3$, (e) 0.7 M MEA at 20 and 30 ^oC, and (f) CO peak during electrochemical reduction of the solution in (e) on a silver electrode.

The FID signals in the gas chromatogram detector after 80 minutes of equilibration between the gas and liquid phase in the electrochemical cell are shown in Figure 3.7 for various electrolyte compositions where the retention time for CO_2 in the gas chromatography analysis is around 7.1 minutes. The 0.1M $KClO_4$ solution and 0.2 M K_2CO_3 solutions (Figure 3.7a and Figure 3.7b) show no CO_2. The pH of the K_2CO_3 solution here is 11.7 which indicates that the concentration of bicarbonate is very low and thus the release of CO_2 is insignificant as any released CO_2 at this pH is likely to react back with hydroxyls to form carbonate. The 0.07 M ammonium carbamate and 0.2M $KHCO_3$ solutions, Figure 3.7c and Figure 3.7d, show a CO_2 peak where the concentration of CO_2 is larger for the bicarbonate solution. Figure 3.7e shows CO_2 peaks of the 0.7 M MEA solution at different temperatures where the solutions were previously saturated with CO_2 and purged with N_2 for 6 hours, at temperatures above 30 ^oC these concentrations are higher

than 20,000 ppm or 2vol% CO_2 which is an order of magnitude higher than that at 20°C. It should be evident at this point that ammonium carbamate, potassium bicarbonate and CO_2-rich MEA solutions release CO_2 and that this CO_2 is in equilibrium with the CO_2 dissolved in solution in the RCE cell. The appearance of a CO peak in the FID detector during the electrochemical reduction of a CO_2-rich MEA solution on a silver catalyst electrodeposited on a Titanium cylinder electrode is shown in Figure 3.7f. The CO signal is much smaller than that of the CO_2 in the headspace of the cell and implies that the fraction of CO_2 electrocatalytically transformed to CO is much lower than the free CO_2 in the system. The second CO peak at a retention of 5 minutes corresponds to the CO reaching the FID detector via a first column in a gas chromatogram equipped with two separation columns for complex hydrocarbon mixtures (the rotation of the valve between columns is at 5.5 minutes).

3.2.9 Experimental procedures for the determination of potential dependence of CO_2-adduct reduction in capture solutions.

In a typical experiment for experimental determination of potential dependence of CO_2-adduct reduction in capture solutions, the rotation speed of the cylinder electrode in the RCE cell was fixed at the start of the experiment and kept constant during the whole duration of the test. Ar was first flowed at a rate of 20 sccm for at least 60 minutes in both the working and counter electrode compartments to make sure that the compositions of gases in the headspace of the working electrode compartment are stable before any further electrochemical tests. The gas flow rates were maintained throughout the electrochemical measurements, and the outlet gas was continuously sent for analysis using online gas chromatography (GC).

RCC testing was performed using chronopotentiometry, making step changes in total current density every 60 minutes. The currents tested were 1, 4, 8, 12, 20, and 28 mA cm^{-2}. The electrode potentials were recorded during the electrochemical reduction process. Additionally, electrochemical impedance spectroscopy (EIS) was conducted under each current density for a duration of 5 seconds prior to the electrolysis.

Gas samples were analyzed at 20-minute intervals. As a result, the gas phase was sampled at 20, 40, 60 min under the current density of 1 mA cm^{-2}; 80, 100, 120 min under the current density of 4 mA cm^{-2}; 140, 160, 180 min under the current density of 8 mA cm^{-2}; 200, 220, 240 min under the current density of 12 mA cm^{-2}; 260, 280, 300 min under the current density of 20 mA cm^{-2}; and 320, 340, 360 min under the current density of 28 mA cm^{-2} from the start of the RCC test. A total of 18 samples from the gas headspace were taken and measured on-line to quantify the CO_2, H_2 and CO partial pressures. See Figure 3.17 and Figure 3.18 for representative examples of the time dependence of the data generated.

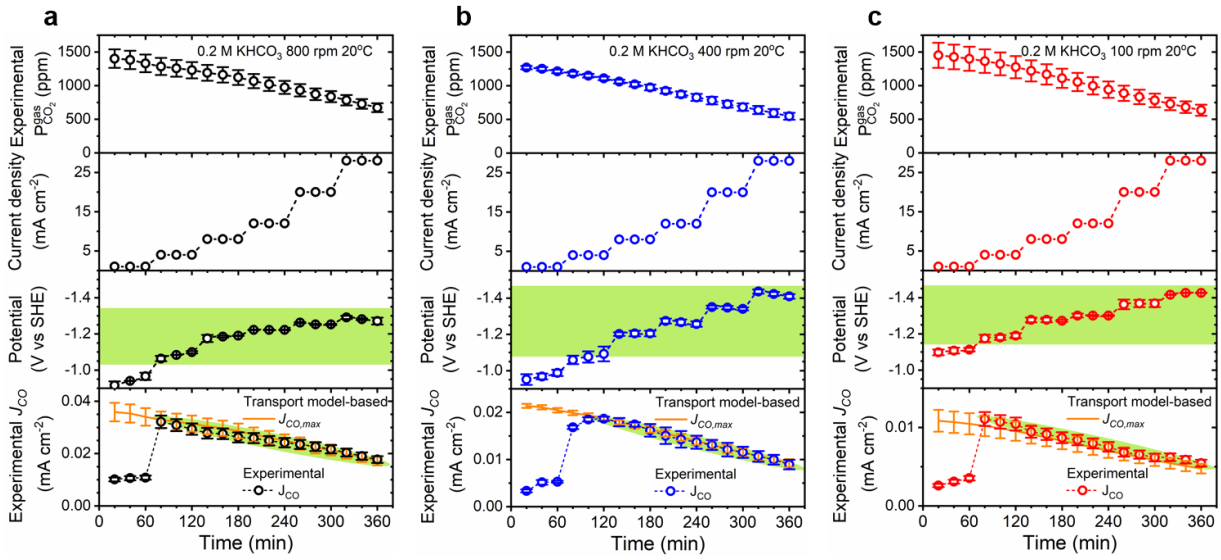

Figure 3.8: Experimental data collected as a function of time in CO_2 partial pressure, applied total current densities, electrode potentials, and partial current density of CO with the corresponding transport model-based $j_{CO_2,max}$ for 0.2 M potassium bicarbonate under a rotational speed of (a) 800 rpm (in duplicate). (b) 400 rpm (in triplicate). (c) 100 rpm (in duplicate).

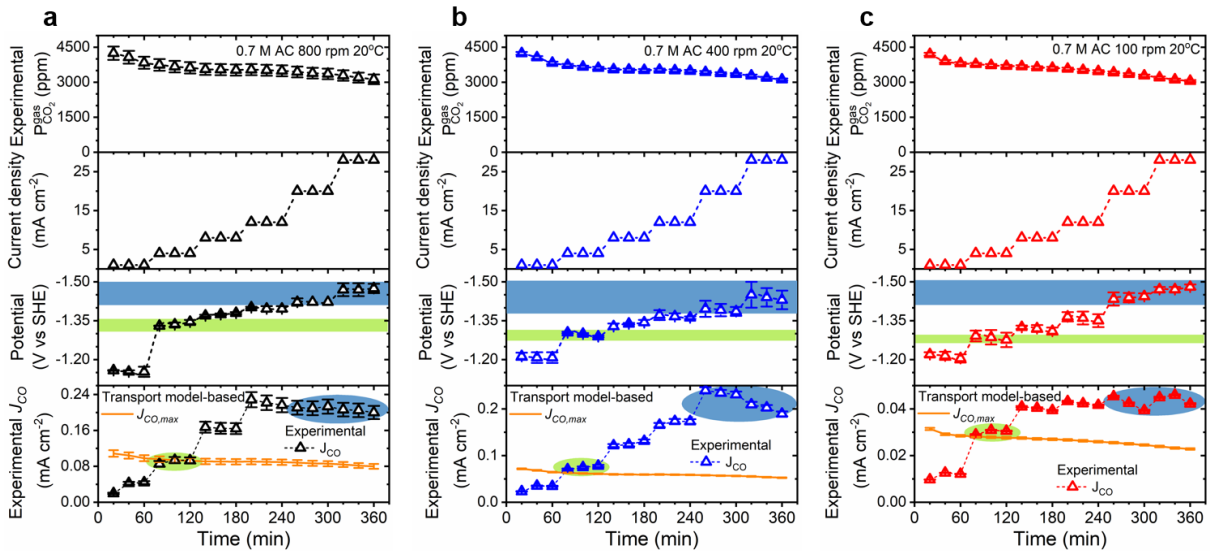

Figure 3.9: Experimental data collected in duplicate as a function of time in CO_2 partial pressure, applied total current densities, electrode potentials, and partial current density of CO with the corresponding transport model-based $j_{CO_2,max}$ for 0.7 M ammonium carbamate (AC) under a rotational speed of (a) 800 rpm. (b) 400 rpm. (c) 100 rpm.

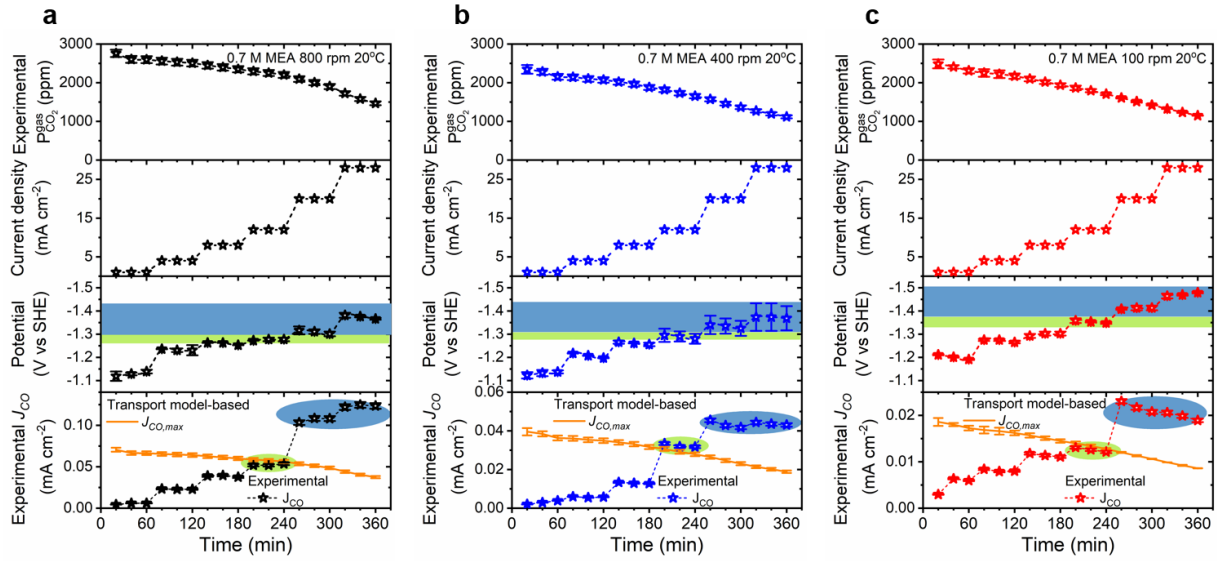

Figure 3.10: Experimental data collected in duplicate as a function of time in CO_2 partial pressure, applied total current densities, electrode potentials, and partial current density of CO with the corresponding transport model-based $j_{CO_2,max}$ for 0.7 M monoethanolamine (MEA) under a rotational speed of (a) 800 rpm. (b) 400 rpm. (c) 100 rpm.

High consistency and reproducibility of the experiments reported here can be seen from a typical triplicate experiment in Figure S16. Here, the error bars on the experimental data collected in triplicate correspond to the standard deviation and are reported as a function of time. Standard

deviations are given for CO_2 partial pressure, electrode potentials (currents were fixed in these experiments), and partial current densities for CO as well as the the corresponding transport model-based $j_{CO,max}$. The data in Figure 3.24 is the average of the three data points obtained for each current density and shown in the time dependent Figures below.

3.2.10 Experimental procedures for the distinction of carbamate, bicarbonate and dissolved CO_2 in RCC.

Although the preparation of the electrolytes and the setting of the experimental cell is identical for the data reported in Figure 3.16 and Figure 3.24, the duration of the experiments is different and for the data in Figure 3.16 only one current density was tested per experiment.

The electrochemical amine-captured CO_2 reduction data in Figure 3.16 was generated using chronopotentiometry under constant current densities for only 120 minutes. For the experimental results shown in Figure 3.16, the corresponding applied total current densities are listed below:

800 rpm (0.7M AC 10 °C) 12 mA cm^{-2}

800 rpm (0.7M AC 20 °C) 4 mA cm^{-2}

800 rpm (1.4M AC 20 °C) 8 mA cm^{-2}

800 rpm (0.7M AC 30 °C) 4 mA cm^{-2}

800 rpm (0.7M MEA 20 °C) 12 mA cm^{-2}

800 rpm (0.7M MEA 30 °C) 4 mA cm^{-2}

800 rpm (0.7M MEA 40 °C) 4 mA cm^{-2};

800 rpm (0.2M $KHCO_3$ 20 °C) 4 mA cm^{-2};

400 rpm (0.7M MEA 20 °C) 12 mA cm^{-2};

400 rpm (0.2M $KHCO_3$ 20 °C) 4 mA cm^{-2};

100 rpm (0.7M MEA 20 °C) 12 mA cm^{-2};

100 rpm (0.2M $KHCO_3$ 20 °C) 4 mA cm^{-2}.

The electrode potentials were recorded during the electrochemical reduction process. Additionally, electrochemical impedance spectroscopy (EIS) was conducted for a duration of 5

seconds prior to the electrolysis. Gas samples were analyzed at 20-minute intervals. As a result, the gas phase was sampled at 20, 40, 60, 80, 100, 120 min from the start of the electrochemical amine-captured CO_2 reduction process. A total of 6 sampling points were collected in-situ with CO_2 partial pressure, electrode potential and CO partial pressure for each. Only one current density was tested per electrode.

3.3 Results and discussion

3.3.1 Theoretical determination of competitive mechanisms for carbamate reduction on Ag.

The thermodynamic feasibility of transforming carbamate on a metal electrode in the presence of potassium cations was first studied using quantum mechanics (QM). In order to account for the effect of the applied potential at the electrode, grand canonical DFT (GCDFT) calculations were carried out explicitly, including the charge polarization that results from the applied potential. This is combined with an implicit model of the water solvent and the electrolyte. GCDFT calculations allow to change the electronic charge at the surface to keep the work function constant, thus keeping the potential constant, along the reaction pathway. A thermodynamic analysis has been chosen here as it is sufficient to explain trends for electrochemical reductions,[143] while circumventing the substantial uncertainties in sampling the solvent microenvironment required to model free energy barriers along electrocatalytic pathways.

Figure 3.11 shows the proposed competitive mechanism of electrochemical carbamate reduction on Ag. Firstly, due to its negative charge, carbamate experiences repulsion from the electrode surface under reductive potential, making it difficult to approach. Cations within the double layer can bind with the carbamate and facilitate the electron transfer from the electrode to the carbamate for its further reduction, which has been proposed in previous works[15] (Figure 3.3). The carbamate undergoes either a C-N cleavage coupled to a proton-electron transfer to generate physisorbed CO_2 and the amine RNH_2 (blue pathway) or a direct proton-electron transfer on the

carbamate to form the *RNHCOOH intermediate (orange pathway, *indicates a chemisorbed species on the Ag electrode). On the blue pathway, once CO_2 is formed, it chemisorbs on the Ag surface and is reduced subsequently to *CO via two proton-electron transfer steps, which is the typical CO_2 reduction reaction (CO_2RR) pathway on Ag.[144] The blue pathway therefore generates CO_2 by initial carbamate decomposition and reduces that CO_2 to CO on the Ag catalyst. In contrast, the orange pathway directly reduces the carbamate, initially keeping the C-N bond formed. Two choices exist after forming *RNHCOOH. One is to break the C-N bond to generate *COOH on the surface (green path) while the other choice is to further reduce it by proton-electron transfer to *RNHCO and water (orange path). Consequently, *RNHCO undergoes an additional proton-electron transfer on N and C-N bond cleaves to form *CO, and restore the amine simultaneously. In short, along the pathway, C-N bond cleavage and further reduction of CO_2 competes with the direct proton-electron transfer to O in the -CO_2 group of the carbamate and C-N cleavage at a later step, thus creating three possible bifurcating pathways.

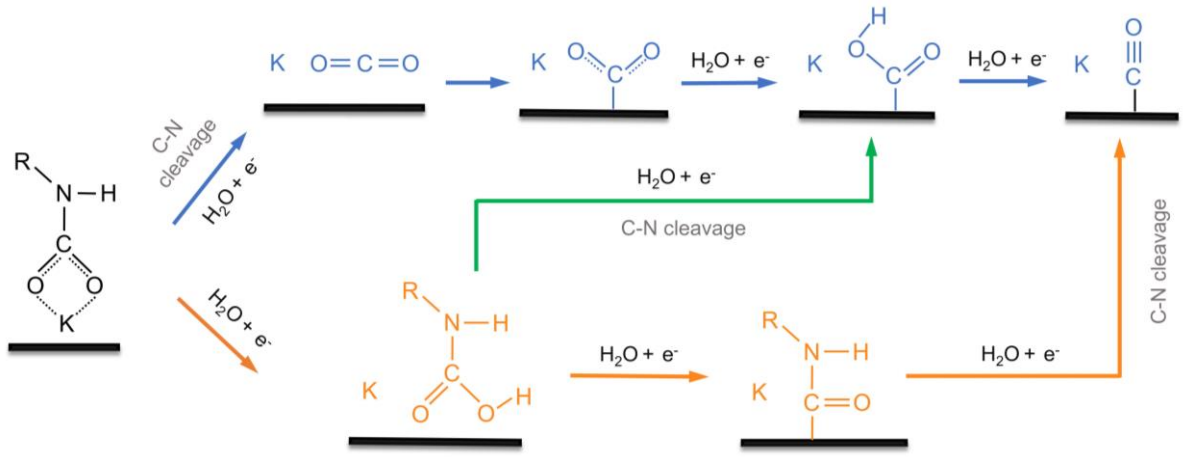

Figure 3.11: Proposed mechanism for the competition between electrochemical carbamate decomposition combined with CO_2 electroreduction (blue pathway) and carbamate direct reduction (orange pathway). The C-N bond cleavage can occur at three possible steps in the mechanism. K is the alkali metal potassium. The C-N bond cleavage can occur at three possible steps in the mechanism. K is the alkali metal potassium.

Ammonia, the simplest capture agent among amines, is chosen here as a model to explore the competitive reaction mechanism of decomposition or direct reduction of the carbamate, in the

presence of K^+ cations. The pH at the interface between the electrode and electrolyte solution can be significantly different from the bulk pH due to the transport of ions and molecules. Under reduction conditions, the transport of hydroxide anions from the electrode surface to the bulk is slow relative to the rate of hydroxide production, leading to an accumulation of hydroxide anions and an increase in pH at the interface.[145, 146] Thus, we chose pH =14 in our calculations, which is a reasonable approximation for the interfacial pH under reduction conditions. The proton source in alkaline conditions is molecular water which produces one hydroxyl equivalent per electron transferred at the electrode interface. The potential here is fixed at -1.3 V vs SHE and at such a negative potential it is markedly exothermic for the carbamate to either break the C-N bond to form CO_2 and NH_3 or be reduced to $*NH_2COOH$ (Figure 3.15). The energetics of these two steps are strongly dependent on the electrode potential since both of them contain one proton-electron transfer. When the potential is extrapolated to 0 V vs SHE, both steps are endothermic, consistent with the thermodynamic stability of captured CO_2.

Once the CO_2(g) forms (blue path), it will adsorb to the surface at the negative potential, with a reaction free energy of +0.36 eV at -1.3 V vs SHE. This adsorption step is known to be rate-limiting for CO_2 reduction on Ag. Previous research has indicated that CO_2 with a significant dipole moment is responsive to the surrounding electric field. In this study, explicit cation modeling was employed to stabilize such intermediates effectively through the manipulation of field-dipole interactions. Adsorbed $*CO_2$ will be further reduced to *COOH in a slightly endergonic step, since the chemical potential of the proton is quite low from the high pH conditions. *COOH will undergo one proton-electron transfer to form *CO which will then desorb from the surface, both steps being exothermic. Conversely, along the orange direct carbamate reduction pathway, $*NH_2COOH$ is physisorbed to the surface, not bonded to the K^+ cation. $*NH_2COOH$ can undergo a C-N bond cleavage coupled to one proton-electron transfer to form NH_3(g) and *COOH on the surface (green path) with a reaction free energy of 0.45 eV.

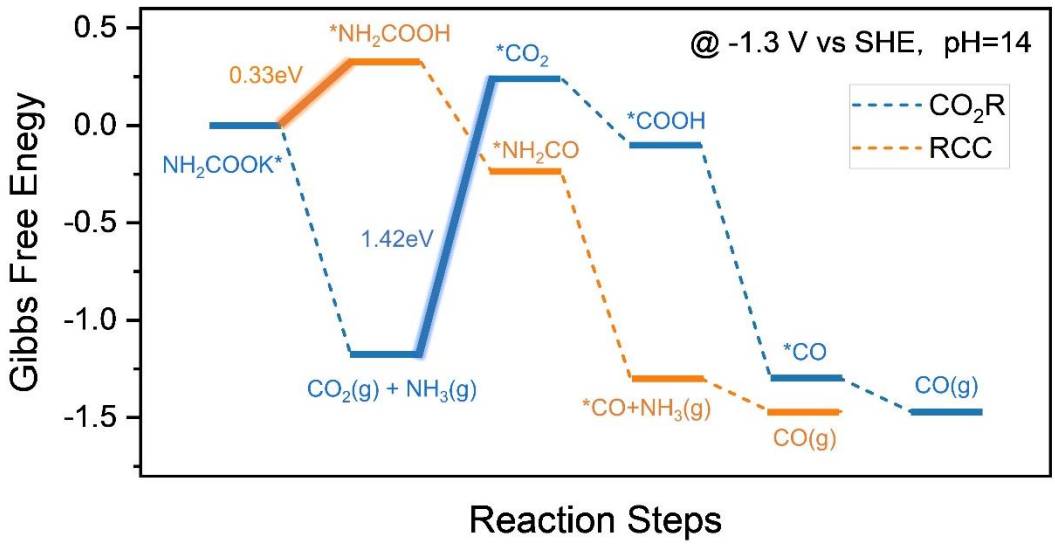

Figure 3.12: Gibbs free energy diagram for captured CO_2 reduction on Ag (111) at -1.3 V vs SHE, T = 300 K and pH=14 using constant charge calculation.

A thermodynamically more difficult direct proton-electron transfer process is to cleave a CO bond and form adsorbed *NHCO and water (reaction free energy of 0.49 eV, orange path) from the physisorbed *NH_2COOH. This implies that breaking the C-N bond at this stage is more favorable than further direct reduction. If the *COOH forms, then it will rejoin the blue CO_2RR pathway. Although the cleavage of the C-N bond of *NH_2CO to form *CO is also strongly exergonic, it is blocked by the difficult former reduction step to form *NH_2CO. In contrast, more standard calculations performed at “zero charge” that do not take into account the polarization of the electrode surface induced by the applied potential (and do not use the Grand Canonical DFT approach otherwise used here) show the opposite result. Such zero charge calculations suggest that at -1.3 V vs SHE the direct carbamate reduction pathway (RCC pathway in Figure 3.12) is much more favorable than the indirect pathway where carbamate decomposes first and then CO_2 is reduced (CO_2R pathway in Figure 3.12). The discrepancy versus experiment in the zero charge calculations arises from the unreasonable description of the cation atom and from the destabilization effect of the *CO_2 intermediate (Figure 3.12).

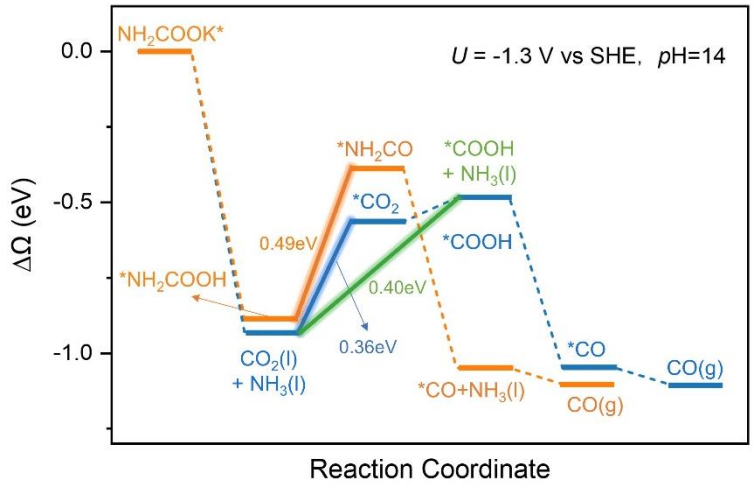

Figure 3.13: Competitive energetics for carbamate decomposition followed by CO_2 reduction (blue line) versus carbamate direct reduction (orange/green line) on Ag (111) along the three paths of Figure 3.11 (colors match those of Figure 3.11). Grand canonical free energy ($\Delta\Omega$) diagram of ammonium-carbamate reduction at -1.3 V vs SHE, T = 300 K and pH = 14 using grand canonical DFT calculation. The pressure for CO_2 and NH_3 is set as 0.3 kPa and 0.1 kPa.

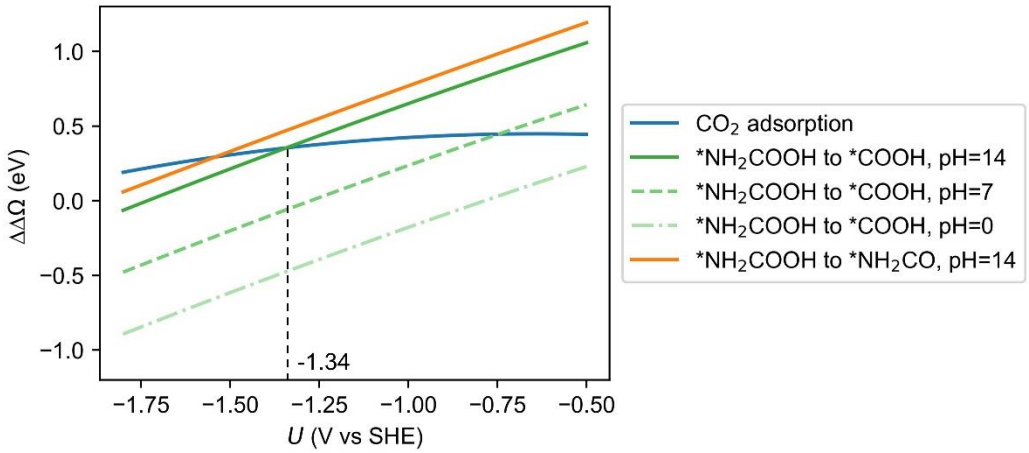

Figure 3.14. Comparison of potential-determining steps for the three pathways. Grand canonical reaction free energy ($\Delta\Delta\Omega$) as a function of potential for three elementary steps, CO_2 chemisorption (potential determining for the blue pathway, blue line), C-N bond cleavage of $*NH_2COOH$ to form *COOH (potential determining for the green pathway, green line) and protonation of $*NH_2COOH$ to $*NH_2CO$ (potential determining for the orange pathway, orange line). The solid line corresponds to pH=14, the dashed line to pH=7 and the dash-dot line to pH=0. The pressure for CO_2 and NH_3 is set as 0.3 kPa and 0.1 kPa.

Comparing the three carbon upgrading pathways in Figure 3.15, breaking the C-N bond of NH_2COOK* and forming $CO_2(g)$ to undergo typical CO_2RR (blue path) is the most dominant path

in terms of thermodynamics. Physisorbed *NH_2COOH is relatively stable, which makes it hard for C-N bond cleavage or protonation to occur, thus the sluggish conversion of *NH_2COOH hinders the carbamate reduction pathway overall even under lower vapor pressures of CO_2 and NH_3 (Figure 3.13 and Figure 3.14). Clearly, three elementary steps, CO_2 adsorption, C-N bond cleavage of *NH_2COOH and direct protonation of *NH_2COOH compete and determine the reaction path and rate.

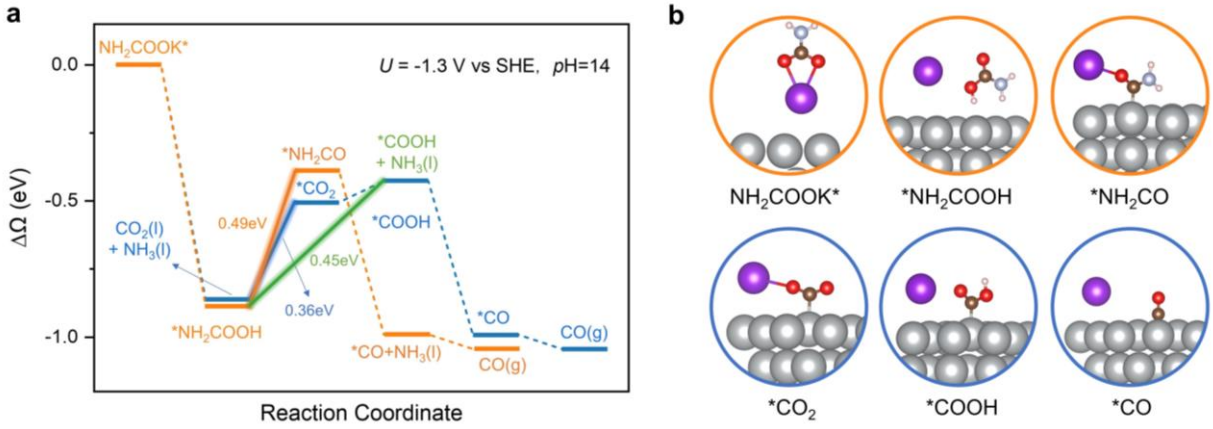

Figure 3.15: Competitive energetics for carbamate decomposition followed by CO_2 reduction (blue line) versus carbamate direct reduction (orange/green line) on Ag (111) along the three paths of Figure 3.11 (colors match those of Figure 3.11). (a) Grand canonical free energy ($\Delta\Omega$) diagram of ammonium-carbamate reduction at -1.3 V vs SHE, T = 300 K and pH = 14 using grand canonical DFT calculation. The vapor pressure for CO_2 and NH_3 are 0.4 kPa and 1 kPa respectively. (b) Side view of intermediates along the reaction pathway. Color code: Ag (gray), K (purple), C (brown), O (red), N (light blue) and H (white).

3.3.2 Experimental distinction of carbamate, bicarbonate and dissolved CO_2 in RCC.

Although theoretical calculations suggest that direct carbamate reduction is thermodynamically less favorable than CO_2 reduction, the experimental distinction of the different carbon sources in RCC systems is a technical challenge. Reducing directly (and efficiently) carbonates and carbamates was almost non-existing in the literature until the last few years.[147] The understanding in the past was that dissolved CO_2 was the only carbon source in these systems.[148] While various works by Perez-Gallent et al.[122] and Chen et al.[149] have already shown

that the carbon source were CO_2 molecules dissolved in solution rather than the major CO_2-containing species of carbamate and bicarbonate in the electrochemical reduction of amine-CO_2 solutions, in these works there is no explicit demonstration and/or quantification of the dissolved CO_2 in solution during electrocatalysis.

In order to experimentally interrogate the carbon source for the production of CO on silver electrodes, a gastight rotating cylinder electrode (RCE) cell (Figure 3.4) is utilized here with similar CO_2-amine and bicarbonate solutions as those reported by others for the direct electrochemical reduction of absorber solutions. The dissolved CO_2 in solution is estimated using Henry's Law as a fast quasi-equilibrium is reached at the gas/liquid interface in the cell between the dissolved CO_2 in the bulk of the liquid and the partial pressure of CO_2 under a constant flow of Ar through the cell. The partial pressure of CO_2 in the gas ($P_{CO_2}^{gas}$) is measured experimentally using an on-line gas chromatogram. The characterization of the gas/liquid equilibrium in the cell under RCC tests are well described in Methods. The concentration of dissolved CO_2 in the solution is then used to determine mass transport limited current densities for the reduction of CO_2 to fuels and chemicals in electrochemical cells of well-characterized mass transport such as the one used in this work.

From Henry's Law, it is known that the concentration of dissolved CO_2 in equilibrium with 1 bar of CO_2 is 34 mM at 20 °C. The maximum flux of CO_2 to the surface of the electrode ($J_{CO_2,max}$) is the product of the concentration of dissolved CO_2 in the bulk ($C_{CO_2,bulk}$) and the mass film transfer coefficient for CO_2 in the liquid (k_{m,CO_2}) which can be tuned by changing the hydrodynamics in the proximity of the liquid/solid interface.[76, 84] Under mass-transport limited conditions, the concentration of CO_2 at the surface of the electrode is close to zero so that Equation 3.11 can be used to calculate $J_{CO_2,max}$.

$$J_{CO_2,max} = k_{m,CO_2} C_{CO_2,bulk} \tag{3.11}$$

The maximum partial current density for CO ($j_{CO_2,max} = 2FJ_{CO_2,max}$) calculated from the maximum CO_2 flux in Equation 3.11 is shown in Figure 3.16. Here, this *transport model-based* maximum current density is denoted by solid lines for the systems operating at 100 rpm, 400 rpm and 800 rpm. The dependence of the mass film transfer coefficient with the hydrodynamics in the RCE cell is well-characterized and is given by Equation 3.10.

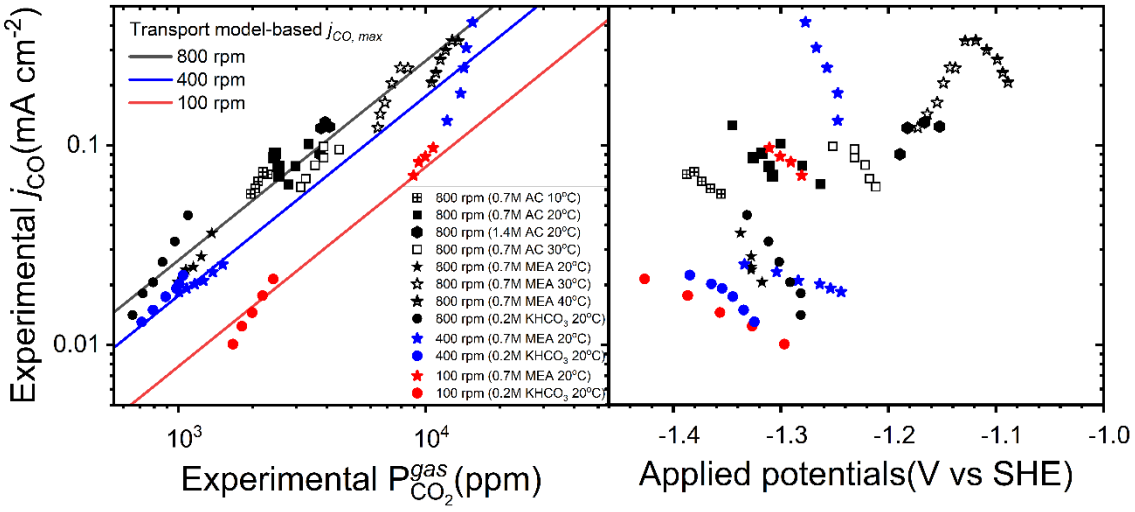

Figure 3.16: Left panel: Experimental and transport model-based maximum partial current density for the reduction of dissolved CO_2 in a solution at equilibrium with a partial pressure of CO_2 determined using a gas chromatogram. Right panel: Applied potential versus partial CO current density for experimental data in Left panel.

Figure 3.16 shows the transport model-based and experimental maximum partial current densities for the production of CO (j_{CO}) on a silver rotating cylinder electrode for multiple absorber-CO_2 solutions at temperatures between 20 and 40 °C and under three different electrode rotation speeds of 100, 400 and 800 rpm. The agreement between the partial current densities observed and those theoretically calculated for the reduction of dissolved CO_2 in equilibrium with the partial pressure of CO_2 in the cell's overhead indicates that the production of CO is indeed limited by the transport of dissolved CO_2 from the bulk of the electrolyte to the catalyst. Small deviations between the experimentally measured j_{CO} to the maximum partial current densities calculated from the transport model in Figure 3.16 could originate from the fact the restructuring, corrosion, and poisoning of the catalyst are not considered in the $j_{CO_2,max}$ calculations.

Although the simple transport model used in this work to estimate $j_{CO_2,max}$ captures well the general relationship between the measured partial pressure of CO_2 and the CO partial current density across different experimental conditions, various surface phenomena such as catalyst restructuring, corrosion, and poisoning are not considered. These phenomena can result in deviations in the experimentally observed partial CO current densities compared to the maximum CO currents calculated by the transport model.

One experimental observation that we have made so far when testing other metals such as copper, is that copper electrodes corrode under experimental RCC conditions turning the solution blue as it is characteristic of the presence of Cu^{2+} cations in solution. Gold, on the other hand, appears to be poisoned as its activity decreases over time. The rates of corrosion and the degree of poisoning of copper and gold metals are a function of the capture solutions used. For simplicity, experimental data on copper and gold are not reported here as these metals required detailed characterization and analysis that are beyond the scope of this work. However, Figure 3.5 already demonstrates that the silver catalyst restructures during testing. Restructuring is likely to involve the adsorption of capture agent molecules on the surface and the movement of atoms over long distances on the surface of the electrode. The simple transport-based model indeed ignores restructuring, corrosion, as well as the irreversible absorption of molecules on the surface of the catalyst. The difference in absorption energies of the different amines as well as the differences in kinetics of the various restructuring processes are likely to impact the slopes seen in Figure 3.16 as the experimental data is obtained over multiple hours of testing. Nevertheless, on the whole, the simple transport-based model captures well the relations between partial pressure of CO_2 and CO partial current density.

The bubble formation and heat dissipation at the electrode interface may also affect the partial current densities of CO observed. Here, we have compared the experimental data for the reduction of different capture solutions under identical current densities, similar applied potentials, and the same rotational speed (Figure 3.17 and Figure 3.18), and analyzed how the partial

pressure of CO_2, potential, and CO partial current density evolves over 6 hours of testing to understand the extent of their impact.

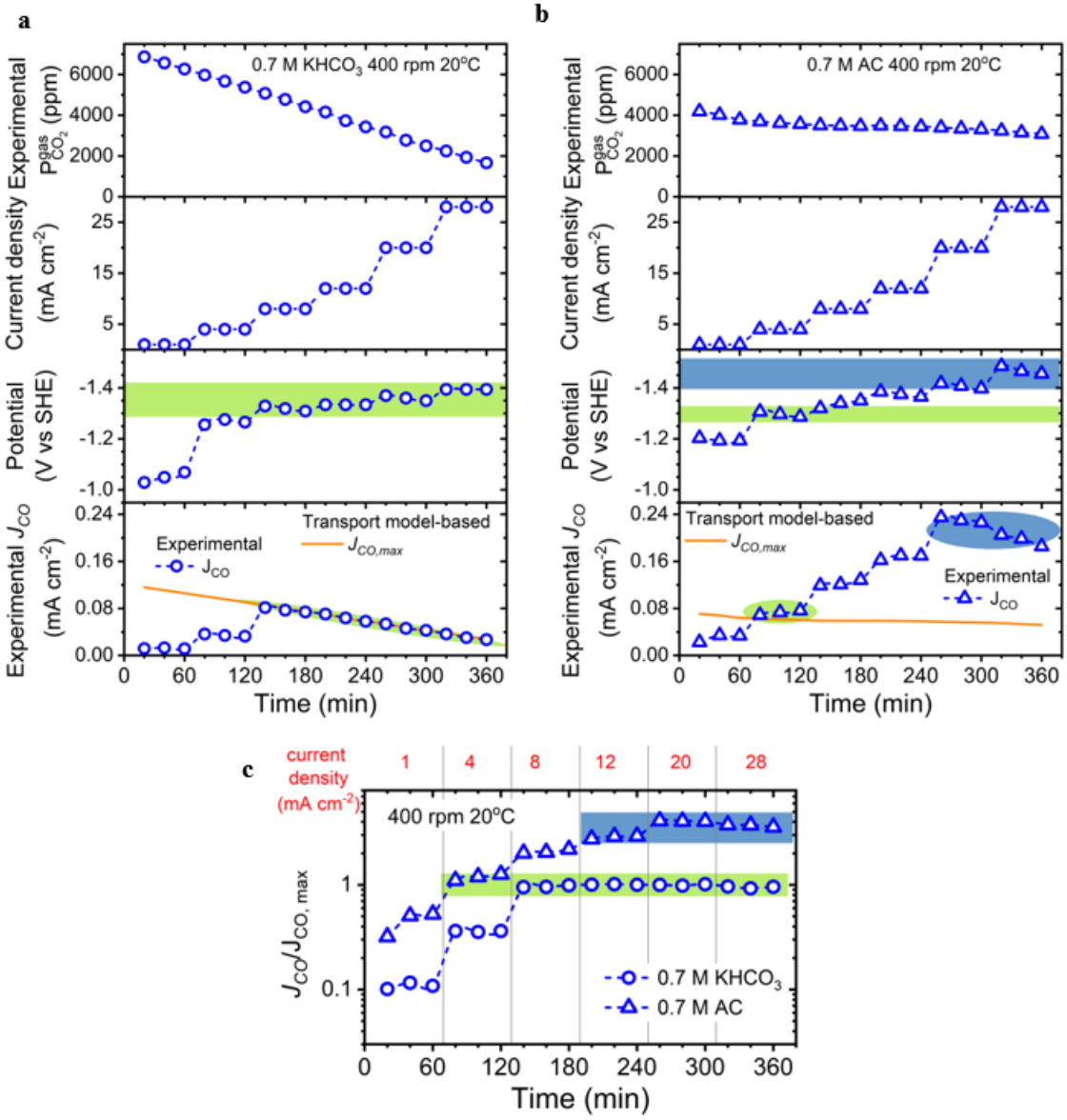

Figure 3.17: Comparison of the reduction of dissolved CO_2 in different capture solutions under a rotational speed of 400 rpm. Experimental data is shown as a function of time for CO_2 partial pressure, applied total current densities, electrode potentials, and partial current density for CO with the corresponding transport model-based $j_{CO_2,max}$ for (a) 0.7 M potassium bicarbonate and (b) 0.7 M ammonium carbamate (AC) electrolytes. (c) Ratio between partial current density for CO and the model-based maximum CO partial current if the CO_2 source is purely dissolved CO_2 in the bulk of the electrolyte.

Figure 3.17 compares the experimental observations for 0.7 M $KHCO_3$ and 0.7 M AC solutions. In both experiments, the partial pressure of CO_2 in the headspace decreases as a function of time although the decrease in partial CO_2 pressure occurs faster in the $KHCO_3$ solution. To achieve the same current densities in both solutions, the applied potential is similar and in the range of -1.2 to -1.5 V vs SHE. Here, it is safe to assume that because the main reduction product is hydrogen in both electrolytes, the bubble formation rate and heat dissipated due to the overpotential at the electrode/electrolyte interface in both solutions are to a large extent similar. While for the bicarbonate electrolyte, the experimental CO partial current is identical to that expected from the mass transport model at any current higher than 8 mA cm^{-2} (green shade in Figure 3.17), the experimental CO partial current densities in the AC electrolyte are higher than those calculated from the transport model-based $j_{CO_2,max}$. A second plateau in CO partial current density (blue shade in Figure 3.17) is reached at current densities higher than 16 mA cm^{-2} after more than 4 hours of testing which could indicate the deactivation of the catalyst to an extent that was not obvious in the experiments carried out in the bicarbonate solution.

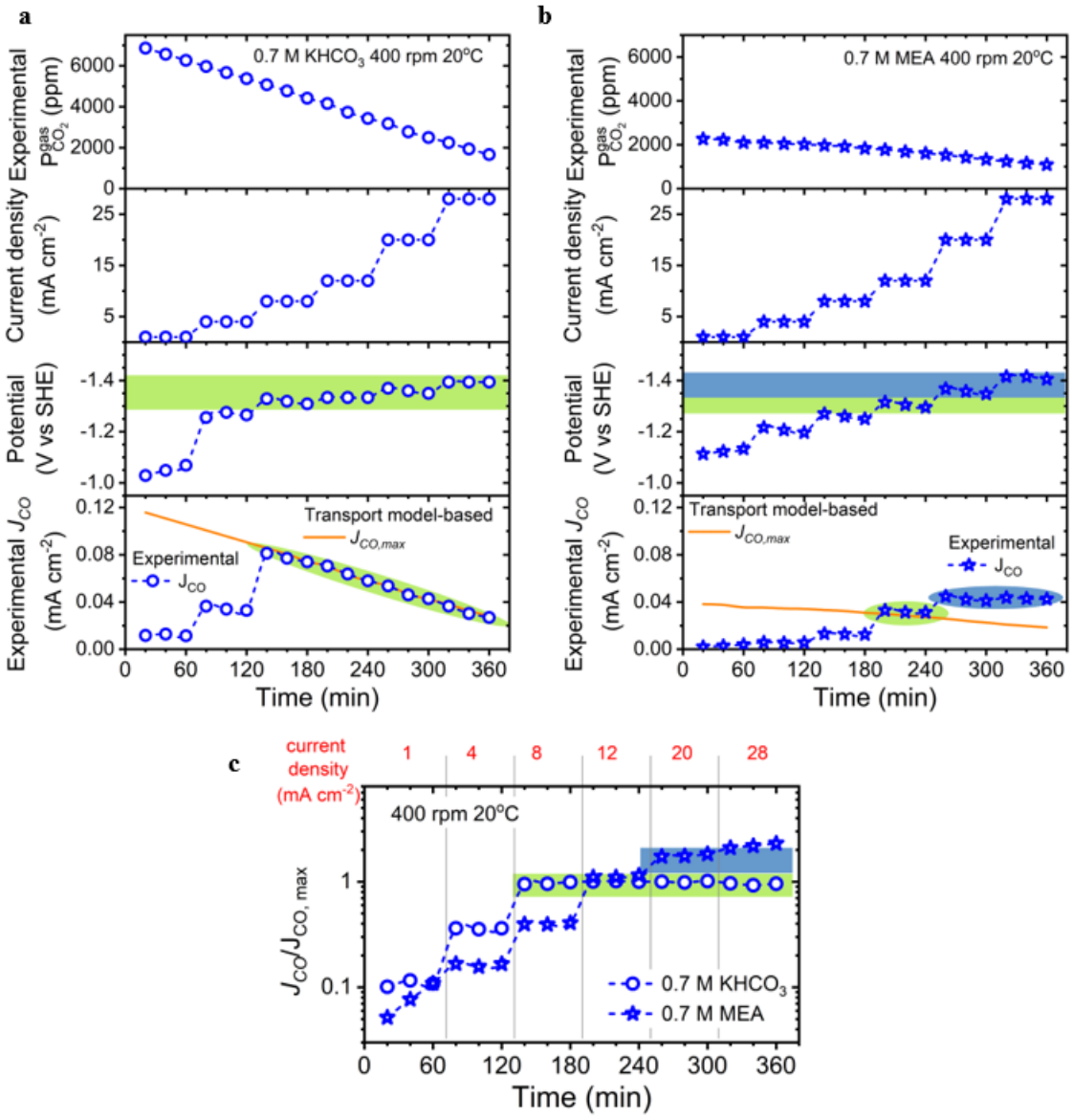

Figure 3.18: Comparison of the reduction of dissolved CO_2 in different capture solutions under a rotational speed of 400 rpm. Experimental data is shown as a function of time for CO_2 partial pressure, applied total current densities, electrode potentials, and partial current density for CO with the corresponding transport model-based $j_{CO_2,max}$ for (a) 0.7 M potassium bicarbonate and (b) 0.7 M monoethanolamine (MEA) electrolytes. (c) Ratio between partial current density for CO and the model-based maximum CO partial current if the CO_2 source is purely dissolved CO_2 in the bulk of the electrolyte.

Figure 3.18 compares the same 0.7 M $KHCO_3$ solution against the experimental data obtained in the CO_2 loaded 0.7 M MEA electrolyte. Similar to the AC solution, the partial current density for CO reaches the $j_{CO_2,max}$ at potentials negative of -1.3 V vs SHE and a second plateau

is also reached after 4 hours of testing despite $j_{CO_2,max}$ being reached just one hour earlier at 16 mA cm^{-2}.

When the data in Figure 3.16 is plotted in dimensionless terms, the $Sh/Sc^{0.33}$ values fall on the same universal line described by Equation 3.10 (Figure 3.6), indicating that CO_2 transport from the bulk is dominant and that contribution of chemical reactions within the liquid film are not significant. To calculate the $Sh/Sc^{0.33}$ number, we have assumed again that the concentration of dissolved CO_2 in the bulk of the electrolyte is in equilibrium with the partial pressure of CO_2 and is described by Henry's Law.

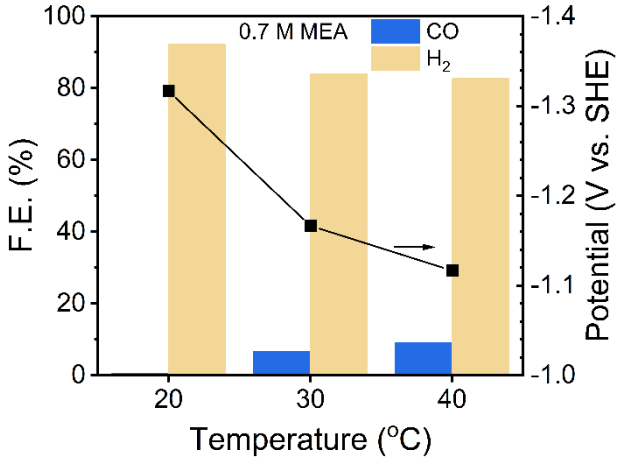

Figure 3.19: Faradaic efficiency and applied potential during the electrochemical reduction of a 0.7 M MEA electrolyte with a Ag electrocatalyst at a fixed current density of 4 mA cm^{-2} at an electrode rotation speed of 800 rpm. The pH at the beginning of the electrolysis is 8.1 and increases to 8.9 after 2 hours of testing.

Figure 3.19 shows the Faradaic efficiency for the reduction of a CO_2 loaded 0.7 M MEA solution on a silver cylinder electrode as a function of temperature and potential. As the temperature in the cell increases, the concentration of dissolved CO_2 in equilibrium with the solution increases and results in higher Faradaic efficiencies for CO and lower applied potentials at a fixed current density of 4 mA cm^{-2}. Faradaic efficiencies of up to 9% for CO are observed at a temperature of 40 ^{o}C which corresponds to a CO partial current density of 0.36 mA cm^{-2}. The partial current densities for CO as a function of potential (Figure 3.16) are similar to those

measured by Lee et al. for flat Ag electrodes.[132] Similar trends of activity and selectivity are observed in the same catalyst for a 0.7 M ammonium carbamate (AC) solution. At a constant temperature, higher overpotentials result in higher partial current densities for CO although the partial current density for CO reaches a plateau at high overpotentials (Figure 3.16). This plateau is proportional to the partial pressure of CO_2 in the headspace of the cell.

The cation effects and other phenomena observed by Lee at al. are likely arising from poor primary and secondary current distributions in their systems. Nonuniform primary and secondary current distributions arise from edge effects with and without the consideration for electrode polarization, respectively. Therefore, planar electrode geometry inherently suffers from nonuniform current distributions especially under high current and when combined with flow over the electrode, this leads to nonuniform concentration/pH gradient over the electrode surface along the direction of the flow creating local hotspots on the electrode.[150, 151] Such localization of electrochemical environment could be alleviated by adding more acidic metal cations such as potassium or cesium which contribute to the buffering of equilibrium reactions through hydrolysis releasing CO_2.[152, 153] The tailoring of the thickness at the electrode double layer is a complex explanation to the optimization of an electrochemical system which performs better as the concentration of the dissolved CO_2 is increased at higher temperatures, and as polarization resistances are decreased through the addition of a supporting electrolyte.

A first important conclusion from this systematic work in RCC is that while in CO_2 electrocatalysis it is common to report outputs such as partial current density and Faradaic efficiencies as a function of potential, in RCC studies it is necessary to measure and report the concentration of dissolved CO_2 in solution, the mass film transfer coefficient at the G/L and L/S interface, as well as the effect of temperature on these system variables. Dissolved CO_2 is not a directly measurable variable so it must be estimated indirectly from the CO_2 partial pressure in equilibrium with the CO_2 absorber liquid.

3.3.3 Theoretical determination of the effect of potential and pH on carbamate reduction mechanism.

Potential and pH effects on the reaction pathways are further discussed for the three competing elementary steps mentioned in the first part of this work, by representing the reaction free energy of the potential determining step for each path as a function of potential and pH (Figure 3.21). Since CO_2 adsorption is a chemical step rather than an electrochemical step, no proton transfer is associated, which means that this step is pH-independent. A slight stabilization effect on $*CO_2$ can be found as the electrode potential is more negative due to the increased injected charge (blue line). The injected charge as a function of electrode potential for different adsorbates are shown in Figure 3.20.

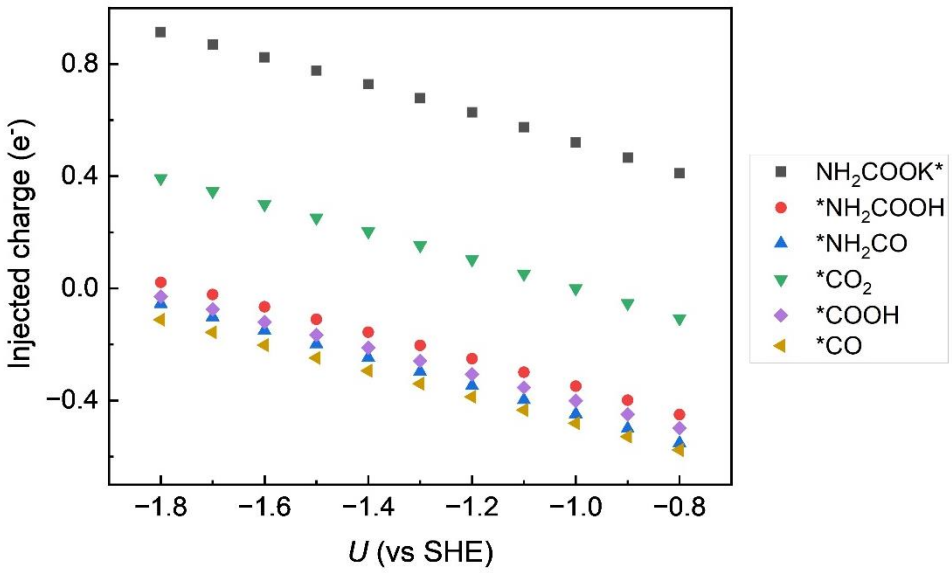

Figure 3.20: The injected charge as the function of electrode potential for different adsorbates.

The formation of *COOH by a coupled C-N bond cleavage and proton-electron transfer from the $*NH_2COOH$ intermediate (green line in Figure 3.21) is thermodynamically more favorable than the formation of $*NH_2CO$ which results from direct reduction of $*NH_2COOH$ (orange line) in a wide potential range (-0.5 V to -1.8 V vs SHE). Notably, at the alkaline condition of pH = 14, a crossover (at -1.45 V vs SHE) can be found between the blue line and green line. The blue path, with

carbamate decomposition, CO_2 chemisorption, and further reduction to CO, is favored when the potential is more positive than ~-1.45V vs SHE. However, if the potential is more negative than this crossover, breaking the C-N bond will be more thermodynamically feasible than CO_2 adsorption, which indicates that the potential-determining step (PDS) will change from CO_2 chemisorption, in the blue pathway, to C-N bond cleavage of the hydrogenated carbamate, in the green pathway. Such a shift of PDS can be rationalized by the fact that forming *COOH is an electrochemical step that contains one proton transfer. This step is then expected to be much more sensitive to the electrode potential than the chemical process of CO_2 chemisorption since the H chemical potential is linearly correlated to the potential. Moreover, the pH will also affect the chemical potential of the proton. A shift down of the green line can be seen when the solution is neutral (dashed line) or acidic (dash-dot line), suggesting that the crossover will shift to less negative potential as the solution pH decreases. In practice, however, as the pH decreases the protonation of the amine increases shifting the carbamate equilibrium towards the direction of faster release of CO_2 (Figure 3.4d).

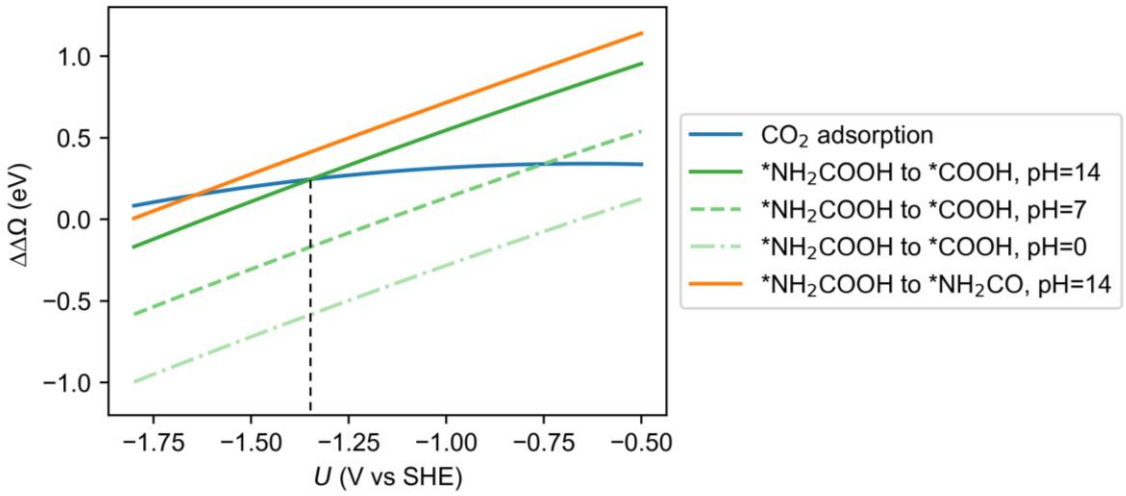

Figure 3.21: Comparison of potential-determining steps for the three pathways of Figures 1 and 2. Grand canonical reaction free energy ($\Delta\Delta\Omega$) as a function of potential for three elementary steps, CO_2 chemisorption (potential determining for the blue pathway, blue line), C-N bond cleavage of *NH_2COOH to form *COOH (potential determining for the green pathway, green line) and protonation of *NH_2COOH to *NH_2CO (potential determining for the orange pathway, orange

line). The solid line corresponds to pH=14, the dashed line to pH=7 and the dash-dot line to pH=0. The vapor pressure for CO_2 and NH_3 are 0.4 kPa and 1 kPa respectively.

In short, the chemical step of CO_2 chemisorption, which is the potential limiting step for the blue pathway is pH-independent and less sensitive to electrode potential while the C-N bond cleavage of the hydrogenated carbamate to form *COOH, potential limiting for the green pathway, is an electrochemical step whose reaction energy is strongly dependent on the pH and potential. Thus, tuning these two parameters could regulate the reaction mechanism. Specifically, a markedly negative potential and acidic pH should favor the direct carbamate reduction pathway joining the conventional CO_2 reduction mechanism at the *COOH intermediates while the initial carbamate decomposition, formation of CO_2 and conventional CO_2RR pathway will be dominant at less negative potential and basic pH.

3.3.4 Experimental determination of potential dependence of CO_2-adduct reduction in capture solutions.

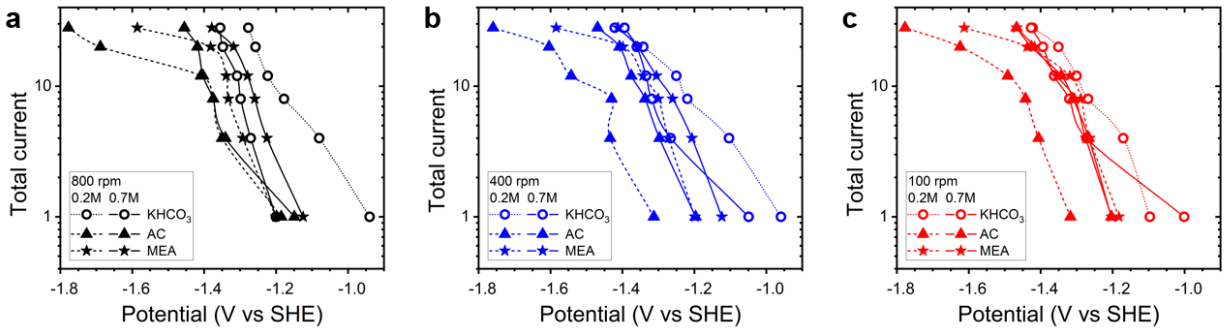

Figure 3.22: Current versus average potential data for constant current experiments during the electrochemical reduction of various CO_2 capture solutions. Each experiment is carried out by increasing the current every 60 minutes and determining the potential needed to drive a total current density of 1, 4, 8, 12, 20, and 28 mA cm^{-2}. (a) 800 rpm. (b) 400 rpm. (c) 100 rpm. The extended dataset with data points collected every 20 minutes are shown in Figure 3.8, Figure 3.9 and Figure 3.10.

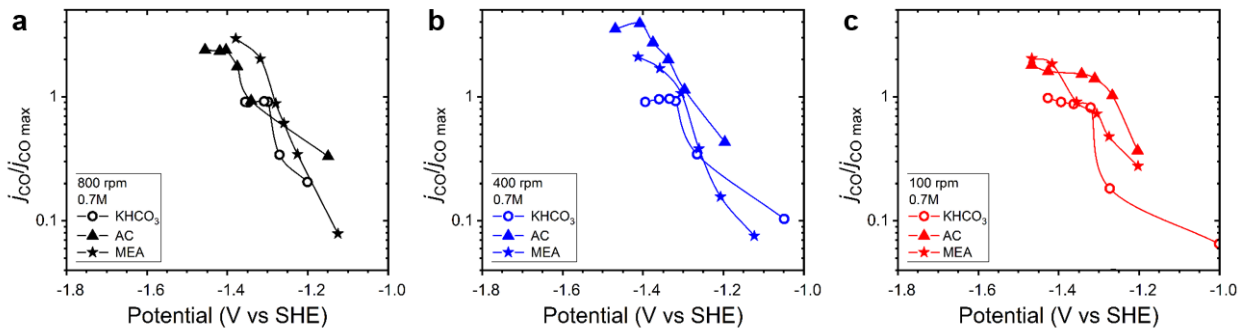

Figure 3.23: Ratio between experimental CO partial current density measured for various CO_2 capture solutions and the theoretical maximum CO partial current when only dissolved CO_2 in the bulk is the carbon source. Each experiment is carried out by increasing the current every 60 minutes and determining the potential needed to drive a total current density of 1, 4, 8, 12, 20, and 28 mA cm^{-2}. (a) 800 rpm. (b) 400 rpm. (c) 100 rpm.

In order to determine the effect of applied potential on the maximum rate of CO production from carbon capture solutions, we have carried sequential constant current measurements on various carbon capture electrolytes under different hydrodynamic conditions in the RCE cell. The details of experiments can be found in Methods. In each experiment, the current density was increased every 60 minutes to determine the potential needed to drive a total current density of 1, 4, 8, 12, 20, and 28 mA cm^{-2}. Less negative potentials are needed to drive the same current when the rotation speed of the electrode and the concentration of the amine are increased, likely due to the improved transport of the protonated amines that relay protons to the surface of the electrode where the main product of reduction is hydrogen (Figure 3.22 and Figure 3.23). Ammonium cations are formed during the CO_2 capture processes and these act as proton sources or proton relay agents for hydrogen evolution. The nature of the ammonium cation, namely, its pKa affects hydrogen evolution rates, onset potentials, and could play a large role in determining competitive absorption rates and the structure of the double-layer.

As time proceeds, the experimentally measured partial pressure of CO_2 in the cell overhead decreases meaning that experimental data in Figure 3.24a are organized chronologically from right to left for each experiment. That is, each of the six data points in one curve corresponds to the average partial current density for CO under each of the six total current densities driven

through the system. In 0.7 M potassium bicarbonate solutions, the partial current density for CO increases as the applied potential becomes more negative and reaches the maximum current density (solid lines in Figure 3.24a) expected at each of the different rotation speeds for a system where the only carbon source is dissolved CO_2 in the bulk of the electrolyte. Figure 3.24b shows that the ratio between the partial current density for CO and the maximum expected partial current density for CO calculated from the transport model in Equation 3.11 is equal to 1 at any potential negative of -1.3 V vs SHE for the bicarbonate electrolyte. If the concentration of bicarbonate is reduced to 0.2 M (Figure 3.24c and Figure 3.24d), the maximum partial current densities that can be obtained for CO are lower since the partial pressure of CO_2 in equilibrium with the solution is also lower and yet the only source of carbon is dissolved CO_2 in equilibrium with the partial pressure of CO_2 in the headspace.

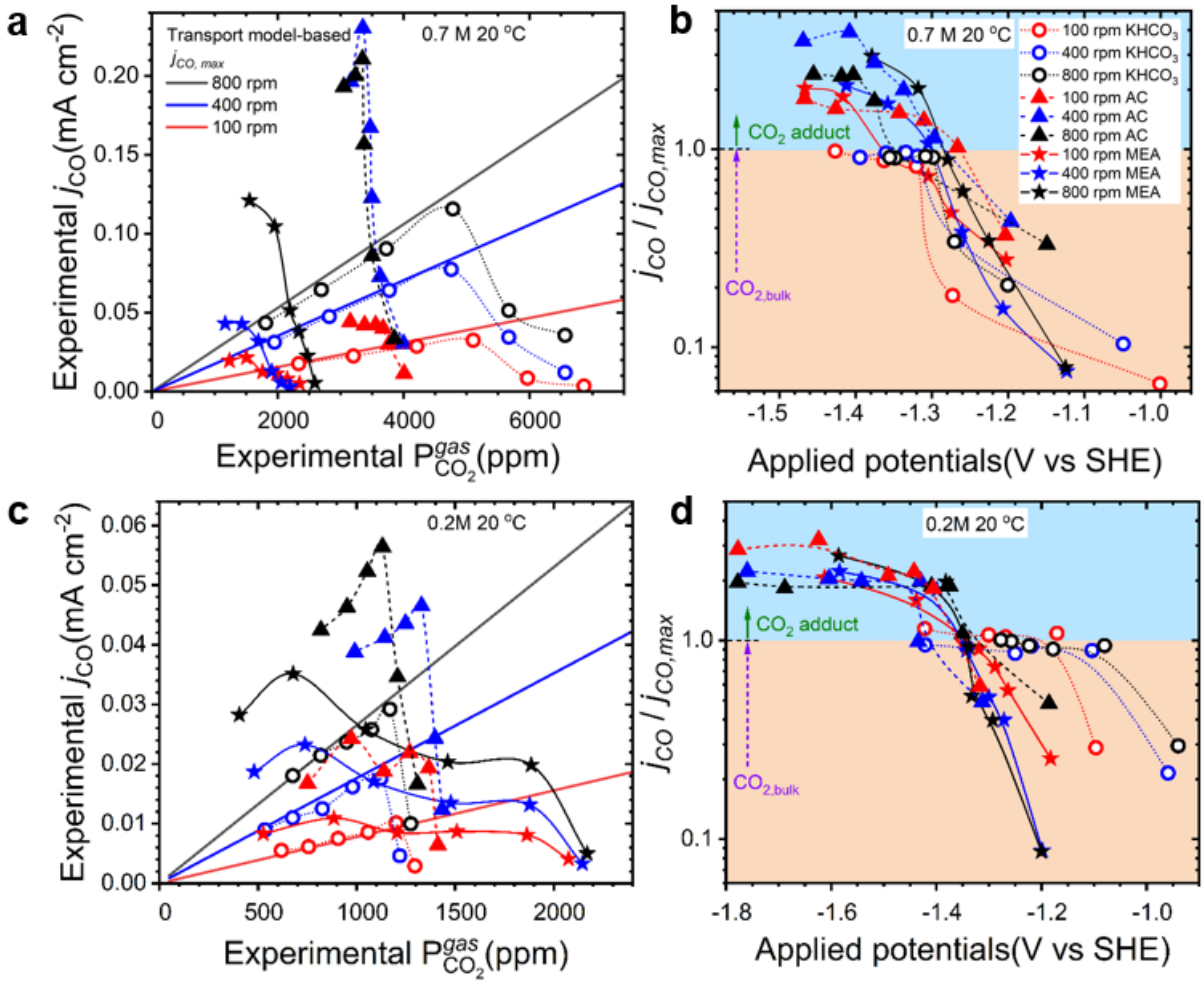

Figure 3.24: Experimental and transport model-based maximum partial current density for the reduction of dissolved CO_2 in capture solution at equilibrium with a partial pressure of CO_2 determined using a gas chromatogram. Each experiment is carried out by increasing the current and determining the potential needed to drive a total current density of 1, 4, 8, 12, 20, and 28 mA cm^{-2}. (a) Experimental partial current for CO in 0.7 M solutions of potassium bicarbonate, ammonium carbamate (AC) and CO_2-loaded MEA. (b) Ratio between partial current density for CO and the model-based maximum CO partial current if the CO_2 source is purely dissolved CO_2 in the bulk of the electrolyte. (c) Experimental partial current for CO in 0.2 M solutions of potassium bicarbonate, ammonium carbamate (AC) and CO_2-loaded MEA. (d) Ratio between partial current density for CO and the model-based maximum CO partial current if the CO_2 source is purely dissolved CO_2 in the bulk of the electrolyte.

Ammonium carbamate and saturated MEA solutions have a similar behavior to bicarbonate although a second plateau on the partial current density for CO is reached when the applied potentials are more negative than those reported in Figure 3.16. The CO partial current density reaches a plateau between 2 and 4 times higher than those measured for bicarbonate solution of

the same concentrations. The maximum partial current density for CO at high overpotentials is no longer only proportional to the partial pressure of CO_2 measured in the cell overhead but provides evidence for a role of the CO_2-absorber adduct to serve as a second carbon source. The ratio of the experimental partial current density for CO to the maximum partial current density for CO calculated from Equation 3.11 (Figure 3.23 and Figure 3.24b, d) are largely independent of the electrode rotation speed and indicate that the enhancement is proportional to the mass film transfer coefficient at the liquid/solid interface. The absolute increase in partial current density is proportional to the carbamate concentration and it could be argued that indeed direct carbamate reduction is possible at more negative potentials as suggested by theory.

Dynamic changes in speciation are largely ignored in bench-scale units utilized for basic RCC research. This is problematic because pumps, heaters and valves in bench-scale units are very much oversized relative to the catalyst electrode area. During scale-up, the relative size of pumps and heat exchangers compared to the electrode areas will be reduced and could reveal challenges with mass and heat transfer processes particularly at gas/liquid and liquid/solid interfaces. The lack of rigorous characterization of spatial and temporal speciation, even in the simplest of the RCC systems, can give rise to conflicting mechanisms and theories that could derail catalyst and absorber discovery efforts in the CCU field. pH also plays a significant role in changing speciation and CO_2 loading in RCC systems and must be carefully considered.

3.4 Conclusions

This work provides a first systematic approach to the research of RCC systems by combining first principle atomistic modeling and experimental electrochemical characterization in an RCE cell where transport is well-defined. This combination reveals that, during electrocatalytic reduction of bicarbonate and amine-based CO_2 capture solutions on a Ag electrode, decomposition of the CO_2-capture agent complex and electroreduction of unbound dissolved CO_2 is the primary mechanism for CO production.

Only at highly negative potential, in the case of amine-based capture, can a reaction channel consisting of direct reduction of the carbamate participate in the reaction kinetics, as suggested by a comparison of potential determining steps calculated from first principles and experiments, where the concentrations of the different carbon species are quantified and where their transport at the gas/liquid and liquid/solid interfaces can be modelled and experimentally controlled.

Future efforts in the RCC field must be geared towards the standardization of data acquisition and reporting that account for spatial and temporal changes in the thermodynamics and concentration of species through the detailed measurement of mass, heat, and charge transfer rates as well as the measurement of local reaction kinetics in the gas/liquid and liquid/solid interfaces. This is required to uncover efficient processes for the utilization of captured CO_2.

Chapter 4: Conclusions and prospects

The dissertation demonstrates the development of effective and selective electrochemical conversion strategies for utilizing greenhouse gases, which have the potential to tackle the challenges of global warming and supplement future energy demands.

Specifically, in Chapter 2, electrodeposition of a family of thin-film transition metal (oxy)hydroxides was demonstrated, which is a simple and clean strategy for the fabrication of electrodes for the partial oxidation of methane to methanol. This strategy excludes the possible existence of any carbon sources other than dissolved methane and paves the way for further systematic studies. CoO_x, NiO_x, MnO_x and CuO_x were active for the partial oxidation of methane to methanol while FeO_x oxidized methane entirely to CO_2 in the potentials tested. Taking CoO_x as a prototypical methane partial oxidation electrocatalyst, medium overpotential regime (0.86~1.06V vs SHE) was justified to be most selective for methane to methanol through both experiments in a gas-tight rotating cylinder electrode cell and theoretical DFT calculations. Medium temperature (room temperature at ca. 17^{o}C) that balancing the reaction rates of methane activation, methanol overoxidation, and OER as well as the solubility of CH_4 was found to be favored towards the production of methanol. In addition, catalyst loading (porosity) correlated with rotational speed (convection of electrolyte) implied the importance of mass transfer in partial oxidation of methane. Under well-defined conditions of mass, heat, and charge transport, all mass transfer coefficients and reaction rate constants can be collected. This information will enable the development of devices with advanced designs having precise control on hydrodynamics and reaction rates, which can be utilized for decentralized partial oxidation of methane at ambient temperatures.

In Chapter 3, the primary mechanism for CO production during electrocatalytic reduction of bicarbonate and amine-based CO_2 capture solutions on a silver electrode is shown to be the decomposition of the CO_2-capture agent complex and subsequent electroreduction of unbound

dissolved CO_2 by combining first principle modeling and experimental electrochemical characterization in an RCE cell with well-defined transport. Meanwhile, the direct reduction of carbamate can only participate in the reaction at highly negative potential in the case of amine-based capturing agent which is suggested by a comparison of potential determining steps theoretically and experimentally. Future discovery of electrocatalysts for RCC should also take corrosion, restructuring and irreversible absorption of molecules into account. Additionally, the well-defined characterization of spatial and temporal speciation; mass, heat, and charge transfer; and reaction kinetics for the gas/liquid and liquid/solid interfaces will facilitate the design of all the units including the pumps and heat exchangers during the scale-up.

In summary, deep understanding of reaction mechanisms and rigorous control of transport are the key parts in the development of electrocatalytic technologies for the capture and conversion of greenhouse gases. By employing these design principles, the performance of reactors can be significantly enhanced.

Although many attempts have been made to convert greenhouse gases into value-added products, we believe that there is still much to discover and understand in order to combat global warming and create a brighter future for humans.

References

(1) Masson-Delmotte, V.; Zhai, P.; Pirani, A.; Connors, S. L.; Péan, C.; Berger, S.; Caud, N.; Chen, Y.; Goldfarb, L.; Gomis, M. Climate change 2021: the physical science basis. *Contribution of working group I to the sixth assessment report of the intergovernmental panel on climate change* **2021**, *2*.

(2) Meinshausen, M.; Meinshausen, N.; Hare, W.; Raper, S. C.; Frieler, K.; Knutti, R.; Frame, D. J.; Allen, M. R. Greenhouse-gas emission targets for limiting global warming to 2°C. *Nature* **2009**, *458* (7242), 1158-1162.

(3) Gasser, T.; Guivarch, C.; Tachiiri, K.; Jones, C.; Ciais, P. Negative emissions physically needed to keep global warming below 2°C. *Nature communications* **2015**, *6* (1), 1-7.

(4) Crabtree, R. H. Aspects of methane chemistry. *Chemical Reviews* **1995**, *95* (4), 987-1007.

(5) Caballero, A.; Perez, P. J. Methane as raw material in synthetic chemistry: The final frontier. *Chemical Society Reviews* **2013**, *42* (23), 8809-8820.

(6) Sher Shah, M. S. A.; Oh, C.; Park, H.; Hwang, Y. J.; Ma, M.; Park, J. H. Catalytic oxidation of methane to oxygenated products: recent advancements and prospects for electrocatalytic and photocatalytic conversion at low temperatures. *Advanced Science* **2020**, *7* (23), 2001946.

(7) Hammer, G.; Lübcke, T.; Kettner, R.; Pillarella, M. R.; Recknagel, H.; Commichau, A.; Neumann, H. J.; Paczynska-Lahme, B. Natural gas. *Ullmann's Encyclopedia of Industrial Chemistry* **2000**.

(8) *Primary energy consumption by source*. U.S. Energy Information Administration, 2023. https://www.eia.gov/totalenergy/data/browser/index.php?tbl=T01.03#/?f=A&start=1949&end=2020&charted=1-2-3-5-12 (accessed 2023-02-14).

(9) Ming, T.; Davies, P.; Liu, W.; Caillol, S. Removal of non-CO_2 greenhouse gases by large-scale atmospheric solar photocatalysis. *Progress in Energy and Combustion Science* **2017**, *60*, 68-96.

(10) Karl, D. M.; Beversdorf, L.; Björkman, K. M.; Church, M. J.; Martinez, A.; Delong, E. F. Aerobic production of methane in the sea. *Nature Geoscience* **2008**, *1* (7), 473-478.

(11) Reay, D.; Smith, P. *Methane and climate change*; Routledge, 2010.

(12) Beck, C.; Rashidbeigi, S.; Roelofsen, O.; Speelman, E. The future is now: How oil and gas companies can decarbonize. *Oil and Gas Practice, McKinsey & Company* **2020**.

(13) Wang, S.; Zhang, Y.; Ju, W.; Chen, J. M.; Ciais, P.; Cescatti, A.; Sardans, J.; Janssens, I. A.; Wu, M.; Berry, J. A. Recent global decline of CO_2 fertilization effects on vegetation photosynthesis. *Science* **2020**, *370* (6522), 1295-1300.

(14) *Global Gas Flaring Reduction Partnership (GGFR)*. The World Bank, 2019. http://www.worldbank.org/en/programs/gasflaringreduction (accessed 2023-02-14).

(15) Meng, X.; Cui, X.; Rajan, N. P.; Yu, L.; Deng, D.; Bao, X. Direct methane conversion under mild condition by thermo-, electro-, or photocatalysis. *Chem* **2019**, *5* (9), 2296-2325.

(16) *Methanol Market - Global Industry Assessment & Forecast*. Vantage Market Research, 2023. https://www.vantagemarketresearch.com/industry-report/methanol-market-1842 (accessed 2023-02-14).

(17) Ravi, M.; Ranocchiari, M.; van Bokhoven, J. The direct catalytic oxidation of methane to methanol-A critical assessment. *Angewandte Chemie-International Edition* **2017**, *56* (52), 16464-16483.

(18) Sirajuddin, S.; Rosenzweig, A. Enzymatic oxidation of methane. *Biochemistry* **2015**, *54* (14), 2283-2294.

(19) Gunsalus, N.; Koppaka, A.; Park, S.; Bischof, S.; Hashiguchi, B.; Periana, R. Homogeneous functionalization of methane. *Chemical Reviews* **2017**, *117* (13), 8521-8573.

(20) Sushkevich, V.; Palagin, D.; Ranocchiari, M.; van Bokhoven, J. Selective anaerobic oxidation of methane enables direct synthesis of methanol. *Science* **2017**, *356* (6337), 523-527.

(21) Ikbal, S.; Colomban, C.; Zhang, D.; Delecluse, M.; Brotin, T.; Dufaud, V.; Dutasta, J.; Sorokin, A.; Martinez, A. Bioinspired oxidation of methane in the confined spaces of molecular cages. *Inorganic Chemistry* **2019**, *58* (11), 7220-7228.

(22) Dinh, K.; Sullivan, M.; Serna, P.; Meyer, R.; Dinca, M.; Roman-Leshkov, Y. Viewpoint on the partial oxidation of methane to methanol using Cu- and Fe-exchanged zeolites. *ACS Catalysis* **2018**, *8* (9), 8306-8313.

(23) Hammond, C.; Forde, M.; Ab Rahim, M.; Thetford, A.; He, Q.; Jenkins, R.; Dimitratos, N.; Lopez-Sanchez, J.; Dummer, N.; Murphy, D.; et al. Direct catalytic conversion of methane to methanol in an aqueous medium by using copper-promoted Fe-ZSM-5. *Angewandte Chemie-International Edition* **2012**, *51* (21), 5129-5133.

(24) Arnarson, L.; Schmidt, P.; Pandey, M.; Bagger, A.; Thygesen, K.; Stephens, I.; Rossmeisl, J. Fundamental limitation of electrocatalytic methane conversion to methanol. *Physical Chemistry Chemical Physics* **2018**, *20* (16), 11152-11159.

(25) Yaashikaa, P.; Kumar, P. S.; Varjani, S. J.; Saravanan, A. A review on photochemical, biochemical and electrochemical transformation of CO2 into value-added products. *Journal of CO_2 Utilization* **2019**, *33*, 131-147.

(26) Jayaweera, I.; Jayaweera, P.; Perea, E.; Springer, R. Engineering-scale Demonstration of the Mixed-salt Process (MSP) for CO2 Capture. *Available at SSRN 3829316* **2021**.

(27) Rau, G. H. Electrochemical splitting of calcium carbonate to increase solution alkalinity: Implications for mitigation of carbon dioxide and ocean acidity. *Environmental science & technology* **2008**, *42* (23), 8935-8940.

(28) Eisaman, M. D.; Alvarado, L.; Larner, D.; Wang, P.; Garg, B.; Littau, K. A. CO_2 separation using bipolar membrane electrodialysis. *Energy & Environmental Science* **2011**, *4* (4), 1319-1328.

(29) Datta, S.; Henry, M. P.; Lin, Y. J.; Fracaro, A. T.; Millard, C. S.; Snyder, S. W.; Stiles, R. L.; Shah, J.; Yuan, J.; Wesoloski, L. Electrochemical CO_2 capture using resin-wafer electrodeionization. *Industrial & Engineering Chemistry Research* **2013**, *52* (43), 15177-15186.

(30) Jin, S.; Wu, M.; Gordon, R. G.; Aziz, M. J.; Kwabi, D. G. pH swing cycle for CO_2 capture electrochemically driven through proton-coupled electron transfer. *Energy & Environmental Science* **2020**, *13* (10), 3706-3722.

(31) Appel, A. M.; Newell, R.; DuBois, D. L.; Rakowski DuBois, M. Concentration of carbon dioxide by electrochemically modulated complexation with a binuclear copper complex. *Inorganic chemistry* **2005**, *44* (9), 3046-3056.

(32) Stern, M. C.; Simeon, F.; Herzog, H.; Hatton, T. A. Post-combustion carbon dioxide capture using electrochemically mediated amine regeneration. *Energy & Environmental Science* **2013**, *6* (8), 2505-2517.

(33) Rahimi, M.; Diederichsen, K. M.; Ozbek, N.; Wang, M.; Choi, W.; Hatton, T. A. An electrochemically mediated amine regeneration process with a mixed absorbent for postcombustion CO_2 capture. *Environmental Science & Technology* **2020**, *54* (14), 8999-9007.

(34) Apaydin, D. H.; Głowacki, E. D.; Portenkirchner, E.; Sariciftci, N. S. Direct electrochemical capture and release of carbon dioxide using an industrial organic pigment: quinacridone. *Angewandte Chemie International Edition* **2014**, *53* (26), 6819-6822.

(35) Voskian, S.; Hatton, T. A. Faradaic electro-swing reactive adsorption for CO_2 capture. *Energy & Environmental Science* **2019**, *12* (12), 3530-3547.

(36) Liu, Y.; Ye, H.-Z.; Diederichsen, K. M.; Van Voorhis, T.; Hatton, T. A. Electrochemically mediated carbon dioxide separation with quinone chemistry in salt-concentrated aqueous media. *Nature communications* **2020**, *11* (1), 1-11.

(37) Scovazzo, P.; Poshusta, J.; DuBois, D.; Koval, C.; Noble, R. Electrochemical separation and concentration of< 1% carbon dioxide from nitrogen. *Journal of The Electrochemical Society* **2003**, *150* (5), D91.

(38) Gurkan, B.; Simeon, F.; Hatton, T. A. Quinone reduction in ionic liquids for electrochemical CO_2 separation. *ACS Sustainable Chemistry & Engineering* **2015**, *3* (7), 1394-1405.

(39) Watkins, J. D.; Siefert, N. S.; Zhou, X.; Myers, C. R.; Kitchin, J. R.; Hopkinson, D. P.; Nulwala, H. B. Redox-mediated separation of carbon dioxide from flue gas. *Energy & Fuels* **2015**, *29* (11), 7508-7515.

(40) Ranjan, R.; Olson, J.; Singh, P.; Lorance, E. D.; Buttry, D. A.; Gould, I. R. Reversible electrochemical trapping of carbon dioxide using 4, 4′-bipyridine that does not require thermal activation. *The Journal of Physical Chemistry Letters* **2015**, *6* (24), 4943-4946.

(41) Singh, P.; Rheinhardt, J. H.; Olson, J. Z.; Tarakeshwar, P.; Mujica, V.; Buttry, D. A. Electrochemical capture and release of carbon dioxide using a disulfide–thiocarbonate redox cycle. *Journal of the American Chemical Society* **2017**, *139* (3), 1033-1036.

(42) Goeppert, A.; Zhang, H.; Czaun, M.; May, R. B.; Prakash, G. S.; Olah, G. A.; Narayanan, S. Easily regenerable solid adsorbents based on polyamines for carbon dioxide capture from the air. *ChemSusChem* **2014**, *7* (5), 1386-1397.

(43) Li, D.; Furukawa, H.; Deng, H.; Liu, C.; Yaghi, O. M.; Eisenberg, D. S. Designed amyloid fibers as materials for selective carbon dioxide capture. *Proceedings of the National Academy of Sciences* **2014**, *111* (1), 191-196.

(44) Seo, H.; Rahimi, M.; Hatton, T. A. Electrochemical Carbon Dioxide Capture and Release with a Redox-Active Amine. *Journal of the American Chemical Society* **2022**, *144* (5), 2164-2170.

(45) Heldebrant, D. J.; Kothandaraman, J.; Mac Dowell, N.; Brickett, L. Next steps for solvent-based CO_2 capture; integration of capture, conversion, and mineralisation. *Chemical Science* **2022**, *13* (22), 6445-6456.

(46) Kothandaraman, J.; Saavedra Lopez, J.; Jiang, Y.; Walter, E. D.; Burton, S. D.; Dagle, R. A.; Heldebrant, D. J. Integrated Capture and Conversion of CO_2 to Methane Using a Water-lean, Post-Combustion CO_2 Capture Solvent. *ChemSusChem* **2021**, *14* (21), 4812-4819.

(47) Liu, Q.; Yang, X.; Li, L.; Miao, S.; Li, Y.; Li, Y.; Wang, X.; Huang, Y.; Zhang, T. Direct catalytic hydrogenation of CO_2 to formate over a Schiff-base-mediated gold nanocatalyst. *Nature communications* **2017**, *8* (1), 1407.

(48) Wang, B.; Albarracín-Suazo, S.; Pagán-Torres, Y.; Nikolla, E. Advances in methane conversion processes. *Catalysis Today* **2017**, *285*, 147-158.

(49) Aresta, M.; Dibenedetto, A.; Quaranta, E. State of the art and perspectives in catalytic processes for CO2 conversion into chemicals and fuels: The distinctive contribution of chemical catalysis and biotechnology. *Journal of Catalysis* **2016**, *343*, 2-45.

(50) Jang, J.; Shen, K.; Morales-Guio, C. G. Electrochemical direct partial oxidation of methane to methanol. *Joule* **2019**, *3* (11), 2589-2593.

(51) *Global Gas Flaring Reduction Partnership (GGFR)*. The World Bank, 2019. http://www.worldbank.org/en/programs/gasflaringreduction (accessed 2023-02-14).

(52) *Tracking Industry 2020*; IEA, 2020. https://www.iea.org/reports/tracking-industry-2020 (accessed 2023-02-14).

(53) *Mission Possible: Reaching net-zero carbon emissions from harder-to-abate sectors by mid-century*; Energy Transitions Commission, 2018. http://www.energy-transitions.org/mission-possible (accessed 2023-02-14).

(54) Institute, I. a. M. *Innovation Outlook: Renewable Methanol*; 2021. https://www.irena.org/publications/2021/Jan/Innovation-Outlook-Renewable-Methanol (accessed 2023-02-14).

(55) Soucie, H.; Elam, M.; Mustain, W. E. Practical Assessment for At-Scale Electrochemical Conversion of Methane to Methanol. *ACS Energy Lett.* **2023**, *8* (2), 1218-1229.

(56) Yuan, S.; Li, Y. D.; Peng, J. Y.; Questell-Santiago, Y. M.; Akkiraju, K.; Giordano, L.; Zheng, D. J.; Bagi, S.; Roman-Leshkov, Y.; Shao-Horn, Y. Conversion of Methane into Liquid Fuels-Bridging Thermal Catalysis with Electrocatalysis. *Adv Energy Mater* **2020**, *10* (40), 2002154.

(57) Mostaghimi, A.; Al-Attas, T.; Kibria, M.; Siahrostami, S. A review on electrocatalytic oxidation of methane to oxygenates. *Journal of Materials Chemistry A* **2020**, *8* (31), 15575-15590.

(58) Shah, M.; Oh, C.; Park, H.; Hwang, Y.; Ma, M.; Park, J. Catalytic Oxidation of Methane to Oxygenated Products: Recent Advancements and Prospects for Electrocatalytic and Photocatalytic Conversion at Low Temperatures. *Adv. Sci.* **2020**, *7* (23), 2001946.

(59) Deng, J.; Lin, S.; Fuller, J.; Iniguez, J.; Xiang, D.; Yang, D.; Chan, G.; Chen, H.; Alexandrova, A.; Liu, C. Ambient methane functionalization initiated by electrochemical oxidation of a vanadium (V)-oxo dimer. *Nature Communications* **2020**, *11* (1), 3686.

(60) Kim, R. S.; Surendranath, Y. Electrochemical reoxidation enables continuous methane-to-methanol catalysis with aqueous Pt salts. *ACS Central Science* **2019**, *5* (7), 1179-1186.

(61) Foster, N. Direct catalytic oxidation of methane to methanol - a review. *Applied Catalysis* **1985**, *19* (1), 1-11.

(62) Sushkevich, V. L.; Palagin, D.; Ranocchiari, M.; van Bokhoven, J. A. Selective anaerobic oxidation of methane enables direct synthesis of methanol. *Science* **2017**, *356* (6337), 523-527.

(63) Gunsalus, N. J.; Koppaka, A.; Park, S. H.; Bischof, S. M.; Hashiguchi, B. G.; Periana, R. A. Homogeneous functionalization of methane. *Chemical Reviews* **2017**, *117* (13), 8521-8573.

(64) Ravi, M.; Ranocchiari, M.; van Bokhoven, J. A. The direct catalytic oxidation of methane to methanol-A critical assessment. *Angewandte Chemie-International Edition* **2017**, *56* (52), 16464-16483.

(65) Mahyuddin, M.; Shiota, Y.; Yoshizawa, K. Methane selective oxidation to methanol by metal-exchanged zeolites: a review of active sites and their reactivity. *Catalysis Science & Technology* **2019**, *9* (8), 1744-1768.

(66) Andrikopoulos, P.; Michel, C.; Chouzier, S.; Sautet, P. In silico screening of iron-oxo catalysts for CH bond cleavage. *ACS Catalysis* **2015**, *5* (4), 2490-2499.

(67) Ensing, B.; Buda, F.; Gribnau, M.; Baerends, E. Methane-to-methanol oxidation by the hydrated iron(IV) oxo species in aqueous solution: A combined DFT and car-parrinello molecular dynamics study. *Journal of the American Chemical Society* **2004**, *126* (13), 4355-4365.

(68) Szecsenyi, A.; Li, G.; Gascon, J.; Pidko, E. Mechanistic complexity of methane oxidation with H_2O_2 by single-site Fe/ZSM-5 catalyst. *ACS Catalysis* **2018**, *8* (9), 7961-7972.

(69) Sirajuddin, S.; Rosenzweig, A. C. Enzymatic oxidation of methane. *Biochemistry* **2015**, *54* (14), 2283-2294.

(70) Lee, S.; McCormick, M.; Lippard, S.; Cho, U. Control of substrate access to the active site in methane monooxygenase. *Nature* **2013**, *494* (7437), 380-384.

(71) Omasta, T. J.; Rigdon, W. A.; Lewis, C. A.; Stanis, R. J.; Liu, R.; Fan, C. Q.; Mustain, W. E. Two pathways for near room temperature electrochemical conversion of methane to methanol. *ECS Transactions* **2015**, *66* (8), 129-136.

(72) Spinner, N.; Mustain, W. Electrochemical methane activation and conversion to oxygenates at room temperature. *Journal of the Electrochemical Society* **2013**, *160* (11), F1275-F1281.

(73) Spinner, N.; Mustain, W. Influence of non-conducting zirconia on the electrochemical performance of nickel oxide in alkaline media at room temperature. *Journal of the Electrochemical Society* **2012**, *159* (12), E187-E192.

(74) Ma, M.; Jin, B. J.; Li, P.; Jung, M. S.; Kim, J. I.; Cho, Y.; Kim, S.; Moon, J. H.; Park, J. H. Ultrahigh electrocatalytic conversion of methane at room temperature. *Advanced Science* **2017**, *4* (12), 1700379.

(75) Oh, C.; Kim, J.; Hwang, Y. J.; Ma, M.; Park, J. H. Electrocatalytic methane oxidation on Co3O4-incorporated ZrO_2 nanotube powder. *Appl Catal B-Environ* **2021**, *283*, 119653.

(76) Jang, J.; Rüscher, M.; Winzely, M.; Morales-Guio, C. G. Gastight rotating cylinder electrode: Toward decoupling mass transport and intrinsic kinetics in electrocatalysis. *AIChE Journal* **2022**, *68* (5), e17605.

(77) Song, Y. F.; Zhao, Y. H.; Nan, G. Z.; Chen, W.; Guo, Z. K.; Li, S. G.; Tang, Z. Y.; Wei, W.; Sun, Y. H. Electrocatalytic oxidation of methane to ethanol via NiO/Ni interface. *Appl Catal B-Environ* **2020**, *270*, 118888.

(78) Guo, Z.; Chen, W.; Song, Y.; Dong, X.; Li, G.; Wei, W.; Sun, Y. Efficient methane electrocatalytic conversion over a Ni-based hollow fiber electrode. *Chinese Journal of Catalysis* **2020**, *41* (7), 1067-1072.

(79) Li, J. L.; Yao, L. B.; Wu, D. Z.; King, J.; Chuang, S. S. C.; Liu, B.; Peng, Z. M. Electrocatalytic methane oxidation to ethanol on iron-nickel hydroxide nanosheets. *Appl Catal B-Environ* **2022**, *316*, 121657.

(80) Prajapati, A.; Collins, B. A.; Goodpaster, J. D.; Singh, M. R. Fundamental insight into electrochemical oxidation of methane towards methanol on transition metal oxides. *Proceedings of the National Academy of Sciences* **2021**, *118* (8), e2023233118.

(81) Prajapati, A.; Sartape, R.; Kani, N.; Gauthier, J.; Singh, M. Chloride-Promoted High-Rate Ambient Electrooxidation of Methane to Methanol on Patterned Cu-Ti Bimetallic Oxides. *ACS Catalysis* **2022**, *12* (22), 14321-14329.

(82) Boyd, M.; Latimer, A.; Dickens, C.; Nielander, A.; Hahn, C.; Norskov, J.; Higgins, D.; Jaramillo, T. Electro-oxidation of methane on platinum under ambient conditions. *ACS Catalysis* **2019**, *9* (8), 7578-7587.

(83) Morales-Guio, C.; Liardet, L.; Hu, X. Oxidatively electrodeposited thin-film transition metal (oxy)hydroxides as oxygen evolution catalysts. *Journal of the American Chemical Society* **2016**, *138* (28), 8946-8957.

(84) Richard, D.; Tom, M.; Jang, J.; Yun, S. G.; Christofides, P. D.; Morales-Guio, C. G. Quantifying transport and electrocatalytic reaction processes in a gastight rotating cylinder electrode reactor via integration of Computational Fluid Dynamics modeling and experiments. *Electrochimica Acta* **2023**, *440*, 141698.

(85) Kresse, G.; Hafner, J. Ab initio molecular-dynamics simulation of the liquid-metal-amorphous-semiconductor transition in germanium. *Physical Review B* **1994**, *49* (20), 14251-14269.

(86) Kresse, G.; Joubert, D. From ultrasoft pseudopotentials to the projector augmented-wave method. *Physical Review B* **1999**, *59* (3), 1758-1775.

(87) Kresse, G.; Furthmuller, J. Efficiency of ab-initio total energy calculations for metals and semiconductors using a plane-wave basis set. *Computational Materials Science* **1996**, *6* (1), 15-50.

(88) Kresse, G.; Furthmuller, J. Efficient iterative schemes for ab initio total-energy calculations using a plane-wave basis set. *Physical Review B* **1996**, *54* (16), 11169-11186.

(89) Perdew, J.; Burke, K.; Ernzerhof, M. Generalized gradient approximation made simple. *Physical Review Letters* **1996**, *77* (18), 3865-3868.

(90) Garcia-Mota, M.; Bajdich, M.; Viswanathan, V.; Vojvodic, A.; Bell, A.; Norskov, J. Importance of Correlation in Determining Electrocatalytic Oxygen Evolution Activity on Cobalt Oxides. *Journal of Physical Chemistry C* **2012**, *116* (39), 21077-21082.

(91) Bajdich, M.; Garcia-Mota, M.; Vojvodic, A.; Norskov, J.; Bell, A. Theoretical Investigation of the Activity of Cobalt Oxides for the Electrochemical Oxidation of Water. *Journal of the American Chemical Society* **2013**, *135* (36), 13521-13530.

(92) Nurlaela, E.; Wang, H.; Shinagawa, T.; Flanagan, S.; Ould-Chikh, S.; Qureshi, M.; Mics, Z.; Sautet, P.; Le Bahers, T.; Canovas, E.; et al. Enhanced Kinetics of Hole Transfer and Electrocatalysis during Photocatalytic Oxygen Evolution by Cocatalyst Tuning. *Acs Catalysis* **2016**, *6* (7), 4117-4126.

(93) Chivot, J.; Mendoza, L.; Mansour, C.; Pauporte, T.; Cassir, M. New insight in the behaviour of Co-H_2O system at 25-150^{o}C, based on revised Pourbaix diagrams. *Corrosion Science* **2008**, *50* (1), 62-69.

(94) Curutchet, A.; Colinet, P.; Michel, C.; Steinmann, S.; Le Bahers, T. Two-sites are better than one: revisiting the OER mechanism on CoOOH by DFT with electrode polarization. *Physical Chemistry Chemical Physics* **2020**, *22* (13), 7031-7038.

(95) Kumari, S.; Sautet, P. Highly dispersed Pt atoms and clusters on hydroxylated indium tin oxide: a view from first-principles calculations. *Journal of Materials Chemistry A* **2021**, *9* (28), 15724-15733.

(96) Kumari, S.; Masubuchi, T.; White, H. S.; Alexandrova, A.; Anderson, S. L.; Sautet, P. Electrocatalytic hydrogen evolution at full atomic utilization over ITO-supported sub-nano Pt_n clusters: High, size-dependent activity controlled by fluxional Pt hydride species. *Journal of the American Chemical Society* **2023**, *145* (10), 5834-5845.

(97) Dudarev, S.; Botton, G.; Savrasov, S.; Humphreys, C.; Sutton, A. Electron-energy-loss spectra and the structural stability of nickel oxide: An LSDA+U study. *Physical Review B* **1998**, *57* (3), 1505-1509.

(98) Mathew, K.; Sundararaman, R.; Letchworth-Weaver, K.; Arias, T. A.; Hennig, R. G. Implicit solvation model for density-functional study of nanocrystal surfaces and reaction pathways. *J Chem Phys* **2014**, *140* (8), 084106.

(99) Mathew, K.; Kolluru, V. S. C.; Mula, S.; Steinmann, S. N.; Hennig, R. G. Implicit self-consistent electrolyte model in plane-wave density-functional theory. *J Chem Phys* **2019**, *151* (23), 234101.

(100) Mathew, K.; Kolluru, V. S. C.; Hennig, R. G. *VASPsol: Implicit solvation and electrolyte model for density-functional theory*. 2018.

(101) Taylor, C.; Wasileski, S.; Filhol, J.; Neurock, M. First principles reaction modeling of the electrochemical interface: Consideration and calculation of a tunable surface potential from atomic and electronic structure. *Physical Review B* **2006**, *73* (16), 165402.

(102) Hajar, Y.; Treps, L.; Michel, C.; Baranova, E.; Steinmann, S. Theoretical insight into the origin of the electrochemical promotion of ethylene oxidation on ruthenium oxide. *Catalysis Science & Technology* **2019**, *9* (21), 5915-5926.

(103) Kanan, M.; Surendranath, Y.; Nocera, D. Cobalt-phosphate oxygen-evolving compound. *Chemical Society Reviews* **2009**, *38* (1), 109-114.

(104) Burke, M. S.; Enman, L. J.; Batchellor, A. S.; Zou, S.; Boettcher, S. W. Oxygen Evolution Reaction Electrocatalysis on Transition Metal Oxides and (Oxy)hydroxides: Activity Trends and Design Principles. *Chemistry of Materials* **2015**, *27* (22), 7549-7558.

(105) Lee, B.; Sakamoto, Y.; Hirabayashi, D.; Suzuki, K.; Hibino, T. Direct oxidation of methane to methanol over proton conductor/metal mixed catalysts. *J. Catal.* **2010**, *271* (2), 195-200.

(106) Risch, M.; Ringleb, F.; Kohlhoff, M.; Bogdanoff, P.; Chernev, P.; Zaharieva, I.; Dau, H. Water oxidation by amorphous cobalt-based oxides: in situ tracking of redox transitions and mode of catalysis. *Energy & Environmental Science* **2015**, *8* (2), 661-674.

(107) Klingan, K.; Ringleb, F.; Zaharieva, I.; Heidkamp, J.; Chernev, P.; Gonzalez-Flores, D.; Risch, M.; Fischer, A.; Dau, H. Water Oxidation by Amorphous Cobalt-Based Oxides: Volume Activity and Proton Transfer to Electrolyte Bases. *Chemsuschem* **2014**, *7* (5), 1301-1310.

(108) Richard, D.; Tom, M.; Jang, J.; Yun, S.; Christofides, P. D.; Morales-Guio, C. G. Quantifying transport and electrocatalytic reaction processes in a gastight rotating cylinder electrode reactor via integration of Computational Fluid Dynamics modeling and experiments. *Electrochimica Acta* **2022**, 141698.

(109) Fornaciari, J. C.; Primc, D.; Kawashima, K.; Wygant, B. R.; Verma, S.; Spanu, L.; Mullins, C. B.; Bell, A. T.; Weber, A. Z. A Perspective on the Electrochemical Oxidation of Methane to Methanol in Membrane Electrode Assemblies. *ACS Energy Letters* **2020**, *5* (9), 2954-2963.

(110) Stevens, M.; Enman, L.; Korkus, E.; Zaffran, J.; Trang, C.; Asbury, J.; Kast, M.; Toroker, M.; Boettcher, S. Ternary Ni-Co-Fe oxyhydroxide oxygen evolution catalysts: Intrinsic activity trends, electrical conductivity, and electronic band structure. *Nano Research* **2019**, *12* (9), 2288-2295.

(111) Morales-Guio, C.; Mayer, M.; Yella, A.; Tilley, S.; Gratzel, M.; Hu, X. An optically transparent iron nickel oxide catalyst for solar water splitting. *Journal of the American Chemical Society* **2015**, *137* (31), 9927-9936.

(112) Gerken, J.; McAlpin, J.; Chen, J.; Rigsby, M.; Casey, W.; Britt, R.; Stahl, S. Electrochemical Water Oxidation with Cobalt-Based Electrocatalysts from pH 0-14: The Thermodynamic Basis for Catalyst Structure, Stability, and Activity. *Journal of the American Chemical Society* **2011**, *133* (36), 14431-14442.

(113) Gannouni, A.; Delbecq, F.; Zina, M.; Sautet, P. Oxidation of methane to methanol over single site palladium oxide species on silica: A mechanistic view from DFT. *Journal of Physical Chemistry a* **2017**, *121* (29), 5500-5508.

(114) Goltl, F.; Michel, C.; Andrikopoulos, P.; Love, A.; Hafner, J.; Hermans, I.; Sautet, P. Computationally exploring confinement effects in the methane-to-methanol conversion over iron-oxo centers in zeolites. *ACS Catalysis* **2016**, *6* (12), 8404-8409.

(115) Lee, B.; Hibino, T. Efficient and selective formation of methanol from methane in a fuel cell-type reactor. *J. Catal.* **2011**, *279* (2), 233-240.

(116) Tomita, A.; Nakajima, J.; Hibino, T. Direct oxidation of methane to methanol at low temperature and pressure in an electrochemical fuel cell. *Angew. Chem. Int. Ed.* **2008**, *47* (8), 1462-1464.

(117) Hibino, T.; Kobayashi, K.; Nagao, M.; Dongwen, Z.; Siyuan, C. Two-stage electrolysis of H_2O and CO_2 to methanol: CO_2-to-methane reduction at the cathode and subsequent methane-to-methanol oxidation at the anode. *Journal of Materials Chemistry a* **2022**, *10* (42), 22718-22729.

(118) Jerng, S. E.; Gallant, B. M. Electrochemical reduction of CO_2 in the captured state using aqueous or nonaqueous amines. *iScience* **2022**, *25* (7), 104558.

(119) Li, M.; Yang, K.; Abdinejad, M.; Zhao, C.; Burdyny, T. Advancing integrated CO_2 electrochemical conversion with amine-based CO_2 capture: a review. *Nanoscale* **2022**, *14* (33), 11892-11908.

(120) Siegel, R. E.; Pattanayak, S.; Berben, L. A. Reactive Capture of CO_2: Opportunities and Challenges. *ACS Catal.* **2023**, *13* (1), 766-784.

(121) Sullivan, I.; Goryachev, A.; Digdaya, I.; Li, X.; Atwater, H.; Vermaas, D.; Xiang, C. Coupling electrochemical CO_2 conversion with CO_2 capture. *Nature Catalysis* **2021**, *4* (11), 952-958.

(122) Perez-Gallent, E.; Vankani, C.; Sanchez-Martinez, C.; Anastasopol, A.; Goetheer, E. Integrating CO_2 Capture with Electrochemical Conversion Using Amine-Based Capture Solvents as Electrolytes. *Industrial & Engineering Chemistry Research* **2021**, *60* (11), 4269-4278.

(123) Wong, M. K.; Shariff, A. M.; Bustam, M. A. Raman spectroscopic study on the equilibrium of carbon dioxide in aqueous monoethanolamine. *RSC Advances* **2016**, *6* (13), 10816-10823.

(124) Lee, J. I.; Otto, F. D.; Mather, A. E. Equilibrium between carbon dioxide and aqueous monoethanolamine solutions. *Journal of Applied Chemistry and Biotechnology* **1976**, *26* (1), 541-549.

(125) Zhu, K.; Yue, C. H.; Wei, Z. H.; Huang, J. J.; Hu, M.; Ji, Y. F.; Liu, H. F.; Zhu, H.; Guo, W. X.; Zhou, F.; et al. Experimental and Thermodynamic Investigation on CO_2 Absorption in Aqueous MEA Solutions. *Advances in Materials Science and Engineering* **2022**, *2022*, 6278342.

(126) Böttinger, W.; Maiwald, M.; Hasse, H. Online NMR spectroscopic study of species distribution in MEA–H_2O–CO_2 and DEA–H_2O–CO_2. *Fluid Phase Equilibria* **2008**, *263* (2), 131-143.

(127) Simoes, M. C.; Hughes, K. J.; Ingham, D. B.; Ma, L.; Pourkashanian, M. Predicting Speciation of Ammonia, Monoethanolamine, and Diethanolamine Using Only Ionic Radius and Ionic Charge. *Industrial & Engineering Chemistry Research* **2018**, *57* (6), 2346-2352.

(128) Jakobsen, J. P.; Krane, J.; Svendsen, H. F. Liquid-Phase Composition Determination in CO_2−H_2O−Alkanolamine Systems: An NMR Study. *Industrial & Engineering Chemistry Research* **2005**, *44* (26), 9894-9903.

(129) Lees, E.; Goldman, M.; Fink, A.; Dvorak, D.; Salvatore, D.; Zhang, Z.; Loo, N.; Berlinguette, C. Electrodes Designed for Converting Bicarbonate into CO. *ACS Energy Lett.* **2020**, *5* (7), 2165-2173.

(130) Li, T.; Lees, E.; Zhang, Z.; Berlinguette, C. Conversion of Bicarbonate to Formate in an Electrochemical Flow Reactor. *ACS Energy Lett.* **2020**, *5* (8), 2624-2630.

(131) Li, T.; Lees, E.; Goldman, M.; Salvatore, D.; Weekes, D.; Berlinguette, C. Electrolytic Conversion of Bicarbonate into CO in a Flow Cell. *Joule* **2019**, *3* (6), 1487-1497.

(132) Lee, G.; Li, Y.; Kim, J.; Peng, T.; Nam, D.; Rasouli, A.; Li, F.; Luo, M.; Ip, A.; Joo, Y.; et al. Electrochemical upgrade of CO_2 from amine capture solution. *Nature Energy* **2021**, *6* (1), 46-53.

(133) Rochelle, G. T. Amine scrubbing for CO_2 capture. *Science* **2009**, *325* (5948), 1652-1654.

(134) Edali, M.; Aboudheir, A.; Idem, R. Kinetics of carbon dioxide absorption into mixed aqueous solutions of MDEA and MEA using a laminar jet apparatus and a numerically solved 2D absorption rate/kinetics model. *International Journal of Greenhouse Gas Control* **2009**, *3* (5), 550-560.

(135) Grimme, S.; Antony, J.; Ehrlich, S.; Krieg, H. A consistent and accurate ab initio parametrization of density functional dispersion correction (DFT-D) for the 94 elements H-Pu. *J Chem Phys* **2010**, *132* (15), 154104.

(136) Steinmann, S.; Michel, C.; Schwiedernoch, R.; Sautet, P. Impacts of electrode potentials and solvents on the electroreduction of CO_2: a comparison of theoretical approaches. *Phys. Chem. Chem. Phys.* **2015**, *17* (21), 13949-13963.

(137) Jayaweera, I.; Jayaweera, P.; Yamasaki, Y.; Elmore, R. Mixed salt solutions for CO_2 capture. In *Absorption-Based Post-Combustion Capture of Carbon Dioxide*, Elsevier, 2016; pp 167-200.

(138) Steinmann, S. N.; Michel, C.; Schwiedernoch, R.; Sautet, P. Impacts of electrode potentials and solvents on the electroreduction of CO_2: a comparison of theoretical approaches. *Phys Chem Chem Phys* **2015**, *17* (21), 13949-13963.

(139) Steinmann, S. N.; Sautet, P. Assessing a First-Principles Model of an Electrochemical Interface by Comparison with Experiment. *The Journal of Physical Chemistry C* **2016**, *120* (10), 5619-5623.

(140) Steinmann, S. N.; Sautet, P.; Michel, C. Solvation free energies for periodic surfaces: comparison of implicit and explicit solvation models. *Phys Chem Chem Phys* **2016**, *18* (46), 31850-31861.

(141) Wei, Z.; Goltl, F.; Steinmann, S. N.; Sautet, P. Modeling Electrochemical Processes with Grand Canonical Treatment of Many-Body Perturbation Theory. *J Phys Chem Lett* **2022**, *13* (26), 6079-6084.

(142) Zarkadas, G.; Stergiou, A.; Papanastasiou, G. Influence of citric acid on the silver electrodeposition from aqueous $AgNO_3$ solutions. *Electrochimica acta* **2005**, *50* (25-26), 5022-5031.

(143) Vijay, S.; Ju, W.; Brückner, S.; Tsang, S. C.; Strasser, P.; Chan, K. R. Unified mechanistic understanding of CO_2 reduction to CO on transition metal and single atom catalysts. *Nature Catalysis* **2021**, *4* (12), 1024-1031.

(144) Clark, E. L.; Ringe, S.; Tang, M.; Walton, A.; Hahn, C.; Jaramillo, T. F.; Chan, K.; Bell, A. T. Influence of Atomic Surface Structure on the Activity of Ag for the Electrochemical Reduction of CO_2 to CO. *ACS catalysis* **2019**, *9* (5), 4006-4014.

(145) Huang, J. E.; Li, F.; Ozden, A.; Sedighian Rasouli, A.; Garcia de Arquer, F. P.; Liu, S.; Zhang, S.; Luo, M.; Wang, X.; Lum, Y.; et al. CO_2 electrolysis to multicarbon products in strong acid. *Science* **2021**, *372* (6546), 1074-1078.

(146) Monteiro, M.; Mirabal, A.; Jacobse, L.; Doblhoff-Dier, K.; Barton, S.; Koper, M. Time-Resolved Local pH Measurements during CO_2 Reduction Using Scanning Electrochemical Microscopy: Buffering and Tip Effects. *Jacs Au* **2021**, *1* (11), 1915-1924.

(147) Gutierrez-Sanchez, O.; Bohlen, B.; Daems, N.; Bulut, M.; Pant, D.; Breugelmans, T. A State-of-the-Art Update on Integrated CO_2 Capture and Electrochemical Conversion Systems. *Chemelectrochem* **2022**, *9* (5), e20210154.

(148) Hori, Y.; Vayenas, C.; White, R.; GamboaAldeco, M. Electrochemical CO_2 reduction on metal electrodes. *Modern Aspects of Electrochemistry* **2008**, (42), 89-189.

(149) Chen, L.; Li, F.; Zhang, Y.; Bentley, C.; Horne, M.; Bond, A.; Zhang, J. Electrochemical Reduction of Carbon Dioxide in a Monoethanolamine Capture Medium. *Chemsuschem* **2017**, *10* (20), 4109-4118.

(150) Parrish, W.; Newman, J. Current distribution on a plane electrode below the limiting current. *Journal of the Electrochemical Society* **1969**, *116* (2), 169.

(151) Parrish, W. R.; Newman, J. Current distributions on plane, parallel electrodes in channel flow. *Journal of the Electrochemical Society* **1970**, *117* (1), 43.

(152) Singh, M. R.; Kwon, Y.; Lum, Y.; Ager III, J. W.; Bell, A. T. Hydrolysis of electrolyte cations enhances the electrochemical reduction of CO_2 over Ag and Cu. *Journal of the American chemical society* **2016**, *138* (39), 13006-13012.

(153) Kash, B. C.; Gomes, R. J.; Amanchukwu, C. V. Mitigating Electrode Inactivation during CO_2 Electrocatalysis in Aprotic Solvents with Alkali Cations. *The Journal of Physical Chemistry Letters* **2023**, *14* (4), 920-926.